DISSERTATION

NON-EQUILIBRIUM STATES OF DISORDERED SYSTEMS: FROM LOW-FREQUENCY PROPERTIES OF GLASSES TO DISTRIBUTION FUNCTION OF ACTIVE ORNSTEIN-UHLENBECK PARTICLES

Submitted by

Alireza Shakerpoor

Department of Chemistry

In partial fulfillment of the requirements

For the Degree of Doctor of Philosophy

Colorado State University

Fort Collins, Colorado

Spring 2022

Doctoral Committee:

Advisor: Grzegorz Szamel

Alan Van Orden
Seonah Kim
Martin Gelfand

ABSTRACT

NON-EQUILIBRIUM STATES OF DISORDERED SYSTEMS: FROM LOW-FREQUENCY PROPERTIES OF GLASSES TO DISTRIBUTION FUNCTION OF ACTIVE ORNSTEIN-UHLENBECK PARTICLES

This dissertation focuses on stationary and dynamical properties of non-equilibrium systems of disordered matter. In particular, we discuss the correlation between the stability of ultra-stable to moderately stable amorphous solids and the structural fluctuations of the elastic field at low frequencies. We report a strong correlation between the stability and the structural homogeneity which we demonstrate numerically through the calculation of local elastic moduli of the solid. Notably, we do not identify any significant length scale associated with elastic correlations which bears specific implications for the wave attenuation in amorphous solids. In the second part of the dissertation, we shift our focus to the disordered systems of active matter. We derive a formal expression for the stationary probability density function of a tagged active particle in an interacting system of active Ornstein-Uhlenbeck particles. We further identify an effective temperature in the probability density function which allows for the subsequent numerical validation of our theoretical results beyond the linear response regime. We show that the effective temperature defined through the violation of the Einstein relation (or equivalently the fluctuation-dissipation theorem), can predict the tagged active particle's density distribution. Lastly, we derive theoretical expressions for the stationary probability density distribution and the current of a non-interacting active Ornstein-Uhlenbeck particle in a tilted periodic potential. We demonstrate the quantitative agreement of these expressions with our numerical results for small to moderate correlation times of the colored-noise. We further explore the dependence of the diffusive motion on the strength of tilting force. We observe a giant enhancement in the diffusion of the particle which becomes more pronounced with increasing the persistence time.

ACKNOWLEDGEMENTS

I would like to take this opportunity to thank all the people who made this journey possible for me. I would like to express my gratitude to Professor Grzegorz Szamel for his academic guidance and mentorship during the course of my PhD. Over the past few years I have learned many from Professor Szamel. I would like to thank him for all that as well as the stimulating conversations to make me a better researcher I am today.

I would like to extend my gratitude to Dr. Elijah Flenner for assisting me with developing codes in C and for his collaboration on projects presented in Chapters 2 and 3 of this thesis. I would also like to thank the National Science Foundation and the Principal Investigator, Professor Grzegorz Szamel, for partial financial support of my research.

Many thanks to my Graduate Committee members, Professor Alan Van Orden, Professor Seonah Kim, and Professor Martin Gelfand, for their time, consideration, and insightful feedback on my research. In particular, I am thankful to Professor Van Orden for his continued support throughout my PhD.

Special thanks to my dear friends inside and outside the United States for their companionship and our timeless moments together.

Lastly, my heartfelt appreciation goes out to my family who made this journey possible for me. I am thankful to my parents for teaching me to be curious and to value knowledge. I am thankful to them for their wisdom, support, and belief in me all through my education. And thank you to my siblings for always being there for me, keeping me motivated, and in simple use of words being my great friends.

DEDICATION

To the memory of my mother,

Ferdows,

and her unwavering, eternal love.

TABLE OF CONTENTS

LIST OF FIGURES

Chapter 1

Introduction

1.1 Disordered Systems and Glass Physics of Low-frequency Spectrum

The physics of condensed systems consists of the study of large numbers of particles when they interact via relatively strong forces. Examples are ubiquitous in nature and extend from liquids to solid state structures or even living cells[1]. This physics focuses on macroscopic properties of many-body systems and hence the application of statistical techniques and mechanics is an indispensable part of this area.

Despite its wide scope of study, condensed matter physics can be grouped under two very broad categories, namely the physics of crystalline systems and disordered systems. A crystalline system is an N-dimensional pattern that is constructed by infinite repetition of identical groups (known as unit cells) in space or in time[2]. Unlike crystals, disordered materials exhibit no structural patterns on any significant scale[3]. In this context, the term "disordered system" (also known as amorphous, non-crystalline, or glassy structure) refers to a wide range of systems including glasses, disordered crystalline solids, complex fluids such as polymers, supercooled liquids, etc., where there exist significant deviations in physical properties of such systems from the crystalline systems[4].

At moderate to high temperatures, many differences in physical properties of crystalline and non-crystalline solids, such as the x-ray or neutron diffraction pattern, are immediately explained based on the structural differences of these solids at the characteristic length scale of a unit cell. However, at very low temperatures, *i.e.* near zero kelvin where the wavelength of thermally excited vibrational modes is long enough to see an average over the order and not the local structural disorder, the structural disorder becomes an irrelevant factor and one would expect similar low-temperature thermal and vibrational properties from both disordered and crystalline solids. This notion of similar low-temperature properties of disordered and crystalline structures was founded

on the hypothesis that the number and the thermal population of long wavelength phonons were independent of the translational periodicity[5,6]. However, this picture soon changed after conducting a number of low temperature experiments on glasses circa 1960[7–10].

At low temperatures and within the harmonic approximation, the vibrational properties of crystals are well described by introducing the phonons, a collection of non-interacting quasi-particles with the well-defined momentum and energy[11]. In terms of phonons, the Debye theory successfully rationalizes the universal vibrational properties of the crystalline solids. The model predicts that at low temperatures, the vibrational density of states (vDOS) follows $D(\omega) \propto \omega^2$, the heat capacity scales as $C \propto T^3$, and the thermal conductivity due to the phonons follows $\kappa \propto T^3$ where ω and T are frequency and temperature, respectively[3,12]. In contrast, at low temperatures and small frequencies, where the vibrational modes are acoustic phonons, disordered solids such as glasses or strongly perturbed crystals show a vDOS as well as thermal and transport properties that differ drastically from those predicted within the scheme of the Debye model[13–18]. This behavior is rather unexpected given that in the long wavelength limit where the continuum approximation holds ($ka \ll 1$), solid systems are expected to behave as an elastic medium where the periodicity and order of the constituent particles do not enter the picture ($k = 2\pi/\lambda$ is the wavevector and a is the interatomic distance).

We note that deviations from the harmonic approximation can happen due to multiple anharmonic contributors[3]. Here, a contrast between anharmonic contributions originating from disorder and finite temperature effects seems to be necessary. At non-vanishing temperatures two effects become relevant. The first is the growing anharmonic couplings of the constituent atoms that give rise to the finite lifetime of phonons which can be accounted for by the Boltzmann transport equation[19]. This effect can be important for both ordered and disordered solids. The second effect is associated with an interplay between disorder and the decreasing wavelength of the vibrational excitations. When the excitations happen at a wavelength comparable to the interparticle spacing, the importance of the structural order plays a role. Indeed, the existence of disorder in non-crystalline

solids adds to the complexity of anharmonic effects[†]. The interplay between the anharmonicity and disorder of the solids has been the subject of some limited investigations[19–25]. Most of the research on the differences between the crystalline and disordered solids (including the work presented in Chapter 2), however, has focused on the low temperature deviations of the disordered solids or even quasi-harmonic conditions at zero temperature to avoid the complications due to the anharmonic effects at higher temperatures[26–28].

A plausible rationalization for the low-frequency deviations of non-crystalline solids from the Debye theory has been a long standing problem in solid state physics whose answer seems to be necessary to formulate a universal theory that captures the vibrational and transport properties of such systems. In what follows, we present major vibrational and thermal anomalies of disordered solids. To this end, we focus on three problems that have been subject of much debate and are rapidly evolving.

It has been shown that at low enough frequencies, also referred to as the terahertz (THz) frequency range, the vibrational excitations in non-crystalline solids show phonon-like behaviors: they follow a Debye-like vDOS ($D(\omega) \propto \omega^2$ with a different proportionality constant), they propagate with the speed of sound, and finally they show linear dispersion relations[29,30]. For these reasons, the vibrational excitations of amorphous solids are highly akin to phonons and in many theoretical works they are treated as phonons. However, other than having a different proportionality constant, a more characteristic difference of vDOS of amorphous solids is an excess of the modes over the Debye prediction which is widely referred to as the boson peak (BP), since its temperature dependence follows that of a Bose-Einstein statistics[27]. Fig. 1.1 shows the occurrence of the BP at low frequencies and how it scales with temperature. The BP appears in many amorphous solids and supercooled liquids. We note that the BP happens in a frequency region where the dispersion relation ($\omega(k)$) for phonons remains linear. One way to define the BP, both theoretically

[†]However, as noted before, this effect should not be an issue as long as one works within the long wavelength limit.

and experimentally, is to extract the vDOS ($D(\omega)$ or $g(\omega)$ in other references) and then look for a peak in the reduced vDOS with respect to the Debye prediction, *i.e.* $D(\omega)/\omega^2$.

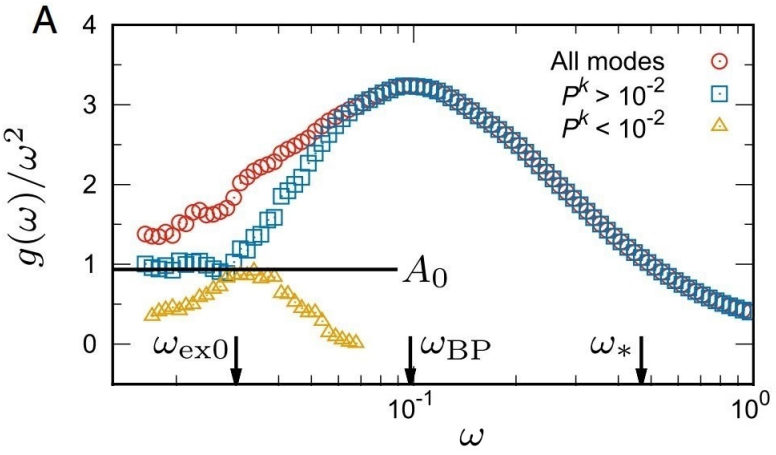

Figure 1.1: The dependence of the reduced vibrational density of states $g(\omega)/\omega^2$ on the frequency, obtained from numerical results of randomly jamming particles interacting through a pairwise potential[29]. In this figure, P^k represents the participation ratio which evaluates the extent of spatial localization of mode k. When $P^k = \mathcal{O}(1)$, it suggests modes are equally extended over all particles (phonons) and when $P^k = \mathcal{O}(1/N)$, it is indicative of localized modes (nonphonons), where N is the number of particles. As shown, the vDOS is independently calculated for modes with P^k smaller and larger than a threshold value as well as for all modes combined (red circles). By decreasing the frequency below ω_*, the boson peak emerges at the specific frequency of ω_{BP}. As the frequency is further reduced below ω_{BP}, $g(\omega)/\omega^2$ decreases more but does not reach the Debye level A_0. In this figure, ω_* is the onset frequency of the low-frequency anomalies of amorphous solids and ω_{ex0} marks a finite ω at which the extended modes converge to the Debye behavior.

Another anomaly is observed in the thermal conductivity of amorphous solids. In crystals, the thermal conductivity κ is given by,

$$\kappa = \frac{1}{3} C_V v l, \tag{1.1}$$

where C_V is the specific heat capacity, v the Debye sound velocity, and l the phonon mean free path. As a result of less frequent anharmonic umklapp events in crystals at low temperatures, the thermal conductivity increases with a decrease in the temperature which is due to an increase in the phonon mean free path. Ultimately, the increase in the mean free path reaches a maximum when l becomes comparable to the sample dimensions[10]. Therefore, as Fig. 1.2 illustrates, with lowering the temperature the change in the thermal conductivity of a crystal is well understood by

observing a maximum followed by a decrease in κ due to a decrease in heat capacity. While the conductivity of crystals is very much dependent on the chemical composition of the solid and also any disturbance of the periodicity lowers the thermal conductivity, in general and at temperatures below $\sim$ 10 K, the thermal conductivity scales as $\kappa \propto T^3$. In contrast, in amorphous solids at $T \leq 1$ K the thermal conductivity follows $\kappa \propto T^2$. This observation has led many to conclude that the vibrational excitations in non-crystalline solids are not phonons even at very low frequency of $\omega \sim 0.1$ THz which is far away from the frequency of the BP[29].

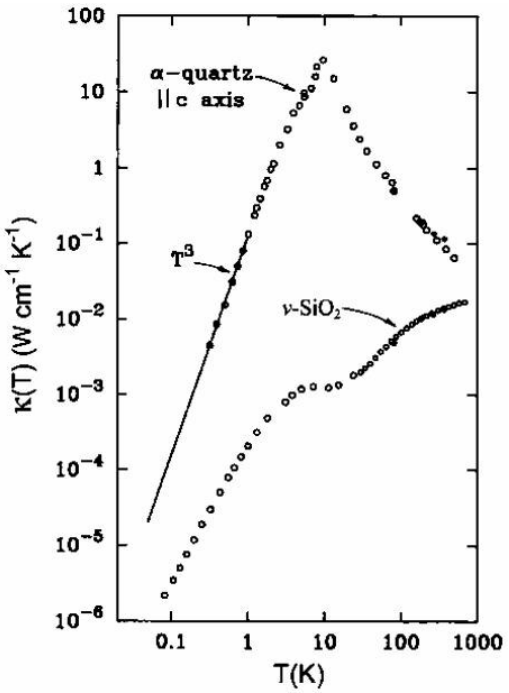

Figure 1.2: Thermal conductivity of crystalline (α-quartz) and non-crystalline (vitreous silicate) SiO_2, all measured experimentally. The figure shows that below 10 K, the thermal conductivity of a glass is several orders of magnitude smaller than its crystalline counterpart. In this experiment the heat flow in the crystal is measured parallel to the c axis[10].

Other than a different scaling of the thermal conductivity with temperature, in non-crystalline solids κ decreases monotonically with a temperature decrease. Besides, κ is independent of the chemical composition and amorphous solids such as polymers, Se, and GeO_2 show equivalent conductivities[10,31]. An immediate explanation to qualitatively understand the conductivity in amorphous solids is based on the existence of more frequent scattering events. The increase of scattering

events are due to the disordered structure of these solids. Disorder decreases the mean free path of the phonons and this in turn lowers the thermal conductivity. This explanation sounds especially plausible since adding any impurity to crystals decreases their conductivity significantly as well.

On the contrary, an observation of another vibrational deviation of amorphous solids from the Debye prediction is quite counterintuitive. Fig. 1.3 illustrates the specific heat capacities calculated from an experimental study of vDOS of SiO_2 glasses and crystals by inelastic X-ray scattering. It is observed that at ~ 10 K, glasses have an excess of the heat capacity over the Debye law where the reduced heat capacity of crystals C_p/T^3 is nearly temperature-independent. This deviation is believed to be related to the excess of the vibrational modes in the ~ 1 THz frequency range of $D(\omega)$, *i.e.* the boson peak. An early explanation for the excess of the heat capacity and the anomalous thermal conductivity of disordered solids, however, was offered by Anderson, Halperin, and Varma[32], and Phillips[33]. Based on their work, degenerate, neighboring local minima create tunneling defects or two-level systems which give rise to excess in specific heat. Such tunneling effects can be important at low-temperature range of $\sim 10 - 100$ K[15].

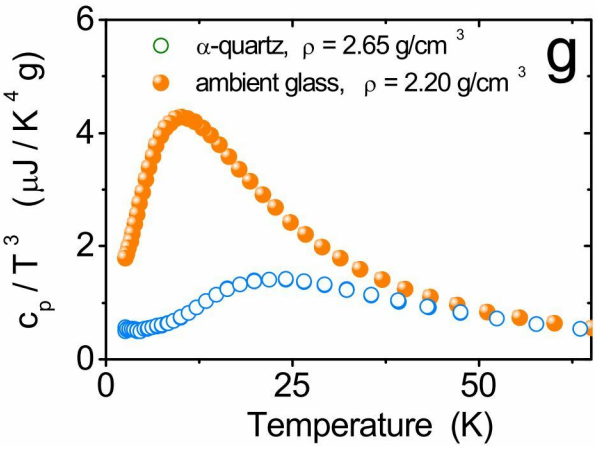

Figure 1.3: The reduced specific heat capacity C_p/T^3 obtained for non-crystalline and crystalline SiO_2. The specific heat capacities are calculated from the corresponding vDOS measured by inelastic X-ray scattering. The reduced heat capacity of the crystal remains almost a flat line at $T \leq 10$ K while the same quantity for the non-crystalline form shows a sharp peak. This peak is believed to be related to the boson peak[6].

We emphasize that the vibrational deviations of amorphous solids are not limited to the deviations from the Debye theory presented in this account. One of such anomalies is the extra damping and scattering of long-wavelength phonons in amorphous solids that has been the subject of intense investigation[17,27,34–36].

1.2 Disordered Systems and Arrested States of Active Matter

The resemblance of many mechanical and statistical properties, patterns and phenomena in Nature to the physics of glasses is remarkable. For example, an optimization problem running on a computer can turn into an arrested state of relatively good but imperfect outputs when the number of constraints are increased[37]. In this case solving for a perfect solution would become an eternal job on the computer which is reminiscent of an aging glassy system probing its potential energy surface for the most stable state. Examples of glassiness are also rich in soft condensed matter and active materials[38,39]. Active matter involves many-body systems of interacting units that are capable of pumping the stored or ambient energy into autonomous, directed motion[40–43]. Many, if not all, of the characteristics of glassy dynamics could be observed in dense active systems. Dynamic arrest becomes a feature of all active systems when there exists a competition between activity and crowding. Non-equilibrium glass transition happening at large density is another phenomenon associated with active systems[44]. The unique property of self-propelled motion in active systems is mainly associated with the living state and is observed in biological systems across different length and time scales. Standard examples at the microscale include microswimmers, bacteria, and synthetic colloidal and granular particles[41,45,46]. Assemblies of living cells with collective motions, their inracellular activity, and cytoskeletal-driven motion are also regarded as other examples of self-propelled motion[47]. At the larger scale, colonies of ants, schools of fish, flocks of birds, or even groups of mammals and crowds illustrate the collective motion.

An immediate question here would be whether these patterns and motions are system specific? Indeed, the collective motion across such broad systems of "particles" are unified under the common theme of a number of properties that are distinct from their thermal counterparts[48]. First, the

energy consumption at a single-particle level drives active systems out of the equilibrium state. This leads to the breakdown of the detailed balance at the level of a single particle which is contrary to the standard driven systems whose violation of the detailed balance is controlled through an external field gradient or boundary conditions[41,49]. However, we note that as systems far from equilibrium, the compatibility of the collective dynamics of active matter with the Onsager's reciprocal relations has been demonstrated[50–52]. Second, in active systems with an inert background medium, whose role is to constitute a passive friction, the momentum of the particles involved in a collision is not conserved[40,41,48]. On the contrary, in Newtonian mechanics of equilibrium systems, the total momentum is conserved. Third, the constituents of an active system, regardless of their interactions, tend to align their directions of motion with their neighbors (where the nature of the interactions becomes important in the symmetry and polarity of the generated current)[40,48]. This behavior is referred to as the emerging collective motion which is also the reason behind the widespread clustering tendency of active particles near repulsive walls. Fourth, as a highly debated property of active systems, it is asserted that active particles experience a non-equilibrium and athermal phase transition that is distinct from a thermal-equilibrium system[53–57].

Such unique characteristics of active motion have propelled the experimental design of active colloids with coherent and stable directed motion in the limit of low densities where hydrodynamic interactions protect a sustained active motion[58–61].

Another way to better perceive the fundamental differences between the Brownian particles (driven by thermal collisions) and active units is to look at how the stochastic equations of motion are constructed in each case. For a system of particles at thermal equilibrium, the canonical approach to system modeling is to employ the Newtonian dynamics and include all the stochastic forces: (a) write down all the contributions to the time evolution of the slow degrees of freedom; (b) include the fast-varying degrees of freedom in the form of noises; and finally, (c) employ the principle of detailed balance, *i.e.* the time reversal symmetry, to define an effective Hamiltonian that gives the stationary and dissipative parts of the dynamics[62]. Taking this approach for a Brownian particle with the unit mass, velocity $\mathbf{v}$, and a potential energy that depends solely on the spatial

coordinate $\mathbf{q}(t)$, leads to the coupled Langevin equations,

$$\frac{d\mathbf{q}}{dt} = \mathbf{v}; \quad \frac{d\mathbf{v}}{dt} = -\xi\mathbf{v} - \nabla U(\mathbf{q}) + \mathcal{F}(t). \tag{1.2}$$

Here, ξ is the Stokes friction coefficient due to the background, U is the potential energy, and $\mathcal{F}$ is the fast-varying stochastic force. Ornstein and Uhlenbeck showed that stochastic force was δ-correlated and its distribution followed a Gaussian function[63],

$$\langle \mathcal{F}(t) \rangle = 0; \quad \langle \mathcal{F}_i(t)\mathcal{F}_j(t') \rangle = 2D\delta_{i,j}\delta(t-t'), \quad i,j = x,y,z. \tag{1.3}$$

The stochastic events $\mathcal{F}_i$ are known as Gaussian white noise with their strength proportional to the coefficient $D = k_{\mathrm{B}}T\xi$ (where k_{B} is the Boltzmann's constant and T is the temperature). We emphasize that for a more evolved model of Brownian motion with spherical and relatively large particles, compared to the solvent particles, the time-invariant translational friction coefficient $\xi(t)$ leads to long-time tails in velocity autocorrelation function which scale as $t^{-3/2}$ when $t \to \infty$[64].

When far from equilibrium, we can construct a similar set of equations by ignoring the detailed balance and replacing the isotropic dissipative force with a featured force that breaks the symmetries,

$$\frac{d\mathbf{q}}{dt} = \mathbf{v}; \quad \frac{d\mathbf{v}}{dt} = \mathbf{F}_{\text{diss}} - \nabla U(\mathbf{q}) + \mathcal{F}(t). \tag{1.4}$$

This new dissipative force, $\mathbf{F}_{\text{diss}} = -\xi(\mathbf{q},\mathbf{v})\mathbf{v}$, depends on the spatial coordinates, velocity, and time. Similar to a Brownian system, here the stochastic force $\mathcal{F}$ is characterized by strength D and a δ-correlated time dependence. However, due to the system being out of equilibrium now, D is independent of the parameters in the dissipative force.

Associated with these set of Langevin equations, the solution to the Fokker-Planck equation will give the joint position and velocity distributions of the particles conditional on arbitrary initial conditions, $P(\mathbf{q},\mathbf{v},t \mid \mathbf{q}_0,\mathbf{v}_0,t_0)$,

$$\frac{\partial P\left(\mathbf{q},\mathbf{v},t \mid \mathbf{q_0},\mathbf{v_0},t_0\right)}{\partial t} = -\mathbf{v}\frac{\partial P}{\partial \mathbf{q}} - \nabla U(\mathbf{q})\frac{\partial P}{\partial \mathbf{v}} + \frac{\partial}{\partial \mathbf{v}}\left[\xi \mathbf{v} P + D\frac{\partial P}{\partial \mathbf{v}}\right]. \tag{1.5}$$

Even such a minimal modeling of an active system gives rise to fundamental deviations from a Brownian system that become evident in the position and velocity distributions. For example, in case of Rayleigh-Helmholtz model† for the friction and in the absence of an external field ($\nabla U(\mathbf{q}) = 0$), one obtains qualitatively different results for the stationary velocity of the Brownian and active particles[65]. Fig. 1.4 shows the velocity distributions for the two systems.

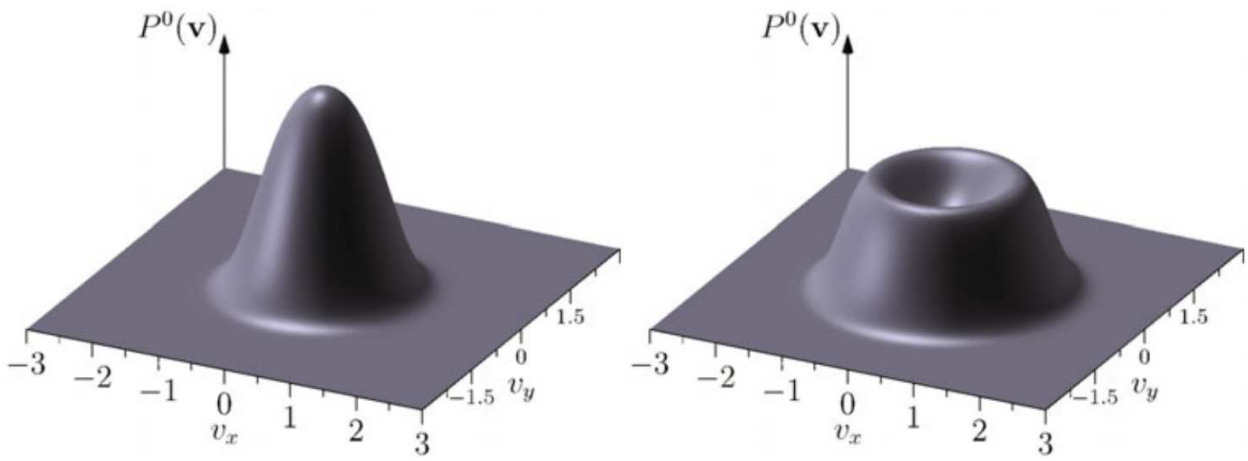

Figure 1.4: Velocity distributions in Cartesian space for Brownian (left panel) and active (right panel) systems modeled with Rayleigh-Helmholtz friction when $\nabla U(\mathbf{q}) = 0$[65]. The absence of external forces leads to stationary velocity distributions.

Let us now consider the various models of self-propelled motion. These models differ by the assumptions made on the properties of the self-propulsion velocity $\mathbf{v}$. We note that in all these models the hydrodynamic details of microswimming mechanism are abandoned and only the net displacement of the particles are considered. Yet, the models are phenomenological and successful in describing the realistic active systems. Three of such most studied models are the run-and-tumble particles (RTPs)[46], active Brownian particles (ABPs)[66,67] and active Ornstein-Uhlenbeck particles (AOUPs)[41,68].

†Rayleigh-Helmholtz model is a standard model for nonlinear friction which was originally applied to earlier studies of Brownian dynamics. In this model, the friction coefficient has a quadratic dependence on velocity.

In a run-and-tumble model, the particle's motion is characterized by sequences of "runs" which happen at a velocity with constant modulus, followed by stochastic reorientation of the velocity vector according to a specific rate, namely "tumbles". This model describes the self-propulsion of the bacteria where the runs have varied length and the tumbles are isotropic[69]. The active Brownian particles also have a constant-modulus velocity, yet the angular dynamics of the particles is controlled through free diffusion and the translational and rotational degrees of freedom are coupled. The self-propulsion in this case follows the formal expression for the velocity $\mathbf{v} = v_0 \left(\cos(\phi), \sin(\phi)\right)$ with ϕ being the angular degree of freedom. The model describes the motion of synthetic or biological active particles with asymmetric chemical or physical features such as chirality or helicity as well as particles with a circular trajectory, or self-phoretic Brownian particles[41,70]. For example, ABPs can model certain groups of bacteria, sperm cells, or self-propelled Janus colloids[56,58,70]. The dynamics of AOUPs differ from RTPs and ABPs by existence of a fluctuating norm of the self-propulsion velocity that varies according to an Ornstein-Uhlenbeck process. This class of particles can model the collective dynamics of cells as well as the motion of passive tracers in an active medium. For a group of AOUPs, the self-propulsion velocities $\{\mathbf{v}_i\}$ form a set of stochastic processes characterized by their zero-mean colored Gaussian noise with the following correlations[68,71],

$$\langle v_i(t) v_j(t') \rangle = \delta_{ij} \frac{D}{\tau} \mathrm{e}^{-|t-t'|/\tau}, \tag{1.6}$$

where the indices denote different particles and D is the strength of the noise. The noise correlation time τ, also known as the persistence time, describes the relaxation time of the Ornstein-Uhlenbeck processes. In the limit of $\tau \to 0$, the correlation of Gaussian white noise is recovered and the dynamics of the particles approaches that of an equilibrium state. Thus, the noise correlation time τ is a parameter indicative of how far an active system is from the equilibrium state. In this context, we consider time scales much longer than the decay time of the velocity autocorrelation function of a system in thermal equilibrium.

Finally, we note that in contrast to an equilibrium system whose dynamics is described by Gaussian white noise, in all models of active systems the statistics of the self-propulsion (*i.e.* $\mathbf{v}$'s) is non-Gaussian.

1.3 Chapter Overview

As I tried to outline in the previous sections, the physics of disordered systems can bring different facets of seemingly independent phenomena together to provide a more universal picture of the problem in hand. My research was also an attempt in this direction. One part of my research was an address to the low-frequency properties of a wide range of glasses from ultra-stable glasses to relatively stable ones. This research which relied on numerical simulations is briefly reviewed in the following Sec. 1.3.1. Another part of my research focused on theoretical and numerical descriptions of a model class of active particles discussed earlier, namely AOUPs. This is also briefly reviewed in Sec. 1.3.2.

1.3.1 Low-frequency Properties of Stable Glasses Within the Framework of Fluctuating Elasticity Theory

Many theories have shaped around the distinct vibrational and/or structural characteristics of disordered solids to account for the low-frequency deviations of disordered solids from the predictions of the Debye theory. The theory of softening of acoustic phonons (vibrational excitations) by stationary disorder[72], the existence of quasi-localized modes and their hybridization with phonon modes[35], and the soft potential model and the effects of anharmonicity at low frequencies[73], are among some of these theories.

One such theory based on the structural differences of amorphous solids is the Fluctuating Elasticity Theory (FET). Originally proposed by Schirmacher, the theory focuses on the random fluctuations of transverse (shear) and longitudinal (bulk) elastic constants in amorphous materials[74–76]. When the local shear (or bulk) modulus[†] of an amorphous solid is measured, the respec-

[†]The details of local elastic moduli calculations are presented in Chapter 2.

tive quantity typically has a normal distribution[77–79]. In contrast, for crystals the strength of elastic moduli in the lattice remains uniform and forms a delta function probability distribution. Due to its formulation and nontrivial measurable parameters defined in it, the FET is mostly applied to sound attenuation and dissipation of vibrational modes[21,34,80].

In the work presented in Chapter 2, we aimed to probe the assumption that whether there existed a correlation between the fluctuations in the elastic matrix of an amorphous medium and its stability. This is a basic implication of the FET. To meet this objective, we numerically simulated a broad range of ultra-stable to moderately stable amorphous solids starting from the respective configuration of the solid in a supercooled liquid phase. All the calculations were performed for near-zero temperature solids to investigate the low-temperature properties of the solid and to rule out the anharmonic contributions of the vibrational modes. We measured the shear and bulk moduli for local domains of the solid and in accordance with the predictions of the FET, we concluded that with increasing the stability of the solid there was a reduction in the fluctuation of both shear and bulk elastic constants. Furthermore, we were interested to examine the spatial correlations in the elastic matrix. We expected to see these correlations, which enter into the FET, for our most homogeneous system, *i.e.* the most stable glass studied. In contrast to the FET, we found that there were no finite-range spatial correlations within the elastic matrix itself.

1.3.2 Density Distribution of AOUPs in the Presence of an External Potential

As pointed out earlier, active particles are non-equilibrium systems for which we do not have a distribution function to determine the moments and cumulants of the statistics. In principle, we would need to derive an exact or approximate expression for the many-particle distribution to calculate the measurable properties of the system. Nonetheless, studying a minimal or a single-particle system has the benefit of pinpointing the effective active particle properties that are independent from the collective motion of the particles in a dense phase. Besides, there is evidence in support of the idea that we can reduce the many-body problem into a single-particle system. For

instance, assuming pair additivity, most of the properties of interest of many-particle systems can be expressed in terms of a reduced distribution function such as the pair distribution function, $g(r)$, which not only provides us with a structural insight but also makes the direct evaluation of the thermodynamic quantities of the system possible[81,82]. With that motivation, single-particle active systems have also been investigated both theoretically and experimentally[83–85].

Similarly, we were interested to determine an exact analytical expression for the stationary distribution function of a tracer particle in a model of interacting AOUPs. We study this model under the influence of an external potential that acts exclusively on the tracer particle. This would allow us to write the position distribution as a perturbative solution. This would also allow us to test the theory beyond the linear response regime for an arbitrary potential with varied amplitudes. Interestingly, our analytical results showed that the distribution function of the tracer particle had a form analogous to that of an equilibrium system, *i.e.* the Boltzmann distribution, with an effective temperature replacing the heat bath temperature in the distribution function. The effective temperature followed the form of the Einstein temperature (where the latter defines the temperature of a colloidal system within the linear response regime as the ratio of two transport coefficients, the mobility and the self-diffusion coefficients). In another part of this research, we used numerical simulations to support the analytical findings. This work is presented in Chapter 3.

In Chapter 4, we discuss our results on the density distribution of an AOUP in a tilted periodic potential. Numerous recent theoretical and experimental studies have focused on the behavior of active particles in the presence of external fields and confinements[83,86–90]. In this work, we derive an analytical expression for the stationary density function and the current/mean velocity of an AOUP within the unified colored-noise approximation (UCNA)[91]. The density function, which is derived for a particle under the influence of a tilted periodic potential, is numerically tested in a state-space of varied temperature, persistence time, and strength of the tilting force. For small to moderate tilting force, we showed that the analytical results were in agreement with the numerical simulations across systems with different temperatures and $\tau_{\mathrm{p}} \leq 1.0$. However, at higher amplitudes of the tilting force we found that the theoretical density function overestimates

the asymmetric effect of the tilting force on the probability density distribution. In the second part of this study, we simulated the mean velocities and self-diffusion coefficients of active and Brownian particles under the influence of a tilted external potential. Consistent with the reported results for a non-interacting Brownian system, we found that both the mean velocity and self-diffusion coefficient of an AOUP are considerably enhanced in the presence of a tilting periodic potential. We further determined that the theoretical expression for the mean velocity quantitatively predicts the results of the numerical simulations at different temperatures as long as $\tau_p \leq 1.0$.

Finally, in Chapter 5, we summarize the main findings and conclude with a brief discussion on the possible avenues for future work.

Chapter 2

Stability dependence of local structural heterogeneities of stable amorphous solids.[†]

2.1 Overview

The universal anomalous vibrational and thermal properties of amorphous solids are believed to be related to the local variations of the elasticity. Recently it has been shown that the vibrational properties are sensitive to the glass's stability. Here we study the stability dependence of the local elastic constants of a simulated glass former over a broad range of stabilities, from a poorly annealed glass to a glass whose stability is comparable to laboratory exceptionally stable vapor deposited glasses. We show that with increasing stability the glass becomes more uniform as evidenced by a smaller variance of local elastic constants. We find that, according to the definition of local elastic moduli used in this work, the local elastic moduli are not spatially correlated.

2.2 Introduction

The vibrational modes and the low temperature thermal properties of amorphous solids are sharply different from those of their crystalline counterparts[10,92–94]. The uniform structure of crystals allows for the description of the low frequency modes as if it were a classical elastic body whose properties are governed by the elastic moduli, which forms the basis of the Debye model for the density of states. This description leads to a T^3 increase of the specific heat for crystalline solids due to the increase of the density of the vibrational modes as the square of the frequency ω. Recently it was shown that the low frequency vibrational modes of amorphous solids can be divided into a Debye term and an excess contribution that increases as the fourth power of the

[†]This chapter was previously published and is reproduced here with minor modifications. See: A. Shakerpoor, E. Flenner, and G. Szamel, Stability dependence of local structural heterogeneities of stable amorphous solids, *Soft Matter* **2020**, *16*, 914.

frequency[18,29]. The excess modes are spatially quasi-localized. Their spatial extent and density decrease with increasing stability. The quasi-localized character of excess modes suggests that there might be a spatially varying local elasticity.

Indeed, there is a large body of evidence for the existence of spatially varying local elastic constants in amorphous solids[17,78,79,95–104]. To explain a plateau observed in the thermal conductivity around 10K for many dielectric amorphous solids, a Rayleigh like scattering of sound waves was assumed[10,94]. This assumption posits scattering from uncorrelated defects that are much smaller than the wavelength of the sound wave, and these defects would naturally give rise to local variations of the elasticity. Further theoretical analysis assuming local variations of the elasticity reproduces the ω^4 excess in the vibrational density of states and predicts the Rayleigh scaling k^4 (where k is a wavevector) of sound attenuation[18,21,80,105]. The k^4 scaling of sound attenuation was questioned in a computer simulation study[100] and a logarithmic correction to the Rayleigh scaling was proposed. This correction was rationalized in terms of a power law decay of the spatial correlations of the local elasticity. However, other simulation studies[18,105,106] suggest that the logarithmic correction either exists only for a narrow range of wavevectors (frequencies) or this correction is only a good description of the crossover region between the high and low wavevector (frequency) behavior of sound attenuation.

Pogna *et al.*[104] examined sound attenuation in geologically hyperaged, ultrastable amber within the framework of fluctuating elasticity theory to establish a link between stability and the local variation of the elastic constants. They fitted the predictions of the theory for the vibrational density of states to the experimental data and in this way obtained estimates of the relative variance of the local elastic constants and of a length scale characterizing their spatial variation. They concluded that there was a reduction in the variation of the elastic constants by around 6% and an increase of the characteristic length scale of around 22% in the hyperaged amber compared to a liquid cooled sample. Thus, increasing stability seemingly narrows the distribution of elastic constants and increases the range of their correlations.

However, in a very recent simulational study Caroli and Lemaitre[17] argued that the fluctuating elasticity theory does not describe well sound attenuation in amorphous solids. They based this conclusion on two results. First, they showed that the fluctuating elasticity theory predicts the k^4 Rayleigh scattering-like sound damping whereas their simulations were consistent with a logarithmic correction. Second, they measured the parameters that enter into the fluctuating elasticity theory in simulations, used them to calculate sound attenuation, and compared these predictions with sound attenuation observed in the same simulations. They found that the predicted sound attenuation is two orders of magnitude smaller than the observed one. The second fact implies that the fluctuating elasticity theory severely underestimates the magnitude of the sound attenuation even if one were to argue that the logarithmic corrections is an intermediate, finite wavevector feature and the sound attenuation can be described within the Rayleigh scattering picture.

We note that it is difficult to directly probe local variations of the elasticity in experiments[78], which forced Pogna *et al.* to treat the relative variance of the local shear modulus as a fitting parameter. In contrast, simulations are able to calculate local elastic constant using several different methods[79,100,105]. Lerner demonstrated that the sample to sample fluctuations of the shear modulus decreased with increasing stability for a model glass former[107], but did not examine the local elastic constants. Mizuno, Mossa, and Barrat found that the width of the distribution of local elastic constant correlates with sound attenuation[99]. For their study, they continuously transformed a crystal into an amorphous solid by continuously changing the size ratio of a binary mixture. Using the same technique they also demonstrated that the thermal conductivity, the lifetime of acoustic modes, and the local elastic heterogeneity are correlated[95]. This investigation, however, does not mimic the experimental procedure of Pogna *et al.*[104] who studied the stability dependence of sound attenuation. Importantly, in the work of Mizuno, Mossa, and Barrat the system is changed systematically in order to establish the correlations between the transport and acoustic properties and the variation of local elastic constants.

Here we examine the dependence of local elastic moduli of a simulated polydisperse glass former on its stability. We partition the system into different box sizes w and determine the dis-

tribution of local elastic moduli for three values of w. We find that the width of the distribution decreases with increasing stability. However, using our definition of the local elastic moduli, we find that the local elastic moduli are uncorrelated in space.

2.3 Methods

2.3.1 Molecular Dynamics Simulations

We studied a system of $N = 48000$ and $N = 192000$ polydisperse repulsive particles in a cubic box of volume V with periodic boundaries in 3D. The pair potential is given by

$$U(r_{ij}) = \begin{cases} \epsilon \left(\frac{\sigma_{ij}}{r_{ij}}\right)^{12} + v(r_{ij}), & \frac{\sigma_{ij}}{r_{ij}} < r_{\text{cut}} \\ 0, & \frac{\sigma_{ij}}{r_{ij}} \geq r_{\text{cut}} \end{cases} \tag{2.1}$$

with

$$v(r_{ij}) = c_0 + c_2 \left(\frac{r_{ij}}{\sigma_{ij}}\right)^2 + c_4 \left(\frac{r_{ij}}{\sigma_{ij}}\right)^4. \tag{2.2}$$

The distance between particle i and particle j is $r_{ij} = |\mathbf{r}_i - \mathbf{r}_j|$, $\sigma_{ij} = \frac{\sigma_i + \sigma_j}{2}(1 - e|\sigma_i - \sigma_j|)$ where the mixing parameter $e = 0.2$[18,108]. The sizes of individual particles σ are given by the probability distribution

$$P(\sigma) = \frac{A}{\sigma^3} \tag{2.3}$$

where $\sigma \in [0.73, 1.63]$ and zero otherwise. The coefficients c_0, c_2, and c_4 are chosen to guarantee the continuity of the potential up to the second derivative at the cutoff distance $r_{\text{cut}} = 1.25$. This choice of system inhibits crystallization due to the polydispersity and fractionation due to the non-additive mixing rule, while allowing the swap Monte Carlo algorithm to equilibrate to low temperatures[108]. We present the results in reduced units with ϵ being our unit of energy, the average of $\sigma = \sigma_0$ being our unit of length, and $\sqrt{m\sigma_0^2/\epsilon}$ being the unit of time.

For each parent temperature $T_{\text{p}} \in [0.062, 0.200]$ we studied 4 independent initial configurations at number density $\rho = 1$. Each configuration was first equilibrated at its parent temperature and

then quenched to an inherent structure via the conjugate gradient algorithm. For reference, for our system the mode-coupling temperature $T_{\text{MCT}} \approx 0.108$ and the glass transition temperature $T_g \approx 0.072$[108]. The equilibration was done using the swap Monte Carlo algorithm that combines conventional Monte Carlo moves with particle swaps[108–110].

After quenching, we ran very low temperature NVT molecular dynamics simulations using LAMMPS[111,112] code to which we added the interaction potential for the present model. The time step for all of MD simulations was $dt = 0.02$. We first ran short equilibration runs at $T = 10^{-5}$ in an NVT ensemble using a Nosé-Hoover thermostat. We then ran NVT production runs. Their length was determined by the time needed to decorrelate a term involving the local and global stress $\left\langle \sigma^m_{\alpha\beta}\sigma_{\gamma\delta} \right\rangle$, which was identified as a slowly decorrelating term and discussed by Mizuno *et al.*[79]. This term is defined in Section 2.3.2. We did not observe any finite size effects, but, consistent with the observation made in Ref. [79], much longer production runs are needed for larger systems. For a system of $N = 48000$ particles, which was mainly used to perform the elastic modulus calculations in this study, the length of the production runs time was $\Delta t = 3 \times 10^5$, which corresponds to 1.5×10^7 time steps. The results shown in the paper are for the $N = 48000$ particle system unless otherwise specified. We observed very infrequent jumps in the energy and the pressure even at the very low temperature that we used, $T = 10^{-5}$. We attribute these jumps to transitions between the locally stable minima. In the analysis we only use a continuous portion of the trajectory that excludes the energy jumps.

2.3.2 Elastic Modulus Calculations

To measure the local elastic response, the system is equally partitioned into cells of size $w = 3.30$, 4.54, 6.05, and 12.11. Several methods have been proposed to define and calculate the local elastic constants. Here we use the so-called "fully local" approach described by Mizuno, Mossa, and Barrat[79]. This approach was also used in other studies[95,99,102]. For each box m the volume averaged stress tensor is calculated as:

$$\sigma^m_{\alpha\beta} = -\rho^m T\delta_{\alpha\beta} + \frac{1}{w^3}\sum_{i<j}\frac{\partial U(r^{ij})}{\partial r^{ij}}\frac{r^{ij}_\alpha r^{ij}_\beta}{r^{ij}}\frac{q^{ij}_m}{r^{ij}} \tag{2.4}$$

where, ρ^m is the local number density of cell m, T is the temperature, δ is the Kronecker delta and $r_{ij} = |\mathbf{r}_i - \mathbf{r}_j|$. Here, the first term on the right-hand side shows the kinetic/ideal gas contribution to the bulk modulus. The parameter q^{ij}_m is the segment of the line joining $\mathbf{r}_i$ and $\mathbf{r}_j$ that lies within the box m. We use Greek subscripts to denote the Cartesian coordinates ($\alpha, \beta, \gamma, \delta = x, y, z$) and Roman superscripts to denote particle labels. The global stress tensor is given by:

$$\sigma_{\alpha\beta} = \frac{1}{V}\sum_m w^3\sigma^m_{\alpha\beta} = -\hat{\rho}T\delta_{\alpha\beta} + \frac{1}{V}\sum_{i<j}\frac{\partial U(r^{ij})}{\partial r^{ij}}\frac{r^{ij}_\alpha r^{ij}_\beta}{r^{ij}}. \tag{2.5}$$

We first calculate the local modulus $C^m_{\alpha\beta\gamma\delta}$ given by

$$\begin{aligned}
C^m_{\alpha\beta\gamma\delta} &= C^{Am}_{\alpha\beta\gamma\delta} - C^{Nm}_{\alpha\beta\gamma\delta} \\
&= C^{Bm}_{\alpha\beta\gamma\delta} + C^{Cm}_{\alpha\beta\gamma\delta} + C^{Km}_{\alpha\beta\gamma\delta} - C^{Nm}_{\alpha\beta\gamma\delta} \\
C^{Bm}_{\alpha\beta\gamma\delta} &= \frac{1}{w^3}\left\langle\sum_{i<j}\left(\frac{\partial^2 U}{\partial {r^{ij}}^2} - \frac{1}{r^{ij}}\frac{\partial U}{\partial r^{ij}}\right)\frac{r^{ij}_\alpha r^{ij}_\beta r^{ij}_\gamma r^{ij}_\delta}{{r^{ij}}^2}\frac{q^{ij}_m}{r^{ij}}\right\rangle \\
C^{Cm}_{\alpha\beta\gamma\delta} &= -\frac{1}{2}\Big[2\left\langle\sigma^m_{\alpha\beta}\right\rangle\delta_{\gamma\delta} - \left\langle\sigma^m_{\alpha\gamma}\right\rangle\delta_{\beta\delta} \\
&\quad - \left\langle\sigma^m_{\alpha\delta}\right\rangle\delta_{\beta\gamma} - \left\langle\sigma^m_{\beta\gamma}\right\rangle\delta_{\alpha\delta} - \left\langle\sigma^m_{\beta\delta}\right\rangle\delta_{\alpha\gamma}\Big] \\
C^{Km}_{\alpha\beta\gamma\delta} &= 2\left\langle\hat{\rho}^m\right\rangle T\left(\delta_{\alpha\gamma}\delta_{\beta\delta} + \delta_{\alpha\delta}\delta_{\beta\gamma}\right) \\
C^{Nm}_{\alpha\beta\gamma\delta} &= \frac{V}{T}\left(\left\langle\sigma^m_{\alpha\beta}\sigma_{\gamma\delta}\right\rangle - \left\langle\sigma^m_{\alpha\beta}\right\rangle\left\langle\sigma_{\gamma\delta}\right\rangle\right),
\end{aligned} \tag{2.6}$$

where $C^{Am}_{\alpha\beta\gamma\delta}$ is the affine contribution and $C^{Nm}_{\alpha\beta\gamma\delta}$ is the non-affine contribution. While the non-affine contribution vanishes in perfect crystalline systems at zero temperature, it has a magnitude comparable to the affine term in amorphous systems[113]. The brackets $\langle\cdots\rangle$ denotes an ensemble average. The Born contribution $C^{Bm}_{\alpha\beta\gamma\delta}$ to the affine term stems from the uniform displacement of all particles and it determines the instantaneous elastic modulus under such displacements[96]. The $C^{Cm}_{\alpha\beta\gamma\delta}$ term is due to the initial stress having a finite value[79]. The $C^{Km}_{\alpha\beta\gamma\delta}$ term is the kinetic energy

contribution to the local elastic modulus tensor. Compared to the Born and the non-affine terms, the kinetic energy contribution to the elastic constant is negligible.

As described by Mizuno *et al.*[79], the local bulk modulus K^m is defined from the pressure-volume change and the five shear moduli $G_1^m, \cdots, G_5^m$, are defined from two pure shear and three simple shear deformations. These moduli are given by the following linear combinations of $C^m_{\alpha\beta\gamma\delta}$

$$\begin{aligned}
K^m &= \left(C^m_{xxxx} + C^m_{yyyy} + C^m_{zzzz}\right. \\
&\quad \left. + C^m_{xxyy} + C^m_{yyxx} + C^m_{xxzz} + C^m_{zzxx} + C^m_{yyzz} + C^m_{zzyy}\right)/9 \\
G_1^m &= \left(C^m_{xxxx} + C^m_{yyyy} - C^m_{xxyy} - C^m_{yyxx}\right)/4 \\
G_2^m &= \left[C^m_{xxxx} + C^m_{yyyy} + 4C^m_{zzzz}\right. \\
&\quad \left. + C^m_{xxyy} + C^m_{yyxx} - 2\left(C^m_{xxzz} + C^m_{zzxx} + C^m_{yyzz} + C^m_{zzyy}\right)\right]/12 \\
G_3^m &= C^m_{xyxy} \\
G_4^m &= C^m_{xzxz} \\
G_5^m &= C^m_{yzyz}. \qquad (2.7)
\end{aligned}$$

The moduli are averaged over MD configurations that are separated by $t = 0.5$, *i.e.* over 6×10^5 time steps.

2.4 Results

Shear and bulk moduli describe the elastic response of the system to a small deformation. In simulations one can determine these moduli through a deformation, or utilize the thermodynamic equations summarized in Eqns. (2.6-2.7) for the whole system, *i.e.* when the system is only partitioned into one box. Here, we partition the system into several boxes and determine distributions of the moduli. We expect that the averages of these distributions should be equal to the values of the moduli obtained from deformation. To check this, we calculated the averages of the moduli for different box sizes w and compared these results to the shear and bulk moduli obtained from deformation.

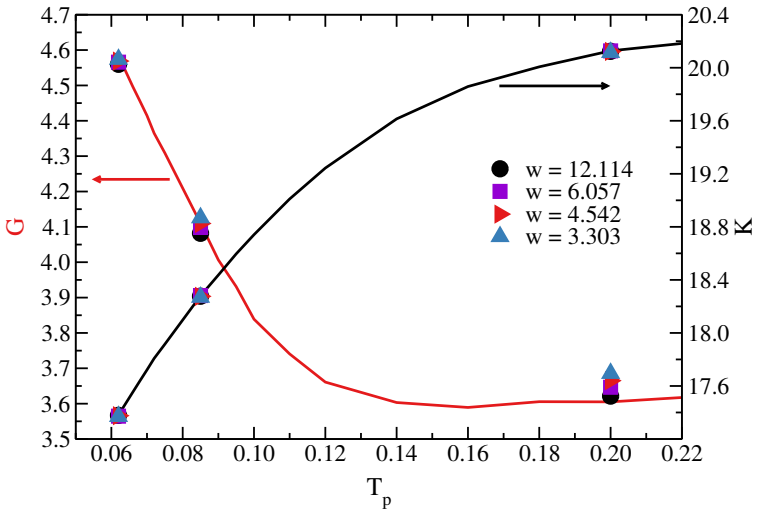

Figure 2.1: Macroscopic shear (red line) and bulk (black line) moduli obtained by deforming the zero temperature (quenched) configurations as functions of the parent temperature. The symbols show the averages of the local shear and bulk moduli for different box sizes. The errorbars for the local moduli averages, not shown here, are smaller than or comparable to the size of the symbols.

Shown in Fig. 2.1 are the shear modulus (left axis) and the bulk modulus (right axis) obtained from deforming the system (lines) and from the averages of the distributions of the local moduli (symbols) for different box sizes. Up to the mode coupling temperature $T_{\rm MCT}$ the global shear modulus G changes very little with decreasing parent temperature $T_{\rm p}$. Below $T_{\rm MCT}$ it increases with decreasing $T_{\rm p}$, reaching a value approximately 27% larger at the lowest parent temperature used. In contrast, the global bulk modulus K monotonically decreases with decreasing $T_{\rm p}$, reaching a value 7% smaller at the lowest parent temperature than at $T_{\rm MCT}$. The averages of the local shear $G^{\rm m}$ and bulk $K^{\rm m}$ moduli for different box sizes are very close to the moduli obtained from deformation. We do find, however, that at the largest parent temperature the averages of the shear moduli are slightly larger than the value obtained from deformation, with the difference increasing systematically with decreasing box size.

We note that, as shown in Fig. 2.2, for both of the global shear and the global bulk moduli the Born and fluctuation terms in $C_{\alpha\beta\gamma\delta}$ decrease with decreasing $T_{\rm p}$. For the shear modulus, the fluctuation term decreases faster with decreasing T_p than the Born term, and this leads to the increase in the shear modulus since the two terms are the same order of magnitude. However, for

the bulk modulus the fluctuation term is an order of magnitude smaller than the Born term, and thus a decrease in the Born term leads to a decrease of the bulk modulus.

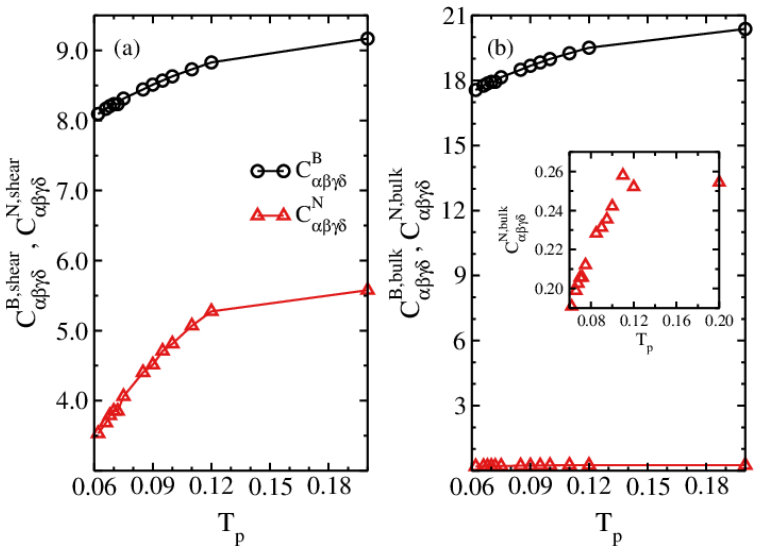

Figure 2.2: The dependence of the Born and fluctuation terms on the parent temperature. Inset: rescaled data for the bulk fluctuation term. Both Born and fluctuation terms decrease with decreasing parent temperature, for both shear (a) and bulk (b) moduli.

Although the average shear and bulk moduli are approximately independent of the box width w, one would expect to find some box width dependence of the width of the moduli distributions. The dependence of the width of the distribution relative on the box size is an important parameter in the fluctuating elasticity theory. Mizuno *et al.* found that the distributions of the individual shear moduli are almost identical and presented distributions averaged over the individual components. We found that the same fact is true for our system and also present distributions of the shear moduli averaged over the individual components.

Shown in Fig. 2.3 are probability distributions of the local shear modulus $G^{\rm m}$ calculated for (a) w = 12.114, (b) w = 6.057, (c) w = 4.543, and (d) w = 3.303 for three parent temperatures T_p = 0.062 (circles), 0.085 (squares), and 0.2 (triangles). We note that we observe no finite size effects, which we demonstrate in the inset to Fig. 2.3(d) by calculating the distribution for $N = 48000$ and $N = 192000$ for a box of the same size. However, as discussed in Ref. [79], the $\left\langle \sigma^m_{\alpha\beta}\sigma_{\gamma\delta}\right\rangle$ term converges very slowly for large systems. To characterize the width we fit the distributions to

a Gaussian distribution, $A\exp\{-0.5(G-G_0)^2/\sigma^2\}$, where G_0 is the average shear modulus and σ is the standard deviation. The fits are shown as continuous lines in the figures. For all box sizes, including the smallest one with $w = 3.303$ that only contains $\simeq 36$ particles, the shear moduli distributions are well described by Gaussian distributions.

We can see two trends. First, with increasing stability the distribution becomes narrower. This is easily seen since the peak of the distribution increases with decreasing width due to normalization of the distributions. Therefore, with increasing stability the glass becomes more uniform, in the sense that the local shear moduli vary less between different boxes. The other trend is that the width becomes broader with decreasing box size. This result is intuitively expected.

One noticeable property of some of these distributions is the appearance of regions with negative moduli. The regions with negative moduli are characterized as domains where the deforming force and the resulting response are in opposite directions[114], which suggests that these domains are unstable. However, with such small domains it is questionable if continuum elasticity is a valid description[113]. Overall, at each box size the distributions with higher averages and smaller standard deviations (*i.e.* the distributions of $T_{\rm p} = 0.062$) represent the more stable structure[101].

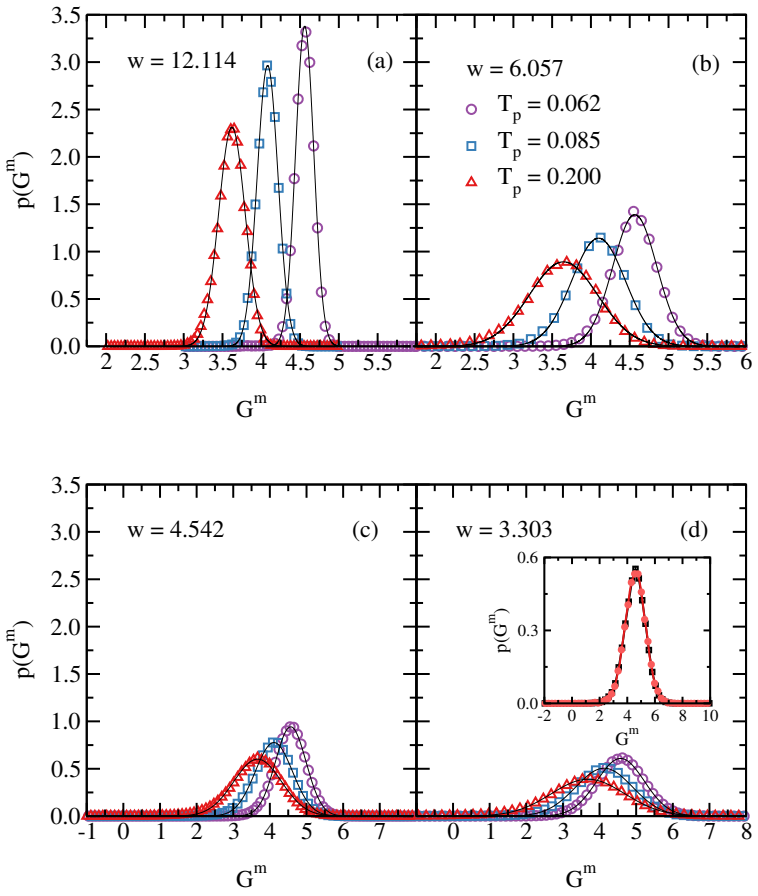

Figure 2.3: Distributions of local shear moduli for different box sizes: (a) $w = 12.114$, (b) $w = 6.057$, (c) $w = 4.542$, (d) $w = 3.303$. Each panel shows distributions for three different parent temperature, circles, $T_p = 0.062$, squares, $T_p = 0.085$ and triangles $T_p = 0.200$. The solid lines show Gaussian fits to the distributions.

We also examined the distribution of the bulk modulus $K^{\rm m}$, Fig. 2.4 for the same three parent temperature $T_{\rm p}$ and box sizes w. We also find that the width of the distribution of $K^{\rm m}$ decreases with decreasing parent temperature and increases with decreasing box size. The lines in the figures are fits to a Gaussian distribution. Again, these results points to the bulk modulus becoming more uniform with an increase of the stability. Since the bulk modulus is 3.5 to 5.5 times larger than the shear modulus (depending on stability), the change in the relative size of the distribution σ_Γ/Γ, where $\Gamma = G$ or K is much less for the bulk modulus.

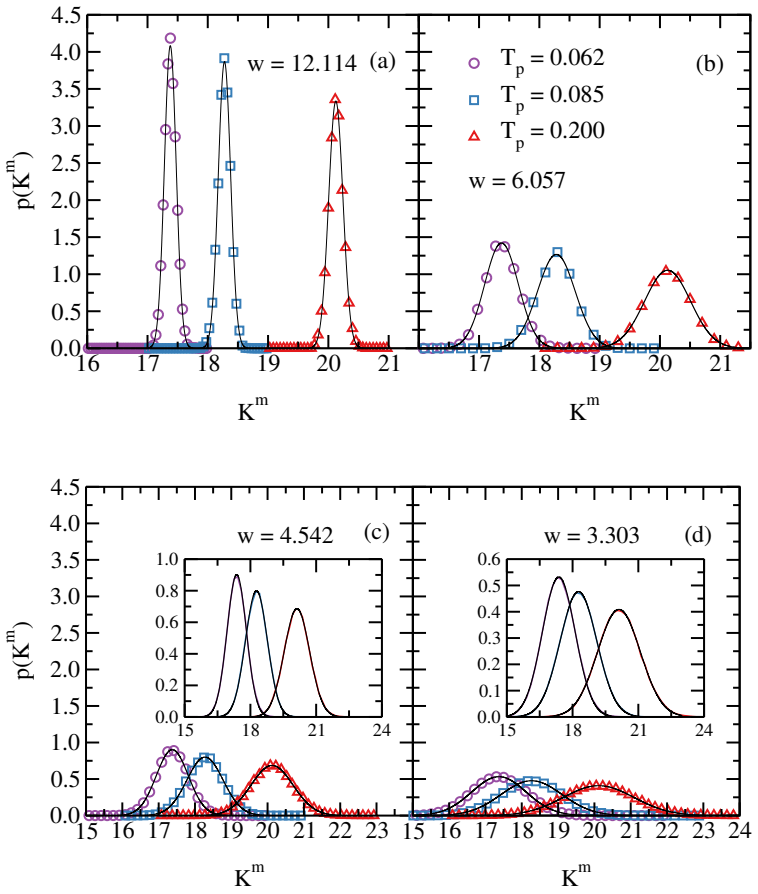

Figure 2.4: Distributions of local bulk moduli for different box sizes: (a) $w = 12.114$, (b) $w = 6.057$, (c) $w = 4.542$, (d) $w = 3.303$. Each panel shows distributions for three different parent temperature, circles, $T_p = 0.062$, squares, $T_p = 0.085$ and triangles $T_p = 0.200$. The solid lines show Gaussian fits to the distributions. Insets: the same distributions as the main panels plotted on a different y-scale for clarity.

We summarize the parent temperature and box size dependence of the standard deviation of the distributions of the local moduli in Fig. 2.5. The closed symbols are the results for the shear moduli and the open symbols are results for the bulk modulus. The increase in σ_{G^m} upon decreasing the box of size from w = 12.114 to w = 3.303 is a factor of 5.5 for T_p = 0.2 and 5.8 for T_p = 0.062. Similarly, the decreases of σ_{G^m} with parent temperature for a fixed box size is 31% for w = 12.114 and 35% for w = 3.303.

Within fluctuating elasticity theory[74,76,80], the heterogeneity of local shear modulus is characterized by the disorder parameter γ_G, $\gamma_G = \rho w^3 \sigma^2_{G^m} / \langle G^m \rangle^2$. We calculated this parameter for the different box sizes. We found that the disorder parameter varies with box size. For our most stable

glass, $T_p = 0.062$, $\gamma_G = 1.24$ for $w = 12.1$ and $\gamma_G = 0.90$ for $w = 3.3$. These two values of the disorder parameters differ by approximately 38%. This box size dependence of the disorder parameter originates from slower than w^{-3} decay of the variance $\sigma^2_{G^m}$ upon increasing the box size w. It makes it unclear if γ_G is a proper parameter to be used as input to a theory of sound attenuation in glasses. We note that Lerner[107] found that a quantity which should be equivalent to the square root of the variance (see Eq. (18) of Ref. [107]) of the sample-to-sample fluctuations of the shear modulus decreases with the size of the system as $N^{-1/2}$. The difference between our results and those of Ref. [107] suggests that the distribution of local shear modulus calculated for a given sample might be different from the distribution of sample-to-sample fluctuations of the shear modulus calculated for the whole system.

The disorder parameter does increase dramatically with decreasing stability for a fixed box size. The disorder parameter increases by a factor of 3.4-3.9, depending on box size, when we compare our most stable glass, $T_p = 0.062$, to our least stable glass, $T_p = 0.2$. For our least stable glass, disorder parameters are of similar magnitude as those found by Mizuno, Ruocco, and Mossa[115] in their $T = 0$ glass.

We note that the change in the variation of the local elastic moduli, *i.e.* of the heterogeneity of the local elasticity, with the changing stability found in this work is much larger than that estimated by Pogna *et al.* for hyperaged amber. In the latter study a decrease of only 5% was estimated upon a very large increase in the stability. We note that the change in the variation of the elastic constants reported by Pogna *et al.* was obtained indirectly, by fitting measured vibrational densities of states to the predictions of the fluctuating elasticity theory. Thus, the accuracy of their inferred change of the variation of the local elastic moduli depends on accuracy of the fluctuating elasticity model that they used. We find that there is probably a stronger dependence of the variation of the elastic constants on the glass' stability than that inferred from fluctuating elasticity theory.

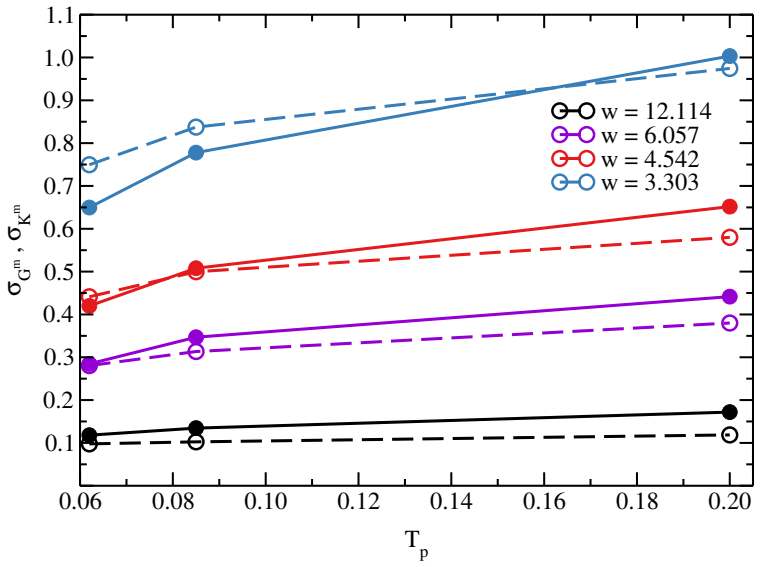

Figure 2.5: Dependence of the standard deviation of the local shear, $\sigma_{\mathrm{G^m}}$, and bulk moduli, $\sigma_{\mathrm{K^m}}$, on the parent temperature. The solid lines and filled symbols show $\sigma_{\mathrm{G^m}}$ and the dashed lines and open symbols show $\sigma_{\mathrm{K^m}}$. The standard deviation $\sigma_{\mathrm{G^m}}$ increases by 67% for our smallest box size $w = 3.303$ and 50% for our largest box size $w = 12.114$. The standard deviation $\sigma_{\mathrm{K^m}}$ increases by 33% for our smallest box size and 7.1% for our largest box size. Since $K > G$, this signifies a much larger relative change in $\sigma_{\mathrm{G^m}}$ than $\sigma_{\mathrm{K^m}}$.

To characterize the spatial correlations of local shear moduli, which also enter into the fluctuating elasticity theory[21], we calculated the correlation function

$$g_{GG}(r) = \sum_m \sum_n \left(\langle G^m G^n \rangle - \langle G^m \rangle \langle G^n \rangle \right) \delta(r - |\mathbf{r}_m - \mathbf{r}_n|), \tag{2.8}$$

where $\mathbf{r}_n$ is the coordinate for the center of a box used to calculate the elastic moduli. We used 3000 particle systems to calculate $g_{GG}(r)$ and checked that the calculation was consistent with results for 48000 particle systems. It is important to recognize the fact that the boxes used in this calculation may overlap (in order to get results for distances r smaller than the box size). Thus, boxes may share some of the same particles and their elastic moduli are necessarily correlated. Therefore, there are trivial correlations in $g_{GG}(r)$ due to overlapping boxes. We show $g_{GG}(r)$ for our most stable glass, $T_p = 0.062$, for four different box sizes w. We find that $g_{GG}(r)$ decays to

near zero at the size of the box, which is indicated by the vertical lines in the figure. This implies that only the trivial correlations exists.

To explore further if there are spatial correlations for the shear modulus and the bulk modulus at every temperature and every box size, we calculate the cross correlations of neighboring non-overlapping boxes. To this end we calculate the correlation parameter

$$\Psi_{\Gamma}^{m,n} = \left\langle \left(\frac{\Gamma^m - \Gamma}{\sigma_{\Gamma^m}} \right) \left(\frac{\Gamma^n - \Gamma}{\sigma_{\Gamma^n}} \right) \right\rangle_m \tag{2.9}$$

where, $\langle \cdots \rangle_m$ denotes an average over all the boxes and box n is one of the six nearest neighbors of box m and $\Gamma = G$ or K. A correlation parameter close to 0 indicates no significant correlation and a value of 1 indicates perfect correlation. In Fig. 2.6(b) we show Ψ_G (circles) and Ψ_K (squares) for box sizes of $w = 6.075$ (black), 4.542 (red), and 3.028 (blue). The values of Ψ_Γ are all close to zero and there are no noticeable trends with box size or parent temperature. This leads us to conclude that the elastic moduli, calculated using this fully local approach, do not exhibit any spatial correlations. We also examined correlations of G_n^m where $n = 1...5$ found in Equation 2.7 and found the same trends, i.e. only trivial correlations. We note that there are other methods to calculate local elastic moduli[79], and these other methods may indicate that the moduli are spatially correlated.

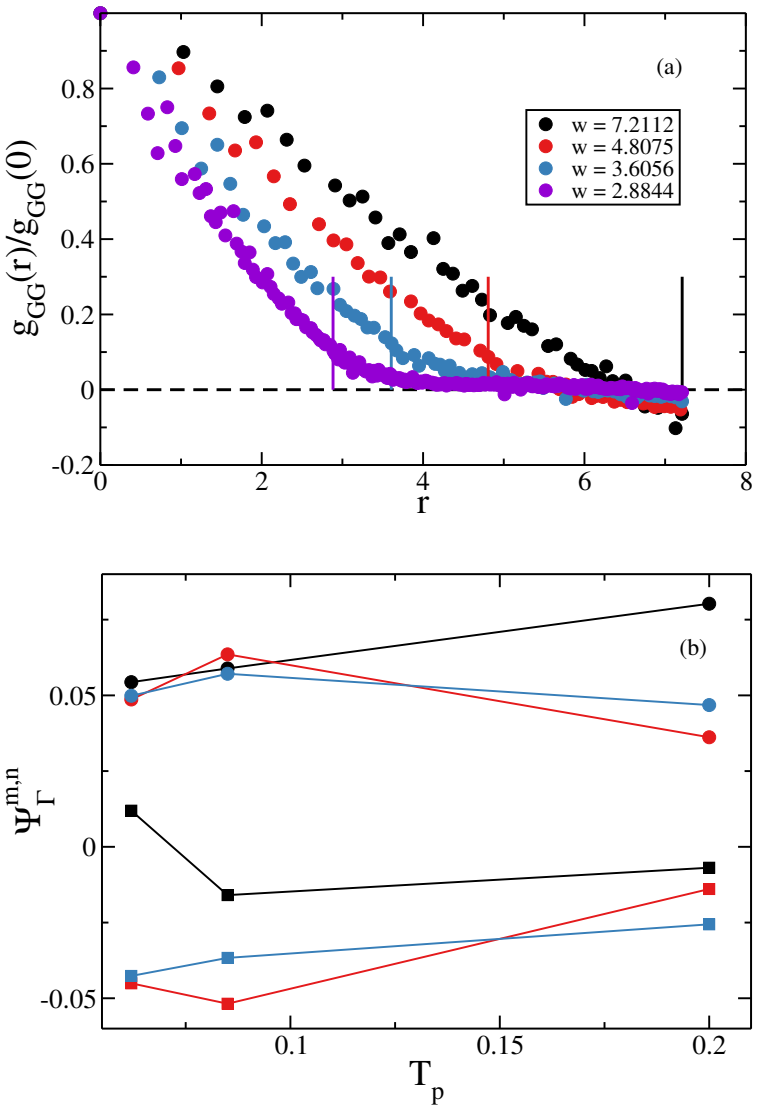

Figure 2.6: Panel (a) shows the spatial correlations of the shear modulus G for a 3000 particle system and for our most stable glass, $T_p = 0.062$. The vertical lines indicate the box sizes. At these points the trivial correlations disappear. Panel (b) illustrates the correlation parameter $\Psi_G^{m,n}$ (circles) and $\Psi_K^{m,n}$ (squares) for the box sizes $w = 6.075$ (black), 4.542 (red), and 3.028 (blue) as a function of parent temperature ($N = 48000$). The correlation parameter is small and there is no clear box size or parent temperature dependence.

This conclusion is at odds with the result of Gelin *et al.*[100] who reported that the elastic correlations decayed as r^{-2} for a two dimensional glass-forming system different from the system used here. We note that Gelin *et al.* used a different way to define local elastic moduli. However, Mizuno and Ikeda[105] utilized the same method as Gelin *et al.* for yet another, different two dimensional system and found that the stress correlations decay as r^{-2}, but the elastic moduli cor-

relations does not show the same long range correlations. We note that power-law decay of spatial correlations of the coarse-grained stress field is generally expected to follow $1/r^d$, where d denotes the spatial dimension[116].

2.5 Conclusions

We examined the structural heterogeneities, including local and global elastic moduli, of glassy systems prepared from parent systems equilibrated at different initial temperatures. Our calculations showed that the glass has a rather mild 27% increase of the local shear modulus, and a smaller 7% decrease on local bulk modulus compared to their values at the mode-coupling temperature with decreasing parent temperature. More importantly, we found that the local shear and the local bulk moduli become more uniform with decreasing parent temperature and thus stability of the glass. This finding is consistent with the recent report on the stability and sound attenuation of stable glasses[34]. Sound attenuation increases with an increase in the fluctuations of the local elasticity, and hence with a decrease of the stability. Our results are in qualitative agreement with fluctuating elasticity theory[74,76,80], which predicts an increase of sound attenuation and the observed Rayleigh-like k^4 scaling for small wavevectors[34,105].

Our results are also qualitatively consistent with recent experimental work by Pogna *et al.* on hyperaged amber[104], which showed that the elastic matrix becomes more homogeneous with increased stability, corresponding to a smaller $T_{\rm p}$ and a narrower moduli distribution in our study. However, we find that the local moduli are not spatially correlated. Pogna *et al.* inferred a 22% increase in the length scale characterizing elastic correlations. The same work reported on an increase of the elastic moduli fluctuation length scale in the more stable amorphous medium. This result, however, remains at variance with the findings of our study, where there is no discernible length scale associated with elasticity and there is no long range decay of elastic correlations. The lack of long range decay is also at odds with the study of Gelin *et al.*[100], but agrees with the conclusions of Mizuno and Ikeda[105].

Our results suggest that the current version of fluctuating elasticity theory is not a quantitatively accurate description of sound attenuation and the boson peak in amorphous solids, even though it makes qualitatively accurate predictions. A similar conclusion was drawn by Caroli and Lamaître[17], who developed a full tensorial fluctuating elasticity theory and found that it underestimates the sound attenuation by about two orders of magnitude. Further theoretical work is warranted to properly describe the interplay of sound attenuation and elastic heterogeneities. Additionally, Mizuno and Ikeda found that elastic moduli correlations may be system dependent[105]. Therefore, different systems should be examined to establish the universality of the results reported here and in other papers. In particular, we note that the polydisperse system studied here is designed to suppress crystallization, and hence some fluctuations may be suppressed compared to more standard binary mixtures.

2.6 Funding

A.S., E. F., and G.S. acknowledge funding from NSF DMR-1608086.

Chapter 3

The Einstein effective temperature can predict the tagged active particle density.[†]

3.1 Overview

We derive a distribution function for the position of a tagged active particle in a slowly varying in space external potential, in a system of interacting active particles. The tagged particle distribution has the form of the Boltzmann distribution but with an effective temperature that replaces the temperature of the heat bath. We show that the effective temperature that enters the tagged particle distribution is the same as the effective temperature defined through the Einstein relation, *i.e.* it is equal to the ratio of the self-diffusion and tagged particle mobility coefficients. This result shows that this effective temperature, which is defined through a fluctuation-dissipation ratio, is relevant beyond the linear response regime. We verify our theoretical findings through computer simulations. Our theory fails when an additional large length scale appears in our active system. In the system we simulated, this length scale is associated with long-wavelength density fluctuations that emerge upon approaching motility-induced phase separation.

3.2 Introduction

Equilibrium statistical mechanics provides us with explicit expressions for many-particle probability distributions for systems that are either isolated or in contact with one or more reservoirs[117]. Probably the most often invoked distribution is the Boltzmann distribution $\propto \exp\left(-\mathcal{H}/T\right)$ describing an equilibrium system with Hamiltonian $\mathcal{H}$ at a temperature T (here and in the following we use units such that the Boltzmann constant is equal to 1, $k_B = 1$). A lot of effort, analytical

[†]This chapter was previously published and is reproduced here with minor modifications. See: A. Shakerpoor, E. Flenner, and G. Szamel, The Einstein effective temperature can predict the tagged active particle density, *J. Chem. Phys.* **2021**, *154*, 081100.

and/or numerical, is required to obtain from this distribution explicit results for measurable properties of a system of interacting particles, but at least we are provided with an explicit starting point for such an effort.

In contrast, for out-of-equilibrium stationary states we do not have such a starting point. If we were to follow the same route as in equilibrium statistical mechanics, we would need to derive an exact or approximate expression for a non-equilibrium steady-state many-particle distribution and then use it to calculate measurable properties of the non-equilibrium system considered. It is rather unlikely that a general formula for such a distribution exists. Conversely, it is very likely that if it were to be found it would be more complicated than the many-particle equilibrium distribution.

On the other hand, it is not clear that we need the full many-particle distribution. Most of the interesting properties of many-particle systems can be expressed in terms of reduced distribution functions, *i.e.* pair distribution $g(r)$ and its generalizations to groups of more than two particles. To calculate these properties one can attempt to derive approximate formulas for the reduced distribution for specific non-equilibrium steady states. We note that in some cases the reduced distributions in non-equilibrium steady states can be measured directly. For example, in the iconic scattering experiment of Clark and Ackerson[118] the static structure factor, *i.e.* the Fourier transform of the pair distribution function, of a sheared colloidal suspension was measured. This experiment inspired a number of other experimental, computational, and theoretical studies of the pair structure in colloidal systems under shear.

In the present paper we focus on a class of non-equilibrium systems that have attracted a lot of attention in the last decade, active matter systems[40,42,45,47,48,70,119]. The constituents of these systems consume energy and as a result move in a systematic way. Examples include assemblies of bacteria or of cells, suspensions of Janus colloidal particles, swarms of insects and flocks of birds. These constituents are often modeled as active or self-propelled particles, which move in a systematic way on short-time scales and in a diffusive way on long-time scales. Importantly, their dynamics breaks detailed balance, and thus their stationary states are profoundly different from equilibrium states. Needless to say, many-particle probability distributions describing these stationary states

are not known explicitly. Several different approximate expressions for such distributions have been proposed and tested[120–122]. In spite of a considerable body of work it is not yet clear which approximate method is the most promising.

In some limits the problem of finding the many-particle stationary distribution for systems of interacting active particles may simplify. For example, in a recent remarkable contribution de Pirey *et al.*[123] showed that in the large dimensional limit, higher-than-two-particle correlations are negligible and used this finding to derive an exact expression for the pair distribution function.

Here we are interested in a more restricted problem. We consider a system of interacting active particles in the presence of an external potential that varies slowly in space and acts on one particle only, the tagged particle. The question we want to answer is, what is the spatial distribution of tagged particle's position? For an equilibrium system at constant temperature this problem has a simple answer; the tagged particle distribution is the Boltzmann distribution for a single particle in an external potential at the temperature of the system. Remarkably, this answer is valid irrespectively of the spatial dependence of the external potential.

We show that for a system of interacting active particles in the limit of a slowly varying in space external potential the tagged particle distribution also has a form of the Boltzmann distribution. However, in this case the role of the temperature is played by a variable that is a ratio of two quantities for which we derive exact albeit formal expressions. Importantly, we show that these quantities are two well-known parameters describing tagged particle dynamics, the self-diffusion coefficient and the tagged particle mobility. Thus, the role of the temperature in our tagged particle distribution is played by the ratio of the self-diffusion and mobility coefficients, which has long been recognized as one of the so-called effective temperatures[124], the Einstein relation temperature.

Recall that in equilibrium statistical mechanics the temperature appears not only in equilibrium probability distributions but also in other relations[125]. In particular, it appears as a proportionality constant in fluctuation-dissipation relations, which connect fluctuations in equilibrium and linear response functions due to weak external perturbations[117,126,127]. The derivation of these relations relies upon the equilibrium form of the many-particle distribution, and in out-of-equilibrium sys-

tems these relations are generally not valid. In the nineties Cugliandolo, Kurchan and Peliti[128] realized that the violation of fluctuation-dissipation relations can be used to define temperature-like quantities, which they called effective temperatures. These temperatures are defined through the fluctuation-dissipation ratios, *i.e.* the ratios of the properties characterizing fluctuations and linear response/dissipation in non-equilibrium states. Importantly, Cugliandolo, Kurchan and Peliti showed that in a slowly relaxing model system, the effective temperature determines the direction of the heat flow. Following this work, a number of different effective temperatures and their properties have been investigated in globally driven non-equilibrium stationary states[129,130] and non-stationary aging systems[131,132]. Remarkably, in driven glassy systems it was found that several seemingly different temperatures had the same value[129], which hinted that there might be a unique effective temperature, at least in this case.

More recently, the Einstein effective temperature, which is defined as the ratio of the self-diffusion and tagged particle mobility coefficients, has been used to characterize some properties of active matter systems[133–136]. In particular, some of us argued that the difference between the Einstein temperature and the so-called active temperature, which characterizes the strength of the self-propulsions, is a good measure of the departure of an active system from equilibrium[137].

Since effective temperatures are defined through the ratio of fluctuations in a steady state to a function describing linear response of this state to a weak external perturbation, it is not clear whether these temperatures can also describe any non-linear response of steady states. Two studies showed the usefulness of the Einstein effective temperature for non-linear response. First, Hayashi and Sasa[138] showed that the Einstein temperature determines the large scale distribution of a single Brownian particle moving in a tilted periodic potential. Second, Szamel and Zhang[139] showed that the Einstein temperature determines the tagged particle density distribution in a slowly varying in space external potential in a system of interacting Brownian particles under steady shear. In both cases the important assumption was the slow variation in space of the external potential, but there was no restriction on its strength.

The present result is similar to that of Ref. [139] in that we assume that the external potential acting on the tagged particle is slowly varying in space and we show that the density distribution is determined by the Einstein temperature. The important difference with this earlier work is in that the present system is athermal, locally driven by self-propulsions of individual particles, and isotropic.

We verify our theoretical results by performing computer simulations of an active system with an external potential. We show that the theory is valid as long as the spatial scale on which the tagged particle density distribution varies is the longest relevant length scale in the problem. When the density correlation length becomes large, due to the incipient motility-induced phase separation, the assumption behind our theory becomes invalid and numerical results show that the theory fails.

The paper is organized as follows. In Sec. 4.3 we present our theoretical derivation. In Sec. 3.4, we describe our computer simulation model and describe our numerical procedures in Sec. 4.4.1, and then we present the results and discuss the limitations of our theory in Sec. 4.4.2. Finally, we conclude the paper with an overview of our results in Sec. 3.5.

3.3 Theoretical Derivation

To derive the equation describing the tagged active particle density distribution in a slowly varying in space external potential we use a gradient expansion. Specifically, we use a version of the celebrated Chapman-Enskog expansion that was originally introduced to derive hydrodynamic equations and the expressions for transport coefficients from the Boltzmann kinetic equation[140]. The specific implementation of the Chapman-Enskog procedure that we use is inspired by Titulaer's[141] derivation of the generalized Smoluchowski equation from the Fokker-Planck equation. Here we follow the nomenclature used by Titulaer (and also adopted in the classic review article of Hess and Klein[142]) and use the name Smoluchowski description/equation to refer to the description of dynamics of colloidal particles on the time scale much larger than the velocity relaxation time, using as dynamic variables only the positions of the particles. In contrast, we use the name Fokker-

Planck description/equation to refer to the description of the dynamics of colloidal particles on a much shorter time scale, on which particles' velocities are relevant. The Fokker-Planck description uses as dynamic variables both positions and velocities of the particles. Thus, Titulaer's derivation amounts to an elimination of the particle's velocity or, in other words, a contracted description of the particle's dynamics, which is possible on the longer time scale. Our present derivation is also a contracted description of the tagged particle distribution, which is possible if the external potential is slowly varying in space. It is similar to the derivation used earlier[139] to obtain an equation describing the tagged particle distribution in a sheared colloidal suspension.

To make the derivation concrete we need to specify the active particle model. We consider a system of active Ornstein-Uhlenbeck particles (AOUPs)[83,120,143]. These particles move in a viscous medium, without inertia (*i.e.* with overdamped dynamics), under the combined influence of the inter-particle forces and self-propulsions, with the latter evolving according to the Ornstein-Uhlenbeck stochastic process. The equations of motions read

$$\dot{\mathbf{r}}_i = \mu_0 \left[\mathbf{F}_i + \mathbf{f}_i\right], \tag{3.1}$$

$$\tau_p \dot{\mathbf{f}}_i = -\mathbf{f}_i + \boldsymbol{\eta}_i. \tag{3.2}$$

In Eq. (3.1) $\mathbf{r}_i$ is the position of particle i, μ_0 is the mobility coefficient of an isolated particle, which is the inverse of the isolated particle's friction coefficient, $\mu_0 = \xi_0^{-1}$, $\mathbf{F}_i$ is the force acting on particle i due to all other particles,

$$\mathbf{F}_i = \sum_{j \neq i} \mathbf{F}(\mathbf{r}_{ij}), \tag{3.3}$$

where $\mathbf{r}_{ij} = \mathbf{r}_i - \mathbf{r}_j$ and $\mathbf{F}(\mathbf{r}) = -\partial_{\mathbf{r}} V(r)$ with $V(r)$ being the two-body potential, and $\mathbf{f}_i$ is the self-propulsion. In Eq. (3.2) τ_p is the persistence time of the self-propulsion and $\boldsymbol{\eta}_i$ is the internal Gaussian noise with zero mean and variance $\langle \boldsymbol{\eta}_i(t)\boldsymbol{\eta}_j(t')\rangle_{\text{noise}} = 2\xi_0 k_B T_a \mathbf{I}\delta_{ij}\delta(t-t')$, where $\langle \ldots \rangle_{\text{noise}}$ denotes averaging over the noise distribution, T_a is the "active" temperature, and $\mathbf{I}$ is the

unit tensor. The active temperature characterizes the strength of the self-propulsion. In addition, it determines the long-time diffusion coefficient of an isolated AOUP, $D_0 = T_a\mu_0 \equiv T_a/\xi_0$.

We assume that there is a slowly varying in space external potential, $\Phi(\mathbf{r}_1)$, acting on particle 1. This particle will be referred to as the tagged particle. The external potential results in an additional term, $-\partial_{\mathbf{r}_1}\Phi(\mathbf{r}_1)$, in the equation of motion for the tagged particle,

$$\dot{\mathbf{r}}_1 = \mu_0 \left[\mathbf{F}_1 - \partial_{\mathbf{r}_1}\Phi(\mathbf{r}_1) + \mathbf{f}_1\right], \tag{3.4}$$

$$\tau_p\dot{\mathbf{f}}_1 = -\mathbf{f}_1 + \boldsymbol{\eta}_1. \tag{3.5}$$

We assume that the systems described by equations of motion (3.1-3.4) can reach a stationary state. The N-particle stationary state distribution of positions and self-propulsions, $P_{\rm s}^{\Phi}$, satisfies the following equation,

$$\left[\Omega_s + \partial_{\mathbf{r}_1}\cdot\mu_0\left(\partial_{\mathbf{r}_1}\Phi(\mathbf{r}_1)\right)\right] P_{\rm s}^{\Phi}\left(\mathbf{r}_1,\mathbf{f}_1,\ldots,\mathbf{r}_N,\mathbf{f}_N\right) = 0. \tag{3.6}$$

Here Ω_s is the evolution operator that corresponds to the unperturbed equations of motion,

$$\Omega_{\rm s}\left(\mathbf{r}_1,\mathbf{f}_1,\ldots,\mathbf{r}_N,\mathbf{f}_N\right) = -\mu_0\sum_{i=1}^{N}\partial_{\mathbf{r}_i}\cdot\left(\mathbf{F}_i+\mathbf{f}_i\right) + \sum_{i=1}^{N}\partial_{\mathbf{f}_i}\cdot\left(\frac{1}{\tau_p}\mathbf{f}_i + \frac{T_{\rm a}}{\mu_0\tau_p^2}\partial_{\mathbf{f}_i}\right). \tag{3.7}$$

To make it an explicit assumption that the external potential acting on the tagged particle is slowly varying we write it as $\Phi(\epsilon\mathbf{r}_1)$, where ϵ is a small parameter. As described before[139], we will use ϵ as an expansion parameter and then, at the end of the derivation, we will set it to 1.

Our goal is to derive from Eq. (3.6) a closed equation for the stationary tagged particle density distribution, $n_s(\mathbf{r}_1)$,

$$n_s(\mathbf{r}_1) = \int d\mathbf{f}_1 d\mathbf{r}_2\ldots d\mathbf{f}_N d\mathbf{r}_N P_{\rm s}^{\Phi}\left(\mathbf{r}_1,\mathbf{f}_1,\ldots,\mathbf{r}_N,\mathbf{f}_N\right). \tag{3.8}$$

The tagged particle density is non-uniform due to the external potential Φ. Due to the slow variation of the external potential, we assume that the tagged particle density will also be slowly varying. Again, to make this assumption explicit we write the tagged particle density as $n_s(\epsilon \mathbf{r}_1)$.

Due to the inter-particle interactions the N-particle distribution is not a slowly varying function of the tagged particle position if the positions of all other particles are kept constant. However, it should be a slowly varying function of $\mathbf{r}_1$ if it is written in terms of the tagged particle position and the positions of all other particles *relative* to the tagged particle position, *i.e.* in terms of $\mathbf{r}_1$ and $\mathbf{r}_{21}$, $\mathbf{r}_{31}$ *etc.* To make this assumption explicit we change the variables and write the stationary state equation in terms of $\mathbf{R}_1 = \epsilon \mathbf{r}_1$, $\mathbf{R}_2 = \mathbf{r}_{21}, \ldots, \mathbf{R}_N = \mathbf{r}_{N1}$,

$$\left[\Omega_s^{(0)} + \epsilon \Omega_s^{(1)} + \epsilon^2 \partial_{\mathbf{R}_1} \cdot \mu_0 \left(\partial_{\mathbf{R}_1} \Phi(\mathbf{R}_1)\right)\right] P_{\mathrm{s}}^{\Phi} \left(\mathbf{R}_1, \mathbf{f}_1, \ldots, \mathbf{R}_N, \mathbf{f}_N\right) = 0, \tag{3.9}$$

where we separate contributions to the evolution operator of different orders in ϵ,

$$\Omega^{(0)} = -\mu_0 \left[-\sum_{i=2}^{N} \partial_{\mathbf{R}_i} \cdot \left(\sum_{i \neq j = 2}^{N} \mathbf{F}\left(-\mathbf{R}_j\right) + \mathbf{f}_1 \right) + \sum_{i=2}^{N} \partial_{\mathbf{R}_i} \cdot \left(\sum_{i \neq j = 2}^{N} \mathbf{F}\left(\mathbf{R}_i\right) + \mathbf{f}_i \right) \right] + \sum_{i=1}^{N} \partial_{\mathbf{f}_i} \cdot \left(\frac{1}{\tau_p} \mathbf{f}_i + \frac{T_{\mathrm{a}}}{\mu_0 \tau_p^2} \partial_{\mathbf{f}_i} \right), \tag{3.10}$$

$$\Omega^{(1)} = -\mu_0 \partial_{\mathbf{R}_1} \cdot \left(\sum_{i=2}^{N} \mathbf{F}\left(-\mathbf{R}_i\right) + \mathbf{f}_1 \right) - \sum_{i=2}^{N} \partial_{\mathbf{R}_i} \cdot \mu_0 \left(\partial_{\mathbf{R}_1} \Phi\left(\mathbf{R}_1\right)\right). \tag{3.11}$$

Following Refs. [141] and [139], we now look for a special perturbative solution of Eq. (3.9)

$$P_{\mathrm{s}}^{\Phi} \left(\mathbf{R}_1, \mathbf{f}_1, \ldots, \mathbf{R}_N, \mathbf{f}_N\right) = n_{\mathrm{s}} \left(\mathbf{R}_1\right) P_{\mathrm{s}}^{(0)} \left(\mathbf{f}_1, \mathbf{R}_2, \mathbf{f}_2, \ldots, \mathbf{R}_N, \mathbf{f}_N\right) + \epsilon P_{\mathrm{s}}^{(1)} \left(\mathbf{R}_1, \mathbf{f}_1, \mathbf{R}_2, \mathbf{f}_2, \ldots, \mathbf{R}_N, \mathbf{f}_N\right) + \epsilon^2 P_{\mathrm{s}}^{(2)} \left(\mathbf{R}_1, \mathbf{f}_1, \mathbf{R}_2, \mathbf{f}_2, \ldots, \mathbf{R}_N, \mathbf{f}_N\right) + \ldots. \tag{3.12}$$

We use the solution postulated in Eq. (3.12) to derive perturbatively an equation for the tagged particle density distribution,

$$\left(\mathcal{D}^{(0)} + \epsilon\mathcal{D}^{(1)} + \epsilon^2\mathcal{D}^{(2)} + \ldots\right) n_{\mathrm{s}}\left(\mathbf{R}_1\right) = 0. \tag{3.13}$$

Eq. (3.13) is obtained by the integration of Eq. (3.9) over the self-propulsion of the tagged particle and the positions of all particles other than the tagged particle. For example, the first two terms in Eq. (3.13) read

$$\mathcal{D}^{(0)} n_{\mathrm{s}}\left(\mathbf{R}_1\right) = \int d\mathbf{f}_1 d\mathbf{R}_2 d\mathbf{f}_2 \ldots d\mathbf{R}_N d\mathbf{f}_N \Omega^{(0)} n_{\mathrm{s}}\left(\mathbf{R}_1\right) P_{\mathrm{s}}^{(0)}, \tag{3.14}$$

$$\mathcal{D}^{(1)} n_{\mathrm{s}}\left(\mathbf{R}_1\right) = \int d\mathbf{f}_1 d\mathbf{R}_2 d\mathbf{f}_2 \ldots d\mathbf{R}_N d\mathbf{f}_N \Omega^{(1)} n_{\mathrm{s}}\left(\mathbf{R}_1\right) P_{\mathrm{s}}^{(0)}$$
$$+ \int d\mathbf{f}_1 d\mathbf{R}_2 d\mathbf{f}_2 \ldots d\mathbf{R}_N d\mathbf{f}_N \, \Omega^{(0)} P_{\mathrm{s}}^{(1)}. \tag{3.15}$$

We note that the second term in Eq. (3.15) vanishes due to integration by parts.

Following the standard Chapman-Enskog procedure[140,141], the tagged particle density $n_{\mathrm{s}}\left(\mathbf{R}_1\right)$ is not expanded in ϵ. Moreover, as in the standard Chapman-Enskog procedure[140,141], there is some freedom in choosing higher order functions $P_{\mathrm{s}}^{(i)}$, $i \geq 1$. This freedom is eliminated by imposing the usual conditions,

$$\int d\mathbf{f}_1 d\mathbf{R}_2 d\mathbf{f}_2 \ldots d\mathbf{R}_N d\mathbf{f}_N P_{\mathrm{s}}^{(i)} = 0 \qquad \forall \; i \geq 1. \tag{3.16}$$

Conditions (3.16) imply that the tagged particle density is completely determined by the zeroth order term in expansion (3.9).

To find the special solution for the stationary state probability distribution we substitute Eq. (3.12) into Eq. (3.9) and solve order by order. The terms of zeroth order give

$$\Omega^{(0)} P_{\mathrm{s}}^{(0)}\left(\mathbf{f}_1, \mathbf{R}_2, \mathbf{f}_2, \ldots, \mathbf{R}_N, \mathbf{f}_N\right) = 0. \tag{3.17}$$

Thus, $P_{\rm s}^{(0)}$ is the translationally invariant steady state distribution of the positions and self-propulsions in the absence of the external potential. The combination of expansion (3.12) and conditions (3.16) implies that this distribution should be normalized to 1,

$$\int d\mathbf{f}_1 d\mathbf{R}_2 d\mathbf{f}_2 \dots d\mathbf{R}_N d\mathbf{f}_N P_{\rm s}^{(0)} = 1. \tag{3.18}$$

The first order terms give an equation for $P_{\rm s}^{(1)}$ in which $n_{\rm s} P_{\rm s}^{(0)}$ plays the role of a source term,

$$\Omega^{(0)} P_{\rm s}^{(1)} + \Omega^{(1)} n_{\rm s}\left(\mathbf{R}_1\right) P_{\rm s}^{(0)} = 0. \tag{3.19}$$

We can formally solve Eq. (3.19) for $P_{\rm s}^{(1)}$,

$$P_{\rm s}^{(1)} = -\left[\Omega^{(0)}\right]^{-1} \Omega^{(1)} n_{\rm s}\left(\mathbf{R}_1\right) P_{\rm s}^{(0)}. \tag{3.20}$$

We recall that $P_{\rm s}^{(0)}$ does not depend on $\mathbf{R}_1$ and we get

$$\begin{aligned} P_{\rm s}^{(1)} = \mu_0 \left[\Omega^{(0)}\right]^{-1} \left[\sum_{i=2}^{N} \mathbf{F}\left(-\mathbf{R}_i\right) + \mathbf{f}_1\right] P_{\rm s}^{(0)} \cdot \partial_{\mathbf{R}_1} n_{\rm s}\left(\mathbf{R}_1\right) \\ + \mu_0 \left[\Omega^{(0)}\right]^{-1} \left(\sum_{i=2}^{N} \partial_{\mathbf{R}_i}\right) P_{\rm s}^{(0)} \cdot \left(\partial_{\mathbf{R}_1} \Phi\left(\mathbf{R}_1\right)\right) n_{\rm s}\left(\mathbf{R}_1\right). \end{aligned} \tag{3.21}$$

We then use these results to derive successive terms in the stationary state equation for the tagged particle distribution, Eq. (3.13). We note that $\mathcal{D}^{(0)}$, Eq. (3.14), involves $\Omega^{(0)} P_{\rm s}^{(0)}$, and thus it vanishes. Then, we note that $\mathcal{D}^{(1)}$, Eq. (3.15), consists of two terms and, as we stated earlier, that the second term vanishes due to integration by parts. In turn, the first term, involving $\Omega^{(1)}$, consists of two contributions that originate from the two contributions to $\Omega^{(1)}$, Eq. (3.11). The first one is proportional to the following integral,

$$\mu_0 \int d\mathbf{f}_1 d\mathbf{R}_2 d\mathbf{f}_2 \dots d\mathbf{R}_N d\mathbf{f}_N \left(\sum_{i=2}^{N} \mathbf{F}\left(-\mathbf{R}_i\right) + \mathbf{f}_1\right) P_{\rm s}^{(0)}, \tag{3.22}$$

which involves the sum of the total inter-particle force acting on that tagged particle and of the self-propulsion of the tagged particle. We note that integral (3.22) is equal to the tagged particle current in the unperturbed stationary state. We assume that there are no average stationary currents in the stationary state, and thus integral (3.22) vanishes. The term contributing to $\mathcal{D}^{(1)}$ that originates from the second contribution to $\Omega^{(1)}$, Eq. (3.11), vanishes due to integration by parts.

The lowest order non-vanishing contribution to stationary state equation (3.13) originates from $\mathcal{D}^{(2)}$,

$$\mathcal{D}^{(2)} n_{\mathrm{s}}\left(\mathbf{R}_1\right) = \int d\mathbf{f}_1 d\mathbf{R}_2 d\mathbf{f}_2 \ldots d\mathbf{R}_N d\mathbf{f}_N \partial_{\mathbf{R}_1} \cdot \mu_0 \partial_{\mathbf{R}_1} \Phi(\mathbf{R}_1) n_{\mathrm{s}}\left(\mathbf{R}_1\right) P_{\mathrm{s}}^{(0)} + \int d\mathbf{f}_1 d\mathbf{R}_2 d\mathbf{f}_2 \ldots d\mathbf{R}_N d\mathbf{f}_N \Omega^{(1)} P_{\mathrm{s}}^{(1)} + \int d\mathbf{f}_1 d\mathbf{R}_2 d\mathbf{f}_2 \ldots d\mathbf{R}_N d\mathbf{f}_N \, \Omega^{(0)} P_{\mathrm{s}}^{(2)}. \quad (3.23)$$

The first term on the right-hand-side gives $\partial_{\mathbf{R}_1} \cdot \mu_0 \partial_{\mathbf{R}_1} \Phi(\mathbf{R}_1) n_{\mathrm{s}}\left(\mathbf{R}_1\right)$ and the last term vanishes after integration by parts. The second term is a sum of two contributions that originate from the two contributions to $\Omega^{(1)}$, Eq. (3.11). The second one vanishes after integration by parts and the first one can be re-written as

$$\partial_{\mathbf{R}_1} D \cdot \partial_{\mathbf{R}_1} n_{\mathrm{s}}\left(\mathbf{R}_1\right) + \partial_{\mathbf{R}_1} \bar{\mu} \cdot \left(\partial_{\mathbf{R}_1} \Phi\left(\mathbf{R}_1\right)\right) n_{\mathrm{s}}\left(\mathbf{R}_1\right), \quad (3.24)$$

where

$$D = -\frac{\mu_0^2}{d} \int d\mathbf{f}_1 d\mathbf{R}_2 d\mathbf{f}_2 \ldots d\mathbf{R}_N d\mathbf{f}_N \left(\sum_{i=2}^{N} \mathbf{F}\left(-\mathbf{R}_i\right) + \mathbf{f}_1 \right) \left[\Omega^{(0)}\right]^{-1} \left[\sum_{i=2}^{N} \mathbf{F}\left(-\mathbf{R}_i\right) + \mathbf{f}_1 \right] P_{\mathrm{s}}^{(0)}, \quad (3.25)$$

$$\bar{\mu} = -\frac{\mu_0^2}{d} \int d\mathbf{f}_1 d\mathbf{R}_2 d\mathbf{f}_2 \ldots d\mathbf{R}_N d\mathbf{f}_N \left(\sum_{i=2}^{N} \mathbf{F}\left(-\mathbf{R}_i\right) + \mathbf{f}_1 \right) \left[\Omega^{(0)}\right]^{-1} \left(\sum_{i=2}^{N} \partial_{\mathbf{R}_i} \right) P_{\mathrm{s}}^{(0)}. \quad (3.26)$$

We note that while writing Eqs. (3.25-3.26) we used the rotational invariance of the d-dimensional stationary state without the external potential.

Combining all non-vanishing contributions to $\mathcal{D}^{(2)}$, setting $\epsilon = 1$, and re-writing the resulting stationary state equation in terms of the original coordinate $\mathbf{r}_1$ we get the following equation for the tagged particle distribution,

$$\partial_{\mathbf{r}_1} \cdot \left[D\partial_{\mathbf{r}_1} + \mu \left(\partial_{\mathbf{r}_1} \Phi \left(\mathbf{r}_1 \right) \right) \right] n_{\mathrm{s}} \left(\mathbf{r}_1 \right) = 0, \tag{3.27}$$

where, rewritten in terms of the original coordinates $\mathbf{r}_1, \ldots, \mathbf{r}_N$, D and μ read

$$D = -\frac{\mu_0^2}{d} \frac{1}{V} \int \mathrm{d}\mathbf{r}_1 \mathrm{d}\mathbf{f}_1 \ldots \mathrm{d}\mathbf{r}_N \mathrm{d}\mathbf{f}_N \left(\mathbf{F}_1 + \mathbf{f}_1 \right) \left[\Omega_{\mathrm{s}} \right]^{-1} \left(\mathbf{F}_1 + \mathbf{f}_1 \right) P_{\mathrm{s}}^{(0)} \left(\mathbf{r}_1, \mathbf{f}_1, \ldots, \mathbf{r}_N, \mathbf{f}_N \right), \tag{3.28}$$

$$\mu = \mu_0 - \frac{\mu_0^2}{d} \frac{1}{V} \int \mathrm{d}\mathbf{r}_1 \mathrm{d}\mathbf{f}_1 \ldots \mathrm{d}\mathbf{r}_N \mathrm{d}\mathbf{f}_N \left(\mathbf{F}_1 + \mathbf{f}_1 \right) \left[\Omega_{\mathrm{s}} \right]^{-1} \partial_{\mathbf{r}_1} P_{\mathrm{s}}^{(0)} \left(\mathbf{r}_1, \mathbf{f}_1, \ldots, \mathbf{r}_N, \mathbf{f}_N \right). \tag{3.29}$$

Eq. (3.27) implies that the tagged particle distribution has the Boltzmann form,

$$n_{\mathrm{s}} \left(\mathbf{r}_1 \right) \propto \exp \left(-\Phi \left(\mathbf{r}_1 \right) / T^{\mathrm{eff}} \right), \tag{3.30}$$

where the effective temperature is the ratio of D and μ,

$$T^{\mathrm{eff}} = D/\mu. \tag{3.31}$$

The final step in the derivation is to assign some physical interpretation to D and μ. This interpretation has already been hinted by our choice of the symbols we used for these quantities. First, we note that since $\mu_0 \left(\mathbf{F}_1 + \mathbf{f}_1 \right)$ is the tagged particle velocity, D can be formally interpreted as the integral of the velocity auto-correlation function,

$$D = d^{-1} \int_0^\infty \left\langle \dot{\mathbf{r}}_1(t) \cdot \dot{\mathbf{r}}_1(0) \right\rangle, \tag{3.32}$$

which in turn is the standard expression for the self-diffusion coefficient[117]. Second, we note that if, for a system initially in a stationary state, a weak spatially uniform external force $\mathbf{F}_1^{\mathrm{ext}}$ is applied to the tagged particle, the tagged particle will start moving. Initially, since the distribution of the

other particles around the tagged particle is isotropic, its velocity will be equal to $\mu_0 \mathbf{F}_1^{\text{ext}}$ but after some time the distribution of the other particles will become slightly anisotropic and they will be exerting an additional friction force on the tagged particle. It can be shown that due to the change of the probability distribution the long-time limit of the tagged particle velocity will be $(\mu_0 + \bar{\mu})\, \mathbf{F}_1^{\text{ext}}$. Thus, $\mu = \mu_0 + \bar{\mu}$, Eq. (3.29), is the tagged particle mobility coefficient.

To summarize, we showed in this section that for a slowly varying in space external potential acting on the tagged particle the tagged particle density has the Boltzmann form with the temperature determined by the ratio of the self-diffusion and mobility coefficients, *i.e.* the Einstein effective temperature.

We note that although the derivation was performed for the AOUPs model, it did not use any features of the Ornstein-Uhlenbeck dynamics of the self-propulsion and the same derivation could be carried out for the athermal Active Brownian particles model.

3.4 Numerical Verification

3.4.1 Methods

To test Eq. (3.30) for the probability distribution and Eq. (3.31) for the effective temperature, we performed a series of computer simulations of interacting AOUPs in an external potential Φ, evolving according to equations of motion (3.1-3.5), and a parallel series of computer simulations of unperturbed particles, evolving according to equations of motion (3.1-3.2). We used the finite range Weeks-Chandler-Andersen (WCA) purely repulsive pair potential $V^{\text{WCA}}(r) = 4\varepsilon \left[\left(\frac{\sigma}{r}\right)^{12} - \left(\frac{\sigma}{r}\right)^{6} \right] + \varepsilon$, for $r < r_c \equiv 2^{1/6}\sigma$ and zero otherwise (we note that ε, which appears in this paragraph only, is different from small parameter ϵ introduced and used in Sec. 4.3). We present the results in standard LJ units where ε is the unit of energy, σ is the unit of length, and $\sigma^2/(\mu_0 \varepsilon)$ is the unit of time. We simulated $N = 10^4$ particles at a number density of $\rho = 0.6751$. The corresponding packing fraction can be calculated in two ways, using either σ or potential cutoff r_c as the characteristic length associated with the potential: $\pi\rho\sigma^3/6 = 0.3535$ whereas

$\pi\rho r_c^3/6 = 0.4999$. We note that at low active temperatures the present system resembles a hard sphere system and the latter volume fraction is the proper measure of the excluded volume.

We simulated AOUP systems at two different active temperatures, $T_a = 0.01$ and $T_a = 1.0$ and a range of persistence times τ_p. The values of T_a were chosen to roughly represent two different dependencies of the self-diffusion coefficient on the persistence time, which we identified in an earlier investigation[137,144]. At the lower temperature we expected D either to increase with τ_p or to have a non-monotonic dependence on τ_p. In contrast, at the higher temperature we expected D to decrease with τ_p.

For simulations without the external potential we used a time step $dt = 0.001$ for $\tau_p \geq 0.02$ and $dt = 0.0002$ for $\tau_p = 0.002$. For the perturbed systems we used $dt = 0.001$ for $T_a = 0.01$ (at which $\tau_p \geq 0.02$) and $dt = 0.0001$ for $T_a = 1.0$.

Evaluation and analysis of the tagged particle distribution

To induce a slowly varying, non-uniform density distribution of the tagged particle we used a potential that is periodic over the simulation box length L, and varying along the x, y or z axis,

$$\Phi(\alpha) = \Phi_0 \sin(2\pi\alpha/L) \qquad \alpha = x, y, z. \tag{3.33}$$

Since for the $N = 10^4$ particle system L is much larger than the particle size, this potential is indeed slowly varying. However, we will see that if the parameter characterizing the strength of the potential, Φ_0, is large enough, the tagged particle density can vary on a smaller length scale.

Without the external potential, the tagged particle distribution is uniform and equal to $1/V$. We are primarily interested in the non-linear response regime, *i.e* we chose Φ_0 such that the tagged particle distribution is strongly non-uniform. Specifically, we chose $\Phi_0 = 0.1$ for $T_a = 0.01$ and $\Phi_0 = 1.0$ and 10.0 for $T_a = 1.0$.

To improve the statistics we applied the external potential to 1.0% of the particles for $T_a = 0.01$ and 0.2% of the particles for $T_a = 1.0$. We note that while selecting the percentage of particles to which the external potential is applied one has to make sure that these particles are dilute enough

in the whole system to be non-interacting. To check for this we calculated steady state structure factors for the particles on which the external potential acts in the plane perpendicular to the direction of the external force, and we confirmed that with these percentages the particles were dilute enough.

To further improve the statistics, we applied the external potential to different particles along each Cartesian coordinate within the same system. The distributions presented are averaged over all three Cartesian coordinates.

We evaluated tagged particle distributions due to external potential (3.33). We fitted Boltzmann distributions (3.30) to the numerical results treating the effective temperature as a fit parameter[145]. The resulting values are shown in the following as T^{fit}.

Evaluation of the Einstein temperature

The Einstein effective temperature is defined as the ratio of the self-diffusion and tagged particle mobility coefficients[146,147],

$$T^{\text{E}} = D/\mu. \tag{3.34}$$

To calculate the self-diffusion coefficient we simulate unperturbed systems of AOUPs described before and use the standard relation,

$$D = (2dN)^{-1} \lim_{t\to\infty} \frac{1}{t} \sum_i \left\langle (\mathbf{r}_i(t) - \mathbf{r}_i(0))^2 \right\rangle \tag{3.35}$$

where d is the dimensionality of the system.

To evaluate the tagged particle mobility coefficient for our out-of-equilibrium systems we use the approach presented in Ref. [134], which involves the application of Malliavin weights. We define the mobility coefficient in terms of a time-dependent response function $\chi(t)$[134],

$$\mu = \lim_{t\to\infty} \frac{1}{t} \chi(t). \tag{3.36}$$

In turn, the response function is calculated through averages involving weighting functions[134],

$$\chi(t) = (Nd)^{-1} \sum_{\alpha,i} \left[\langle \alpha_i(t) \left(q_{i\alpha}(t) - q_{i\alpha}(0) \right) \rangle + \tau_p \langle \dot{\alpha}_i(t) \left(q_{i\alpha}(t) - q_{i\alpha}(0) \right) \rangle \right], \tag{3.37}$$

where $\alpha = x, y, z$ and the weighting function $q_{i\alpha}(t)$ obeys the equation of motion,

$$\dot{q}_{i\alpha} = \mu_0^2 / \left(2T_{\rm a} \right)^{-1} \eta_{i\alpha}, \tag{3.38}$$

where $\eta_{i\alpha}$ is the α component of the Gaussian noise acting on particle i.

3.4.2 Results

For the external potential Φ varying along α axis, $\alpha = x, y, z$, the tagged particle distribution varies along the same direction and is uniform along the remaining two directions. In Fig. 3.1 we show tagged particle distributions averaged over the three directions of the perturbation. More precisely, we show $L^2 \bar{n}_s(\alpha)$ where $L = 24.56$ is the box size and the over-bar denotes averaging over three directions of the perturbation. We use the standard normalization condition $\int_V d\mathbf{r} \bar{n}_s(\mathbf{r}) = 1$. The distributions shown in Fig. 3.1 are significantly different from the tagged particle density in the absence of the external potential, when $L^2 V^{-1} = 1/L = 0.0407$.

The important qualitative information that can be obtained from a quick look at Fig. 3.1 is that the tagged particle densities depend strongly on the persistence time of the self-propulsion.

To further verify that we are in the non-linear response regime in Fig. 3.2, we show the tagged particle mean squared displacements (MSDs) along the axis of the external potential (solid curves) compared to the mean squared displacement along an axis perpendicular to that of the external potential (dashed curves, for clarity shown for the longest persistence time only). We see that the MSDs along the axis of the external potential are significantly different from those along a perpendicular axis. In fact, for $T_a = 0.01$ and $\Phi_0 = 0.1$ the tagged particle is localized at the external potential minimum on the time scale of the simulation.

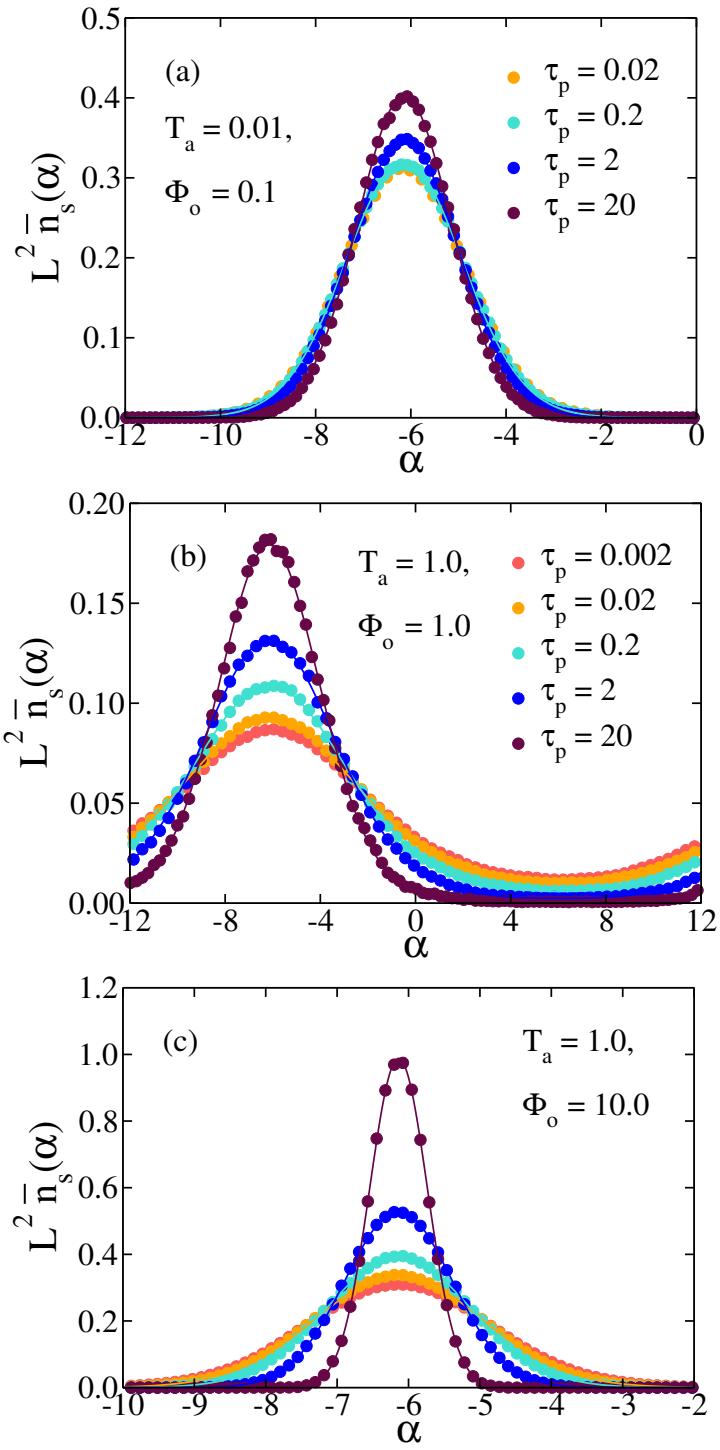

Figure 3.1: The tagged particle density distribution along the direction of the external potential, $L^2\bar{n}_s$, averaged over three different directions of the potential. α is the coordinate along the direction of the external potential. The box extends from $\alpha = -12.28$ to $\alpha = 12.28$. The minimum of the external potential is located at $\alpha = -6.14$ and for particles localized around the potential minimum, (a) and (c), we focus on the part of the box near the minimum. (a) $T_a = 0.01$, $\Phi_0 = 0.1$ and $\tau_p \in [0.02, 20]$. (b) $T_a = 1.0$, $\Phi_0 = 1.0$ and $\tau_p \in [0.002, 20]$. (c) $T_a = 1.0$, $\Phi_0 = 1.0$ and $\tau_p \in [0.002, 20]$. Solid lines indicate Boltzmann distributions fitted to the data. The unperturbed distribution would be $L^2 \times V^{-1} = L^{-1} = 0.0407$.

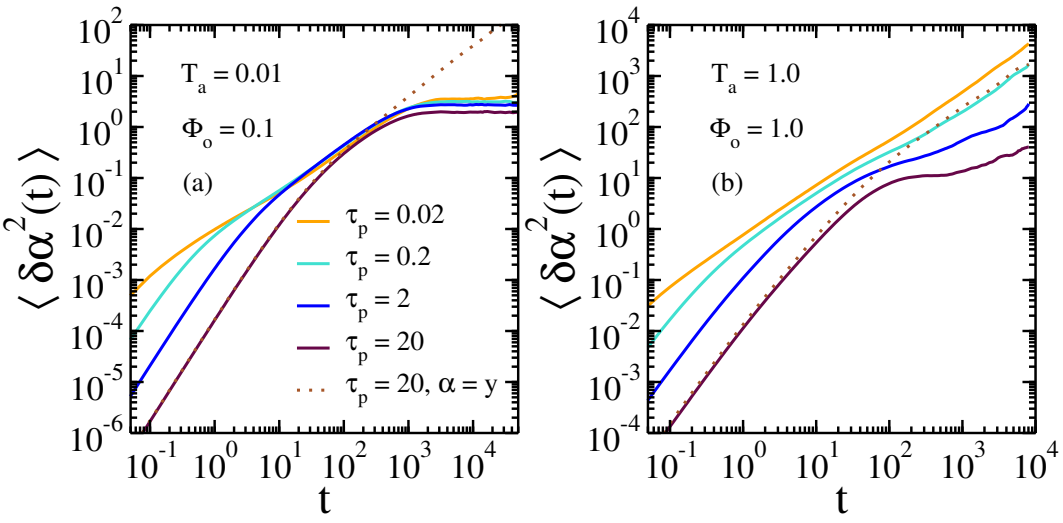

Figure 3.2: Tagged particle mean squared displacement along the direction of the external potential. (a) $T_a = 0.01$, $\Phi_0 = 0.1$ and $\tau_p \in [0.02, 20]$. The strong external potential leads to a localization of the tagged particle on the time scale of the simulation. (b) $T_a = 1.0$, $\Phi_0 = 1.0$ and $\tau_p \in [0.02, 20]$. Weaker external potential slows down the tagged particle motion but does not localize it on the time scale of the simulation. Dashed lines show the tagged particle mean squared displacement in the direction perpendicular to the external potential for $\tau_p = 20$. The motion in the perpendicular direction is unperturbed by the external potential.

The tagged particle density distributions shown in Fig. 3.1 can be fitted very well to the Boltzmann distribution $\propto \exp(-\Phi(\mathbf{r})/T^{\text{fit}})$ using T^{fit} as the fit parameter[145]. The resulting values T^{fit} are shown in Fig. 3.3. We observe that the fitted temperatures decrease with increasing persistence time, which could have been anticipated from the persistence time dependence of the tagged particle densities.

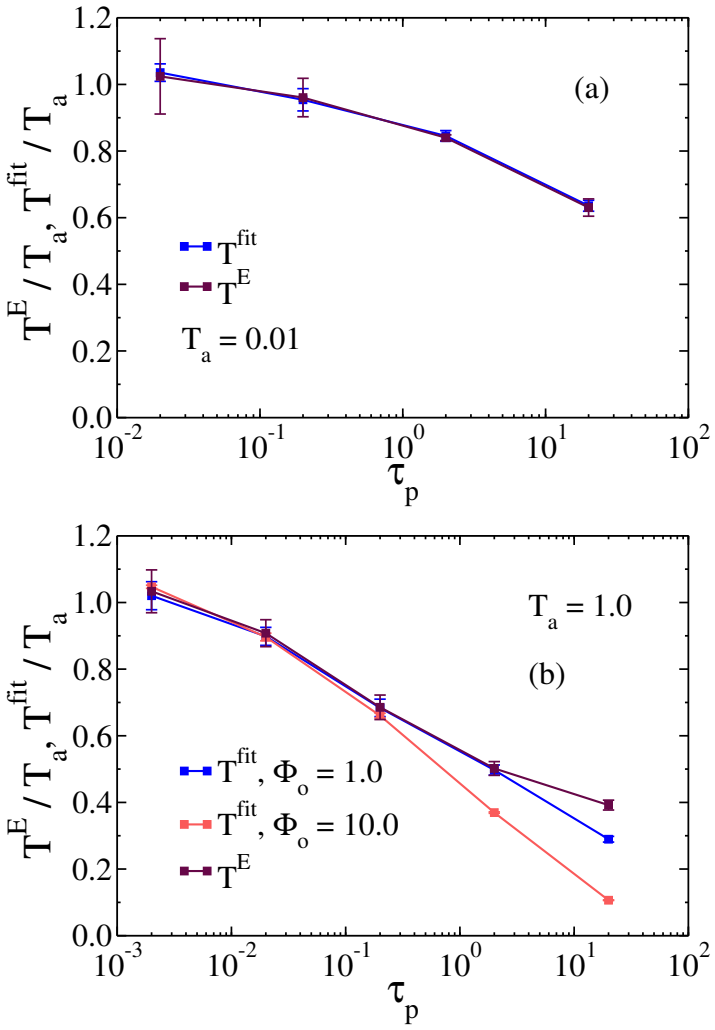

Figure 3.3: Comparison of the temperatures obtained from fitting Boltzmann distributions to the tagged particle density distributions and the Einstein relation effective temperatures. (a) $T_a = 0.01$, $\Phi_0 = 0.1$ and $\tau_p \in [0.02, 20]$. (b) $T_a = 1.0$, $\Phi_0 = 1.0$, and $\Phi_0 = 10.0$, and $\tau_p \in [0.002, 20]$. All temperatures are shown relative to the active temperature T_a.

To verify our theory presented in Sec. 4.3 we need to check whether temperatures obtained from the fits, T^{fit}, are the same as the Einstein temperatures obtained from the ratios of the self-diffusion and tagged particle mobility coefficients. Even before calculating the latter temperatures we can infer from Fig. 3.3 that the theory does not work for the two longest persistence times for $T_a = 1.0$. The reason is that the Einstein temperature describes an unperturbed system and thus does not depend on Φ_0 whereas for the two longest persistence times for $T_a = 1.0$ the temperatures obtained from the fits depend on Φ_0. We will return to this issue at the end of this section.

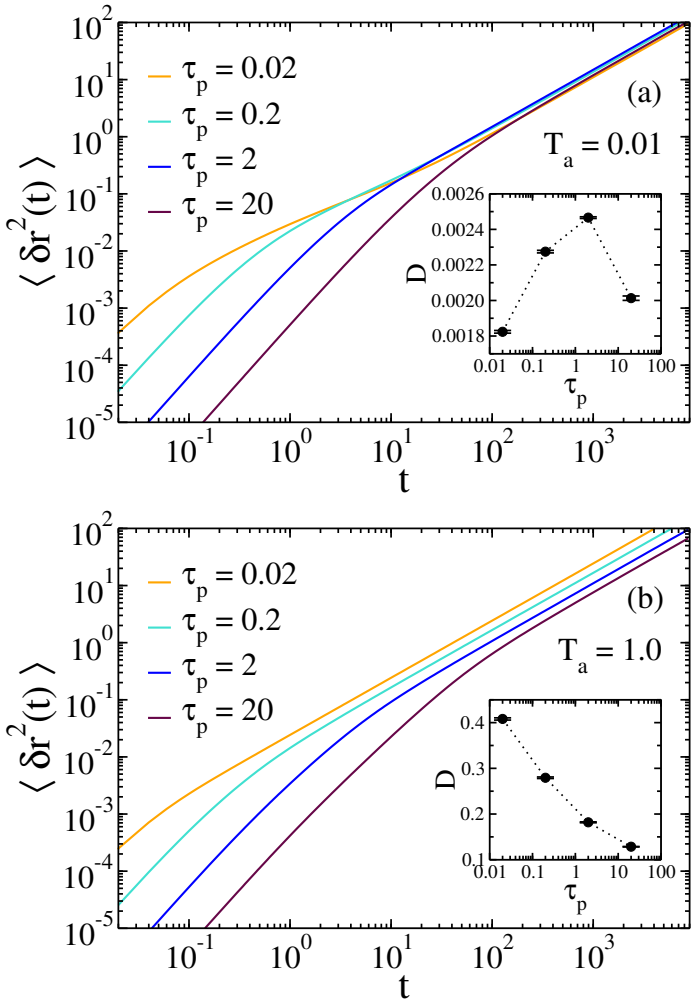

Figure 3.4: Mean squared displacement in unperturbed systems. (a) $T_a = 0.01$ and $\tau_p \in [0.02, 20]$. (b) $T_a = 1.0$ and $\tau_p \in [0.02, 20]$. Insets: persistence time dependence of the self-diffusion coefficient. D is a non-monotonic function of τ_p at $T_a = 0.01$ and decreases monotonically with increasing τ_p at $T_a = 1.0$.

In Figs. 4.5(a-b) we show the MSDs $\langle \delta r^2(t) \rangle$, where $\delta r^2(t) = (\mathbf{r}_1(t) - \mathbf{r}_1(0))^2$, for unperturbed systems. The self-diffusion coefficients are calculated from these MSDs according to Eq. (3.35) and are presented in the insets. As anticipated and in agreement with earlier investigations[137,144], we get two different behaviors of the self diffusion coefficient at the two active temperatures investigated. For the lower active temperature, $T_a = 0.01$, we observe a non-monotonic dependence of the self-diffusion coefficient on the persistence time, and for the higher active temperature, $T_a = 1.0$, we observe that the self-diffusion coefficient decreases monotonically with increasing persistence time.

In Figs. 3.5(a-b) we show the persistence time dependence of the time-dependent response function $\chi(t)$[134] at the two active temperatures investigated. The insets show the mobility coefficients calculated from the long time limit of $\chi(t)$ according to Eq. (3.36). We note that at the lower active temperature, $T_{\rm a} = 0.01$, the mobility monotonically increases with increasing τ_p, in contrast to the non-monotonic behavior of the self-diffusion coefficient. At the higher active temperature, $T_{\rm a} = 1.0$, the mobility monotonically decreases with increasing persistence time, and thus exhibits the same τ_p dependence as the self-diffusion coefficient.

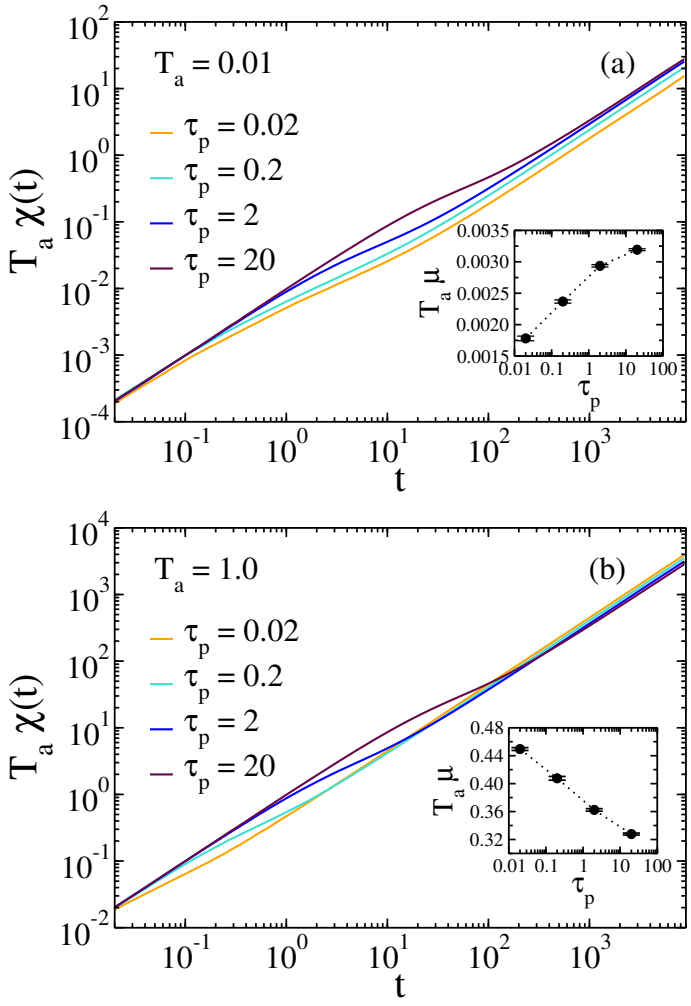

Figure 3.5: Time dependent response functions that characterize the response to a weak external potential in unperturbed systems calculated using Eq. 3.37. (a) $T_a = 0.01$ and $\tau_p \in [0.02, 20]$. (b) $T_a = 1.0$ and $\tau_p \in [0.02, 20]$. Insets: persistence time dependence of the tagged particle mobility coefficient. $T_a\mu$ increases monotonically with increasing τ_p at $T_a = 0.01$ and it decreases monotonically with increasing τ_p at $T_a = 1.0$.

Comparing insets in Figs. 4.5(a-b) and in Figs. 3.5(a-b) we can see that at the smallest persistence times $D \approx T_a\mu$. This behavior is expected since in the limit of the vanishing persistence time at constant active temperature, the present model active systems becomes equivalent to Brownian systems at temperature equal to the active temperature, $T = T_a$. For a Brownian system the fluctuation-dissipation theorem holds and $D = T\mu$.

In Fig. 3.3 we compare the Einstein temperatures T^{E} defined as the ratios D/μ to the temperatures obtained from fits to the Boltzmann distribution, T^{fit}. As mentioned in the previous paragraph, in the limit of small persistence times our active system becomes equivalent to the Brownian system and both T^{fit} and T^{E} become equal to the active temperature. With increasing persistence time, while keeping the active temperature constant, both T^{fit} and T^{E} decrease. We note that the decrease of the ratio of the Einstein temperature and the active temperature, T^{E}/T_a, was observed before in active matter systems[134,137]. We recall that the ratio of the Einstein effective temperature to the bath temperature increases with increasing shear rate for colloidal suspensions under steady shear[139]. Qualitatively similar behavior is observed in quenched glassy systems undergoing aging[148,149]. However, the opposite behavior, *i.e.* an effective temperature smaller than the bath temperature, was observed in glassy systems upon a sudden increase of the bath temperature[150].

For the lower active temperature, $T_a = 0.01$, we observe a very good agreement between T^{fit} and T^{E} for all persistence times investigated. In contrast, for the higher active temperature, $T_a = 1.0$, we initially see a very good agreement between T^{fit} and T^{E} but then, for longer persistence times we observe that temperatures obtained from the fits deviate from the temperatures from the Einstein relation. Notably, it happens first for T^{fit} obtained for the more confining potential, $\Phi_0 = 10.0$, and then for T^{fit} obtained for the less confining potential, $\Phi_0 = 1.0$.

We recall that our theoretical derivation in Sec. 4.3 relied upon the assumption that the spatial variation of the potential and of the tagged particle density occurs on the longest relevant length scale. On the other hand, we know that with increasing persistence time systems of self-propelled particles may undergo a motility-induced phase separation and that upon approaching

such a transition they can exhibit long-range density fluctuations. To investigate the existence of such fluctuations we evaluated steady state structure factors of the unperturbed systems.

In Fig. 3.6 we show steady state structure factors $S(k)$,

$$S(k) = 1 + \frac{1}{N} \left\langle \sum_{i=1}^{N} \sum_{j \neq i}^{N} \exp\left[-i\mathbf{k} \cdot (\mathbf{r}_i - \mathbf{r}_j)\right] \right\rangle, \tag{3.39}$$

for unperturbed systems at both active temperatures. We observe that for the lower active temperature, $T_a = 0.01$, only a modest increase of $S(k)$ is observed for small wavevectors at the longest persistence times. This suggests that at this active temperature and in the range of the persistence times investigated density correlations are relatively short-ranged.

In contrast, for the higher active temperature, $T_a = 1.0$, we observe a large small-wavevector increase of $S(k)$ for the two longest persistence times. This suggests that at this active temperature at these persistence times there are long-ranged density fluctuations. To make this statement more quantitative we simulated a larger system consisting of 8×10^4 particles at $\tau_p = 2.0$. The small wavevector behavior of the steady state structure factor for this system is shown in the inset to Fig. 3.6. To quantify the range of the density correlations we fitted the numerical results to the Ornstein-Zernike form $f(k) = a/[1 + (bk)^2]$. We recall that the parameter b in the Ornstein-Zernike fit is a measure of the density correlation length. We obtained $b = 2.19$ which is perhaps moderate but is larger than the length on which the tagged particle density varies for $\Phi_0 = 10.0$ at $T_a = 1.0$, $\tau_p = 2.0$. Thus, in hindsight, it is not surprising that our theory is not applicable for these parameters.

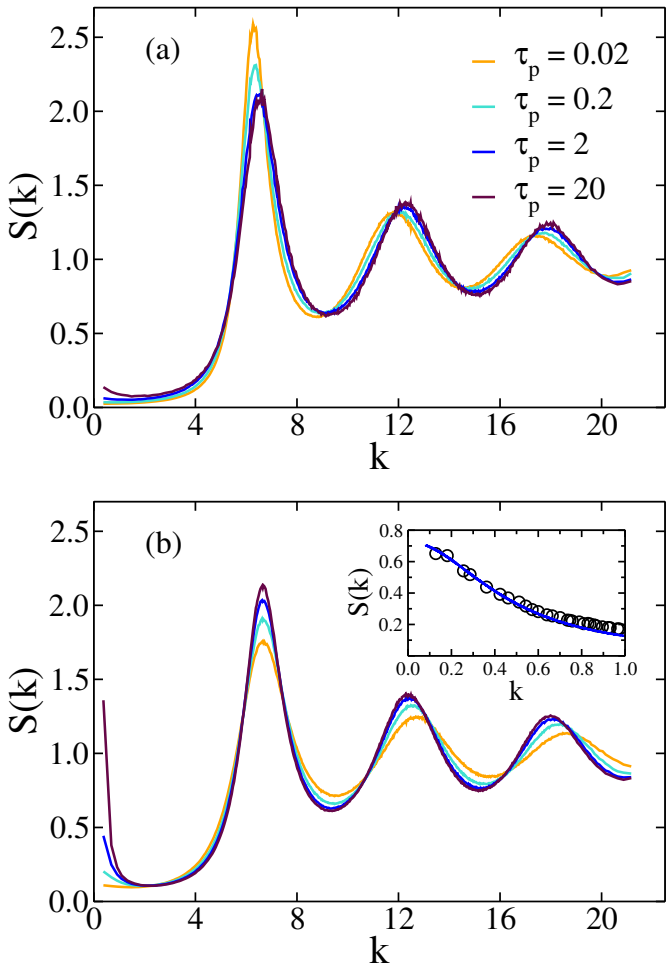

Figure 3.6: Stationary state structure factors of unperturbed systems. (a) $T_a = 0.01$ and $\tau_p \in [0.02, 20]$. (b) $T_a = 1.0$ and $\tau_p \in [0.02, 20]$. The upturn at small wavevectors indicates increasing correlation length. Inset in (b): small wavevector behavior of the structure factor calculated using 8×10^4 particle system for $T_\mathrm{a} = 1.0$ and $\tau_p = 2$. The solid line shows an Ornstein-Zernike function, $f(k) = a/[1 + (bk)^2]$, fitted to the data.

3.5 Conclusions

We derived an expression for the tagged particle density distribution in a slowly varying in space external potential in a system of interacting athermal active particles. The tagged particle distribution has the Boltzmann functional form, but the role of the temperature is played by the ratio of the self-diffusion and tagged particle mobility coefficients. We used computer simulations to verify the theoretical result. The theory works well if the characteristic length of the tagged particle density variation is the longest relevant length in the system. The theory is inapplicable

if the characteristic length of the density fluctuations is longer than the the characteristic length of the tagged particle density variation.

The ratio of the self-diffusion and tagged particle mobility coefficients has long been known as the Einstein temperature, one of several effective temperatures obtained for non-equilibrium systems from the fluctuation-dissipation ratios. We emphasize that in our calculations D and μ depend only on the properties of the system and, unlike parameters of the Einstein temperature, are insensitive to the strength of the external potential. Our result shows that the Einstein temperature determines the large spatial scale tagged particle density distribution beyond the linear response regime. This resembles earlier results that established that the Einstein temperature plays a similar role for a single Brownian particle in a tilted periodic potential[138] and for a tagged particle in a colloidal suspension under steady shear flow[139]. These three results obtained for very different systems suggest that the Einstein temperature may be generally relevant for the large spatial scale tagged particle density distribution in any stationary non-equilibrium system in which the large scale motion is diffusive. We note that the significance of the Einstein temperature was also investigated in driven granular media, see, *e.g.*, Refs. [151, 152] and references therein, but mostly in the linear response regime. It would be interesting to check whether the Einstein temperature determines the large scale tagged granular particle distribution beyond the linear response, along the lines of Refs. [138, 139] and the present work.

Finally, we note that our result, which is exact in the limit of slow varying tagged particle density, may serve as a test case for approximate theories for active matter in external potentials.

3.6 Data availability

The data that support the findings of this study are available from the corresponding author upon reasonable request.

3.7 Funding

We gratefully acknowledge the support of NSF Grant No. CHE 1800282.

Chapter 4

A systematic deviation from the exact theory of Brownian motion: density distribution, current, and self-diffusion of an active particle in a tilted periodic potential.[†]

4.1 Overview

The giant enhancement of diffusive motion of a Brownian particle in a tilted periodic potential is a phenomenon that was theoretically predicted by Reimann *et al.* [153]. Here, we consider the similar problem of studying the active motion in a tilted periodic potential where the motion of the particle is deterministically directed to the right. In our active system, we vary the persistence time τ_p as a control parameter that quantifies the distance from a Brownian system. We pursue two goals: (a) whether Reimann's results are recovered in a system of active Ornstein-Uhlenbeck particles and (b) whether the formulation of a theory within the unified colored noise approximation can predict the computer simulations. In accordance with the observed effects in a Brownian system, our numerical simulations show a monotonic enhancement of the particle current with an increase in the amplitude of the tilting force and a giant enhancement of diffusion coefficient at a threshold tilting force. We further derive approximate expressions for the stationary probability distribution and the current. A comparison with our numerical simulations shows that the theoretical expressions quantitatively predict the particle distribution and current in the range of $\tau_p \in [0, 1.0]$. Within the same range of persistence times, however, the theory for the stationary probability distribution breaks down at higher amplitudes of the tilting force.

[†]Alireza Shakerpoor[a], Grzegorz Szamel[a]; [a] Department of Chemistry, Colorado State University, Fort Collins, CO, USA.

4.2 Introduction

Transport phenomena in spatially periodic systems have been widely investigated due to their relevance to many phenomenological models as well as physical systems. They describe different phenomena in condensed phase systems including transport on crystalline surfaces[154,155], fluctuations of currents in Josephson junctions[156], superionic conductance[157], transport through confined spatially periodic geometries[158,159], as well as their role in the theories of chemical reaction rates and jump events[160].

One major application of transport in spatially periodic systems is their extension to the study of ratchet systems, *i.e.* periodic systems which lack the spatial inversion symmetry. Such systems have attracted much interest since they can induce stationary currents on the microscale where stochastic motion of particles is transformed into a directed transport. A stationary current through the stochastic dynamics of a system in thermal equilibrium is prohibited by the second law of thermodynamics. One can achieve a directed transport, however, when two conditions are met[161–163]. First, the system has to be driven out of the thermal equilibrium state by additional deterministic or stochastic perturbations. The existence of a periodic potential as an external perturbation suffices to force the system out of the equilibrium state. Second, the spatial inversion symmetry of the system has to be broken. Out of many available options, one common way to achieve a broken symmetry is by imposing a tilting force on the periodic potential which leads to the so-called ratchet potential. In this setup, the energy required for a directed transport is provided by thermal noise, external time-dependent modulation, or a non-equilibrium energy input[163]. The noise-induced transport in a periodic potential landscape that lacks inversion symmetry gives rise to a Brownian ratchet system.

While there is a rich literature focusing on the Brownian ratchets[161,164–169], the ratchet effects of a class of intrinsically non-equilibrium systems known as active particles have been the subject of a limited investigation[170,171]. The constituents of an active system are able to turn the ambient or stored energy into autonomous, self-propelled motion. This energy dissipation at an individual unit level drives the system out of the equilibrium state[48,65,119]. Thus, as intrinsically non-equilibrium

systems with spontaneous directed motion, it will be interesting to investigate active systems from the perspective of a ratchet system.

This work is motivated by theoretical[153,172], numerical[166,173], and more recent experimental results[174–176] which have reported a monotonic enhancement of the current with an increase in the amplitude of the tilting force and a giant enhancement of the diffusion coefficient at a threshold tilting force[161].

Here we examine an active Ornstein-Uhlenbeck particle (AOUP) under the influence of a periodic potential tilted by a static force. This class of particles have been used to model the collective motion of cells as well as the motion of passive tracers in an active bath[68]. For such a system of AOUP and within the unified colored noise approximation, we derive expressions for the probability density distribution and the particle current/velocity. We further examine the analytical results by running numerical simulations. For the density distribution and regardless of the amplitude of the persistence time, our analytical and numerical results predict a more diffused stationary distribution with an increase in the amplitude of the tilting force. Counterintuitively, we observe a smaller particle current with an increase in the persistence time of the AOUP at all tilting forces studied here. Finally, our numerical results show an enhanced diffusion coefficient whose amplification becomes stronger with an increase in the persistence time.

This chapter is organized as follows. In Sec. 4.3 we present our theoretical results for the stationary density distribution and particle current. In Sec. 4.4 we discuss our numerical simulations and compare the theoretical predictions with numerical results. Our overview and concluding remarks are presented in Sec. 4.5. Lastly, we detail the derivations of the stationary density distribution and the current in Sec. 4.6.1 and Sec. 4.6.2, respectively.

4.3 An Active Particle Under the Influence of a Non-Conservative Force

The following stochastic equations describe the motion of an overdamped, athermal active Ornstein-Uhlenbeck particle in an external potential, $V(x)$.

$$\dot{x} = -\frac{1}{\gamma}\,\partial_x V(x) + \eta,$$
$$\dot{\eta} = -\frac{\eta}{\tau_p} + \left(\frac{D_0^{1/2}}{\tau_p}\right)\Gamma(t). \tag{4.1}$$

Here, x is the position of the 1-d particle, γ is the friction coefficient, η is a Gaussian colored noise with the persistence time τ_p, D_0 is the free diffusion coefficient (i.e. $D_0 = k_{\rm B}T_a/\gamma$ with $k_{\rm B}$ being the Boltzmann coefficient and T_a being the active temperature which characterizes the strength of the self-propulsions), and Γ is a zero-mean, Gaussian white noise with correlation $\langle\Gamma(t)\Gamma(s)\rangle = 2\delta(t-s)$. The tilted periodic potential takes the form $V(x) = \Phi(x) - Fx$, where F is a non-conservative force that modifies the periodic potential $\Phi(x)$.

We recall that the problem of a Brownian particle moving in a tilted periodic potential has been shown to have exact solutions for the distribution function, current, and diffusion coefficient[153,177]. In the present work, we will use the unified colored-noise approximation (UCNA) to derive exact expressions for the stationary state density distribution and current of active systems with finite persistence time. The UCNA is an extension of the adiabatic elimination procedure (AEP) where the latter provides a systematic and rigorous approach to construct Fokker-Planck equations for the slow space variables of the system via the elimination of fast variables[178]. The UCNA was originally proposed to describe the nonlinear dynamical systems with a moderate to strong intensity of the stochastic force η. It extends the AEP to systems with finite relaxation times of fast varying variables (*i.e.* $\tau_p \neq 0$)[91].

The application of the UCNA to our problem leads to the following equation for the stationary state probability distribution (see Sec. 4.6.1),

$$P_{\rm s}(x) = Ae^{-\beta\int_0^x dx' N^{-1}(\partial_{x'}V(x'))}\left|N^{-1}\right|\Big(\int_0^x dx' e^{\beta\int_0^{x'} dx'' N^{-1}(\partial_{x''}V(x''))}\left|N^{-1}\right| + \frac{\int_0^L dx e^{\beta\int_0^x dx' N^{-1}(\partial_{x'}V(x'))}\left|N^{-1}\right|}{e^{\beta\int_0^L dx N^{-1}(\partial_x V(x))}-1}\Big). \tag{4.2}$$

In this equation, A is the normalization constant, $\beta = (k_{\mathrm{B}}T_a)^{-1}$, $N(x)$ involves the second derivative of the potential with the form $N(x) = [1 + \tau_p\gamma^{-1}(\partial_x^2 V(x))]^{-1}$, L indicates the size of the system, and $|\cdots|$ denotes an absolute value. We note that the form of the function in Eq. 4.2 results from a non-vanishing current that originates from the non-conservative force tilting the periodic potential. In this form and in the limit of $\tau_p \to 0$, the stationary state density function approaches the distribution of a Brownian particle moving in the same external potential.

Furthermore, we use the stationary state density distribution to derive the following expression for the particle current within the UCNA (see Sec. 4.6.2),

$$v = \frac{D_0 L\left(1 - \exp(-\beta F L)\right)}{\int_0^L dx \int_0^L dy \left(N(x)N\left(x+y\right)\right)^{-1} \exp\left[-G(x) + G\left(x+y\right)\right]}. \tag{4.3}$$

where $G(x) = \beta \int_0^x dx' N^{-1}(x') \left(\partial_{x'} V(x')\right)$. As for the stationary state probability distribution, we test the validity of Eq. 4.3 by running numerical simulations at varied state points of temperature, persistence time, and the strength of the tilting force.

4.4 Numerical Simulations

4.4.1 Methods

We simulate an AOUP system of athermal particles whose motions evolve according to Eq. 4.1. For such a system, the thermal Brownian fluctuations are negligible compared to the random Gaussian force η. While our goal is to study a single AOUP, to improve the statistics it is advantageous to run many simulations of one particle in parallel. To this end, we prepare a system of $N = 100$ non-interacting particles with a uniform random initial distribution. The particles have a unit mass and they are bound to a 1-d box of length L. The external potential used in simulations, $V(x) = -\sin(2\pi x/L) - Fx$, is periodic over the box length and is tilted by the static force F. To highlight the departure from a Brownian system, we additionally simulate independent sets of passive Brownian particles (PBPs) where they can be modeled by,

$$\dot{x} = -\frac{1}{\gamma}\,\partial_x V(x) + D_0^{1/2}\Gamma(t). \tag{4.4}$$

In our simulations, we adopt a system of units such that the Boltzmann constant k_{B} and the friction coefficient γ are unity. The time step in all simulations is $dt = 0.01$.

Two quantities of interest in our simulations, the mean velocity and self-diffusion coefficient, are defined as follows

$$v = \lim_{t\to\infty} \frac{\langle x(t)\rangle}{t}, \tag{4.5}$$

$$D = \lim_{t\to\infty} \frac{\langle x(t) - \langle x(t)\rangle\rangle^2}{2t}, \tag{4.6}$$

where $\langle\cdots\rangle$ denote an ensemble average. For an active system, we show that when the periodic potential is effectively tilted, these quantities are enhanced compared to a particle in an unbiased periodic potential.

4.4.2 Results and discussion

For a particle trapped in a potential energy well, a sufficiently strong tilting of the washboard potential can reduce the potential energy barrier and set the particle at a running state until it is trapped into the next local minimum. This reduced potential barrier allows the particle to run freely downhill the potential landscape[175]. As shown in Fig. 4.1, the Brownian and active systems have a more diffused density distribution with an increase in the amplitude of the tilting force due to the particles being more likely to overcome the potential barrier. Besides, a comparison of distributions calculated at different F shows that with increasing the amplitude of the tilting force, the density distributions of active and Brownian systems become more similar.

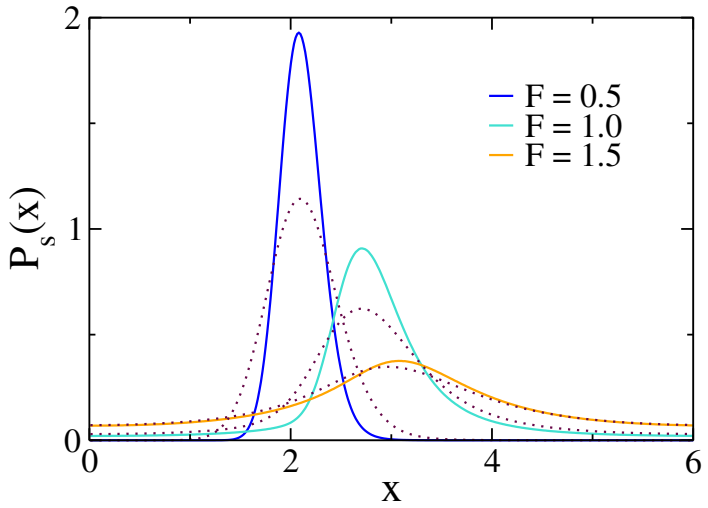

Figure 4.1: Stationary state distribution of active particles calculated with different static external force F. As a reference, the dotted lines show the distribution of a PBP moving under the influence of the same static force. The results here are shown for systems at $T_a = 0.1$ and active particles with $\tau_p = 2.0$.

Fig. 4.2 shows the excellent agreement of the major result of this chapter (expressed in Eq. 4.2) with the numerical simulations. When $F = 0$, the approximate probability density quantitatively predicts the density distribution of the active particles across systems with different active temperatures and persistence times. We note that a similar agreement has been reported for the density functions derived within the UCNA for single and interacting active particles in a repulsive force field[120]. Similarly, the same agreement is observed for the smaller values of the tilting force as illustrated in Fig. 4.3 for $F = 0.5$. The theory, however, breaks down for active systems with stronger tilting force of $F = 1.5$ where the deviation from the simulation is only observed at the longer persistence time of $\tau_p = 1.0$. By comparing Fig. 4.2 and Fig. 4.3 we also note that the tilting force makes the Gaussian-like spatial distribution of the particles more asymmetric. This asymmetry in distribution is however overestimated by the theoretical prediction whose deviation from the simulation becomes more pronounced for systems with a stronger tilting force and longer persistence time.

Finally, we emphasize that the calculations presented in this section are limited to $\tau_p \leq 1.0$ while for longer persistence times the theory gives unphysical results.

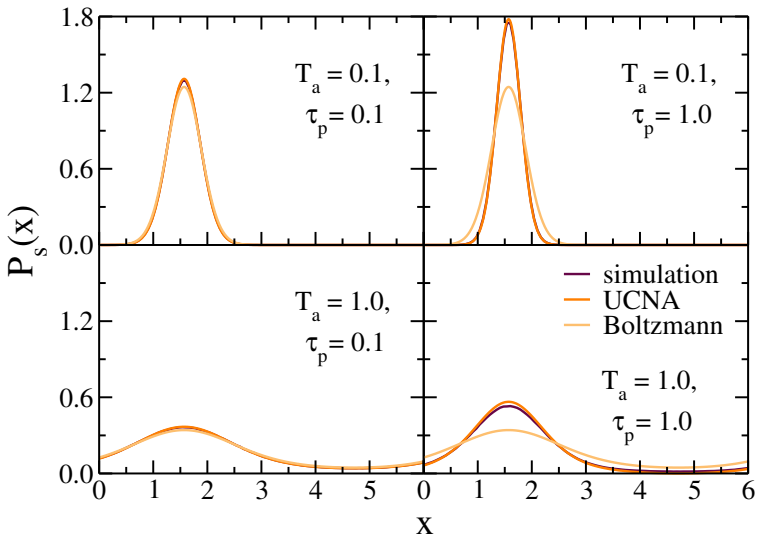

Figure 4.2: Stationary state distributions of active particles in a confining periodic potential shown in the absence of a static external force. As a reference, the Boltzmann distributions illustrate systems in equilibrium ($\tau_p = 0$).

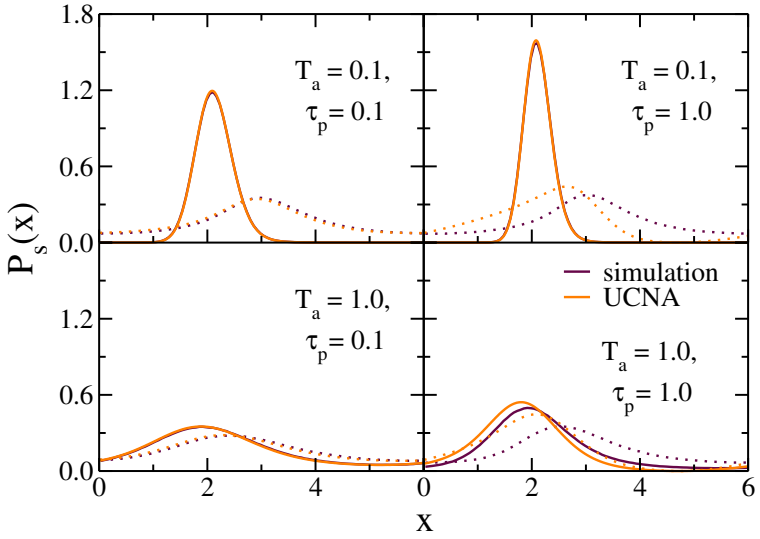

Figure 4.3: Stationary state distributions of active particles in a periodic potential tilted by a static external force F. The solid and dotted lines (with a similar color coding to the solid lines) belong to systems with $F = 0.5$ and $F = 1.5$, respectively.

To further investigate the dependence of dynamical variables of the active system on a tilted periodic potential, we numerically calculated the mean velocities and self-diffusion coefficients in a range of the tilting force F. Fig. 4.4 illustrates the dependence of mean velocities calculated

at $T_a = 0.1$ and 0.01 on τ_p and F. While at both active temperatures the tilting force leads to a monotonic increase of mean velocities, it is difficult to distinguish between the velocities of active and Brownian particles at the lower active temperature. At the higher active temperature of $T_a = 0.1$, however, the accelerating effect of the tilting force is stronger for Brownian and active particles with smaller τ_p. This is a rather unexpected result since the particles with a longer persistence time are expected to maintain a more consistent motion on the potential landscape regardless of the depth of the potential well implying a higher likelihood of making a jump over a potential barrier. Nonetheless, we observe a higher velocity for particles with a smaller persistence time. We also note that the split in velocities is mostly evident around $F = 1.0$ and it disappears at the extremes of the higher and lower F. It is noteworthy that for the range of tilting forces studied, the velocities at both active temperatures maintain approximately the same magnitude for most F.

The insets compare our numerical results with the theoretical predictions for the velocity. The results, which are obtained at $\tau_p = 1.0$, show that Eq. 4.3 can quantitatively predict the velocity within the interval of small to moderate persistence times. Nonetheless, as for the stationary probability density obtained within the UCNA, the theory for the velocity breaks down beyond $\tau_p = 1.0$. This marks the limitation of the UCNA applied to our system of active particles with longer noise correlation times.

On a broader note, we summarize the application of the UCNA to the present problem as being limited to $\tau_p \leq 1.0$. Within this range of persistence time, the theory gives quantitative results for the stationary density distribution when $F = 0$. For small F, the theory predicts the numerical calculations quantitatively while for large F, it fails to provide a qualitative agreement with simulations. Likewise, the theory for the mean velocity remains in quantitative agreement with the numerical simulations within $\tau_p \in [0, 1.0]$ yet, not shown here, a comparison between the mean velocities calculated at different persistence times shows that the theory fails to correctly predict the trend observed in Fig. 4.4 where the particles with a longer persistence time demonstrate a stronger enhancement of the mean velocity.

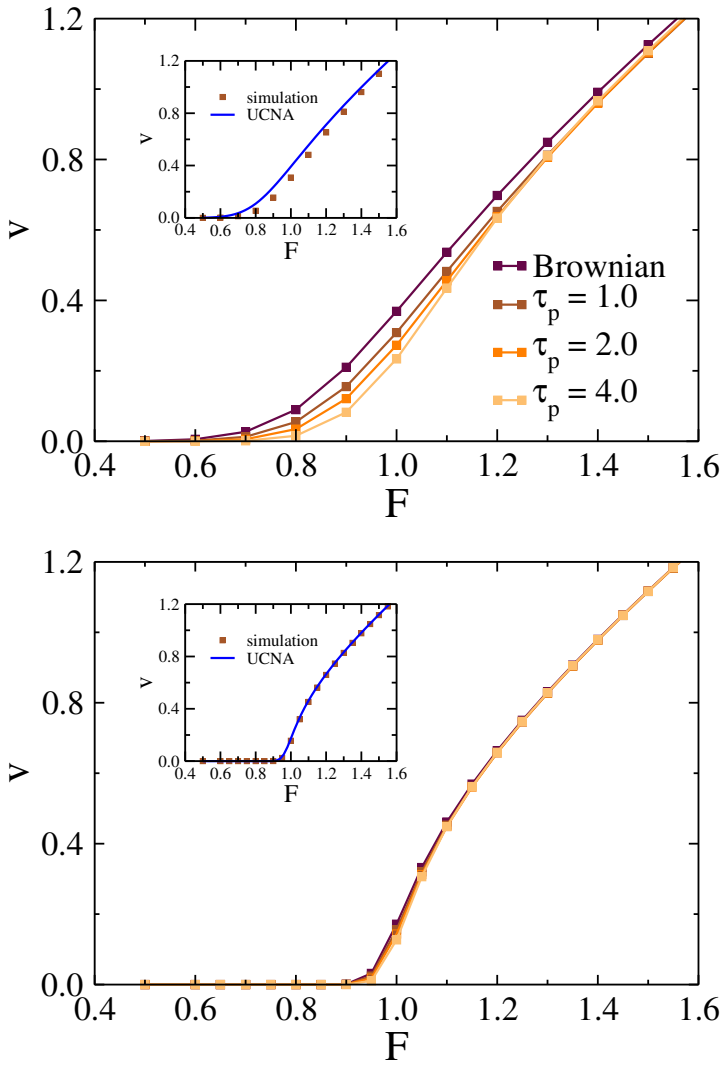

Figure 4.4: Enhanced mean velocities of Brownian and active particles under the influence of a static external force. Shown in the top panel, the velocities calculated at $T_a = 0.1$, are more strongly enhanced for a PBP while for an active particle the enhancement becomes weaker with an increase in τ_p. The bottom panel, however, shows that the split in velocities at the lower active temperature of $T_a = 0.01$ disappears while the enhancement in velocities retains the same magnitude as that of $T_a = 0.1$ for most F. The lines are guides to the eye. Insets: comparison between the theoretical prediction and numerical results calculated for $\tau_p = 1.0$ at the corresponding active temperature.

In Fig. 4.5 we show the dependence of self-diffusion coefficients calculated at two active temperatures on τ_p and F where the self-diffusion coefficient is normalized to the free diffusion coefficient D_0 (proportional to the temperature). Unlike the monotonic dependence of the mean velocities on the tilting force, we observe a giant enhancement of the diffusion coefficient at a threshold tilting force. The restricted interval of the enhanced diffusion coefficients, which is

approximately centered around a critical tilting force F_c, becomes considerably narrower at the lower active temperature. At the higher active temperature, the enhancement in this interval of F becomes stronger for active particles with higher τ_p while their distribution of D over F becomes narrower. Conversely, outside this interval, the enhancement at both temperatures is more effective for the PBP and active particles with smaller τ_p. We also find that the force F_c is relatively insensitive to the temperature while the enhancement of the diffusion coefficient is strongly dependent on the temperature.

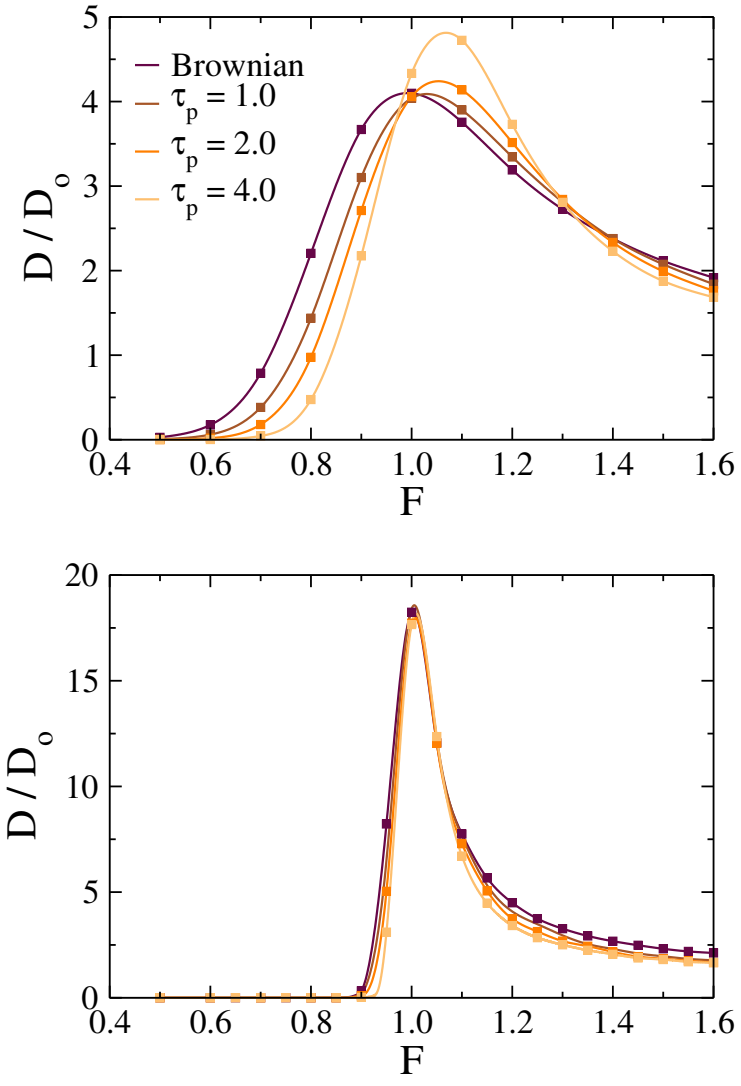

Figure 4.5: Giant amplification of the self-diffusion coefficient observed in a finite range of the static force evaluated at $T_a = 0.1$ (top panel) and $T_a = 0.01$ (bottom panel). The lines are guides for the eye.

4.5 Conclusions

As intrinsically non-equilibrium systems with autonomous directed motion, active systems are likely to make the design of a ratchet system richer by adding to the degrees of freedom of such systems. In this work we have explored the motion of an overdamped AOUP in a so-called ratchet potential. In the absence of a tilting force, our theoretical density distribution function successfully predicts the numerical results for systems with $\tau_p \leq 1.0$. When the tilting force is turned on, it has an added effect of distorting the particle's spatial distribution whose impact is overestimated by our theoretical expression at higher amplitudes of the tilting force.

Our calculations for the particle current show that active particles with a longer persistence time have a smaller particle current at all tilting forces investigated. This suggests that active particles with shorter persistence times are more likely to make jumps spanning local minima. However, this gap between the currents of particles with different persistence times disappears at lower active temperatures. Furthermore, we observe a similar to Brownian particles' giant enhancement of self-diffusion coefficient, where a stronger enhancement is only observed at the higher temperature for active particles with a longer persistence time. The giant enhancement of self-diffusion lends itself to applications such as particle sorting resolution[175] yet it degrades the coherent motion of the particles.

In conclusion, our theoretical results derived for an overdamped AOUP within the UCNA prove quantitatively accurate for small to moderate colored noise correlation times ($\tau_p \leq 1.0$). Here, by comparing our results to that of a Brownian system, we observe that in the limit of an overdamped system and strong tilting force, the source of the driving fluctuations becomes rather irrelevant in determining the dynamics of the system.

4.6 Theoretical Derivation

4.6.1 Approximate density function of an AOUP in a tilted periodic potential

To derive an approximate density function for an AOUP in a tilted external potential, we follow the standard adiabatic elimination procedure to obtain the Langevin equation by eliminating the fast varying Gaussian noise η from the equations of motion described in Eq. 4.1[91,120,178]. The elimination of η yields the following equation,

$$\begin{aligned}\ddot{x} &= -\frac{1}{\gamma}\left(\partial_x^2 V(x)\right)\dot{x} - \frac{1}{\tau_p}\left[\dot{x} + \frac{1}{\gamma}\left(\partial_x \Phi(x) - F\right)\right] + \frac{D_0^{1/2}}{\tau_p}\Gamma(t), \\ &= -\left(\frac{1}{\tau_p} + \frac{1}{\gamma}\left(\partial_x^2 V(x)\right)\right)\dot{x} - \frac{1}{\tau_p \gamma}\left(\partial_x \Phi(x) - F\right) + \frac{D_0^{1/2}}{\tau_p}\Gamma(t). \end{aligned} \tag{4.7}$$

Next, to obtain the Langevin dynamics we adopt the conventional adiabatic approximation in an overdamped system by setting $\ddot{x} = 0$,

$$\dot{x} = -\frac{1}{\gamma} N(x)\left(\left(\partial_x \Phi\right) - F\right) + D_0^{1/2} N(x)\Gamma(t), \tag{4.8}$$

where we have introduced $N(x) = \left[1 + \tau_p \gamma^{-1}\left(\partial_x^2 V(x)\right)\right]^{-1}$ which has a non-singular limit as $\tau_p \to 0$. Then, the Langevin equation can be transformed to the Fokker-Planck dynamics for the density function to give[179],

$$\partial_t P(x,t) = -\partial_x \left[-\frac{1}{\gamma} N(x)\left(\left(\partial_x \Phi\right) - F\right)\right] P(x,t) + D_0 \partial_x N(x) \partial_x N(x) P(x,t). \tag{4.9}$$

The external potential, which is tilted by the non-conservative force F, yields a finite current. Thus, the stationary form of the equation with the probability current A_0 reads,

$$\frac{1}{\gamma} N(x)\left(\left(\partial_x \Phi\right) - F\right) P_{\mathrm{s}} + D_0 N(x) \partial_x N(x) P_{\mathrm{s}} = A_0. \tag{4.10}$$

We multiply this equation by $N^{-1}(x)$ from the left-hand side and then further expand it to obtain,

$$\left[\frac{1}{D_0\gamma}\left((\partial_x\Phi)-F\right)+\left(\partial_x N(x)\right)\right]P_{\rm s}+N(x)\left(\partial_x P_{\rm s}\right)=\frac{A_0}{D_0}N^{-1}(x). \tag{4.11}$$

Another left-hand side multiplication by $N^{-1}(x)$ yields the following exactly solvable differential equation,

$$\partial_x P_{\rm s}+\left[\frac{1}{D_0\gamma}N^{-1}(x)\left((\partial_x\Phi)-F\right)+\partial_x\ln N(x)\right]P_{\rm s}=\frac{A_0}{D_0}N^{-2}(x). \tag{4.12}$$

The solution to this equation then reads,

$$P_{\rm s}(x)=e^{-\beta\int_0^x dx' N^{-1}(\partial_{x'}V(x'))}\left|N^{-1}\right|\left[\frac{A_0}{D_0}\int_0^x dx' e^{\beta\int_0^{x'}dx'' N^{-1}(\partial_{x''}V(x''))}\left|N^{-1}\right|+C\right]. \tag{4.13}$$

Finally, we determine the constant C by applying the periodic boundary condition $P_{\rm s}(0)=P_{\rm s}(L)$, which gives the general solution described in Eq. 4.2 with the normalization constant $A=A_0/D_0$.

4.6.2 Particle current within UCNA

Let us assume that the particle described in Eq. 4.9 evolves according to the operator Ω. We assume that the particle starts at $x=x_0$ and then evolves. Thus, its distribution follows,

$$P\left(x\mid x_0;t\right)=\exp\left(\Omega t\right)\delta\left(x-x_0\right). \tag{4.14}$$

We are interested in the displacement of the particle from its position at x_0, *i.e.* in the distribution

$$P_{\text{displ}}\left(y\mid x_0;t\right)=P\left(y+x_0\mid x_0;t\right)=\int_{-\infty}^{\infty}dx\delta\left(y-x+x_0\right)P\left(x\mid x_0;t\right). \tag{4.15}$$

It is convenient to assume that the initial position is distributed according to the stationary distribution, $P_{\rm s}$. In other words, we want to average expression 4.15 over the stationary state distribution of x_0,

$$P_{\text{displ}}(y;t) = \int_0^L dx_0 P(y + x_0 \mid x_0; t) P_{\text{s}}(x_0), \tag{4.16}$$

$$= \int_{-\infty}^{\infty} dx \int_0^L dx_0 \delta(y - x + x_0) \exp(\Omega t) \delta(x - x_0) P_{\text{s}}(x_0). \tag{4.17}$$

We expect that in the long-time limit, on large spatial scale $P_{\text{displ}}(y;t)$ will satisfy a drift -diffusion equation. *I.e.* we expect,

$$\partial_t P_{\text{displ}}(y;t) \simeq -\partial_y (v - D\partial_y) P_{\text{displ}}(y;t). \tag{4.18}$$

The standard problem is what are the velocity v and diffusion coefficient D. In this section we focus on finding an expression for the former by considering the equation of motion for the Fourier transform of $P_{\text{displ}}(y;t)$ in the limit of large times and small wavevectors k. Among the various approaches to this problem, we choose the projection operator method to derive the exact but formal expression for v. We show that this solution can be reduced to the corresponding quadrature.

Let us introduce Fourier transform,

$$\begin{aligned} F(k;t) &= \int_{-\infty}^{\infty} dy e^{-iky} P_{\text{displ}}(y;t), \\ &= \int_{-\infty}^{\infty} dy e^{-iky} \int_{-\infty}^{\infty} dx \int_0^L dx_0 \delta(y - x + x_0) \exp(\Omega t) \delta(x - x_0) P_{\text{s}}(x_0), \\ &= \int_{-\infty}^{\infty} dx \int_0^L dx_0 e^{-ik(x-x_0)} \exp(\Omega t) \delta(x - x_0) P_{\text{s}}(x_0) = \int_0^L dx e^{-ikx} \exp(\Omega t) e^{ikx} P_{\text{s}}(x), \\ &= \left\langle e^{-ikx} \exp(\Omega t) e^{ikx} \right\rangle, \end{aligned} \tag{4.19}$$

where in the last line $\langle \ldots \rangle$ denote averaging with respect to the stationary state probability distribution over the period of the external potential, *i.e.* over $[0, L]$. Here, the operator Ω acts on everything to its right, including the stationary state distribution.

We note that in the limit of small wavevectors and large times, *i.e.* within the limit that approximation 4.18 holds, we expect to get

$$\partial_t F(k;t) \simeq -ik(v - iDk) F(k;t). \tag{4.20}$$

Now, Laplace transform of $F(k;t)$ is

$$F(k;z) = \left\langle e^{-ikx} \left(z - \Omega\right)^{-1} e^{ikx} \right\rangle, \tag{4.21}$$

and Laplace transform of the time derivative $\dot{F}(k;t)$ gives

$$zF(k;z) - F(k;t=0) = \left\langle e^{-ikx} \Omega \left(z - \Omega\right)^{-1} e^{ikx} \right\rangle. \tag{4.22}$$

For the Laplace transform and in the limit of small wavevectors and small z we expect to get

$$zF(k;z) - F(k;t=0) \simeq -ik\left(v - iDk\right) F(k;z). \tag{4.23}$$

We introduce the projection operator and orthogonal projection that obey,

$$\begin{aligned} \mathcal{P}\mathrm{B} &= e^{ikx} \rangle \left\langle e^{-ikx} \mathrm{B} \right., \\ \mathcal{Q} &= \mathcal{I} - \mathcal{P}, \end{aligned} \tag{4.24}$$

where B is an arbitrary state, $\mathcal{Q}$ denotes the orthogonal complement of the projection operator $\mathcal{P}$, and $\mathcal{I}$ is the identity. Now, we take the following standard steps

$$\begin{aligned} \left\langle e^{-ikx} \Omega (z - \Omega)^{-1} e^{ikx} \right\rangle &= \left\langle e^{-ikx} \Omega (\mathcal{P} + \mathcal{Q}) (z - \Omega)^{-1} e^{ikx} \right\rangle, \\ &= \left\langle e^{-ikx} \Omega e^{ikx} \right\rangle \left\langle e^{-ikx} (z - \Omega)^{-1} e^{ikx} \right\rangle \\ &+ \left\langle e^{-ikx} \Omega \mathcal{Q} (z - \mathcal{Q}\Omega\mathcal{Q})^{-1} \mathcal{Q}\Omega e^{ikx} \right\rangle \left\langle e^{-ikx} (z - \Omega)^{-1} e^{ikx} \right\rangle. \end{aligned} \tag{4.25}$$

Let us consider small wavevector limit of $\left\langle e^{-ikx} \Omega e^{ikx} \right\rangle$.

$$\begin{aligned} \left\langle e^{-ikx} \Omega e^{ikx} \right\rangle &= - \left\langle e^{-ikx} D_0 \partial_x \left[N(x) \left(-\beta V'(x) + \beta F + N'(x)\right) - \partial_x N^2(x) \right] e^{ikx} \right\rangle, \\ &= - iD_0 k \left\langle e^{-ikx} \left[N(x) \left(-\beta V'(x) + \beta F + N'(x)\right) - \partial_x N^2(x) \right] e^{ikx} \right\rangle, \\ &= - iD_0 k \left\langle N(x) \left(-\beta V'(x) + \beta F + N'(x)\right) \right\rangle - D_0 k^2 \left\langle N^2(x) \right\rangle, \end{aligned} \tag{4.26}$$

where we used the fact that the stationary state probability distribution is periodic over the period of the external potential. By comparing Eq. 4.26 with the anticipated Eq. 4.23, we identify the velocity as

$$v = D_0 \left\langle N(x) \left(-\beta V'(x) + \beta F + N'(x)\right)\right\rangle . \tag{4.27}$$

Next, we reduce this formal expression to the corresponding quadrature. Integration by parts and the periodicity of the stationary state probability distribution and $N(x)$ yield

$$v = D_0 \left\langle N(x) \left(-\beta \Phi'(x) + \beta F\right)\right\rangle - \frac{1}{2} D_0 \int_0^L dx N^2(x) \left(\partial_x P_{\rm s}\right). \tag{4.28}$$

We note that

$$\partial_x P_{\rm s} = -\beta N^{-1}(x) V^{'} P_{\rm s} + N(x) \left(\partial_x N^{-1}(x)\right) P_{\rm s} + A N^{-2}(x). \tag{4.29}$$

Substitution of the latter expression in Eq. 4.28 yields

$$\begin{aligned} v &= D_0 \left(\int_0^L dx N^2(x) \left(\partial_x P_{\rm s}\right) - \int_0^L dx N^3(x) \left(\partial_x N^{-1}(x)\right) P_{\rm s} - A \int_0^L dx \right) \\ &- \frac{1}{2} D_0 \int_0^L dx N^2(x) \left(\partial_x P_{\rm s}\right), \\ &= \frac{1}{2} D_0 \int_0^L dx N^2(x) \left(\partial_x P_{\rm s}\right) - D_0 \int_0^L dx N^3(x) \left(\partial_x N^{-1}(x)\right) P_{\rm s} - A D_0 L, \\ &= -A D_0 L, \end{aligned} \tag{4.30}$$

where in the third line, the first two terms on the right hand side cancel out due to integration by parts. Next, by using the normalization condition $\int_0^L dx P_{\rm s} = 1$ we determine A and obtain

$$v = -\frac{D_0 L}{\int_0^L dx e^{-\beta \int_0^x dx' N^{-1}(\partial_{x'} V(x'))} |N^{-1}| \left(\int_0^x dx' e^{\beta \int_0^{x'} dx'' N^{-1}(\partial_{x''} V(x''))} |N^{-1}| + \frac{\int_0^L dx e^{\beta \int_0^x dx' N^{-1}\left(\partial_{x'} V(x')\right)} |N^{-1}|}{e^{\beta \int_0^L dx N^{-1}(\partial_x V(x))} - 1} \right)}, \tag{4.31}$$

$$= \frac{D_0 L\left(1-\exp(-\beta F L)\right)}{\int_0^L dx e^{-\beta\int_0^x dx' N^{-1}(\partial_{x'}V(x'))}|N^{-1}|\Big(\left(\exp(-\beta FL)-1\right)\int_0^x dx' e^{\beta\int_0^{x'} dx'' N^{-1}(\partial_{x''}V(x''))}|N^{-1}| + \int_0^L dx e^{\beta\int_0^x dx' N^{-1}(\partial_{x'}V(x'))}|N^{-1}|\Big)}, \tag{4.32}$$

where the last line follows from the fact that $\beta\int_0^L dx N^{-1}\left(\partial_x V(x)\right) = -\beta FL$. To further simplify Eq. 4.32, we introduce the shorthand notation

$$G(x) = \beta\int_0^x dx' N^{-1}(x')\left(\partial_{x'}V(x')\right), \tag{4.33}$$

and we note that $\exp(-\beta FL)e^{G(x)} = e^{G(x+L)}$. Thus, the denominator of Eq. 4.32 is simplified to read

$$\begin{aligned}
&\int_0^L dx N^{-1}(x)e^{-G(x)}\int_x^L dx' N^{-1}\left(x'\right)e^{G(x')} \\
&+\exp(-\beta FL)\int_0^L dx N^{-1}(x)e^{-G(x)}\int_0^x dx' N^{-1}\left(x'\right)e^{G(x')}, \\
&=\int_0^L dx N^{-1}(x)e^{-G(x)}\int_x^L dx' N^{-1}\left(x'\right)e^{G(x')} + \int_0^L dx N^{-1}(x)e^{-G(x)}\int_0^x dx' N^{-1}\left(x'\right)e^{G(x'+L)}.
\end{aligned} \tag{4.34}$$

Then, due to $N(x)$ being periodic, *i.e.* $N(x) = N(x+L)$, one obtains

$$\begin{aligned}
&\int_0^L dx N^{-1}(x)e^{-G(x)}\int_x^L dx' N^{-1}\left(x'\right)e^{G(x')} + \int_0^L dx N^{-1}(x)e^{-G(x)}\int_0^x dx' N^{-1}\left(x'\right)e^{G(x'+L)}, \\
&=\int_0^L dx N^{-1}(x)e^{-G(x)}\int_x^L dx' N^{-1}\left(x'\right)e^{G(x')} \\
&+\int_0^L dx N^{-1}(x)e^{-G(x)}\int_L^{x+L} dx' N^{-1}\left(x'-L\right)e^{G(x')}, \\
&=\int_0^L dx N^{-1}(x)e^{-G(x)}\int_x^L dx' N^{-1}\left(x'\right)e^{G(x')} + \int_0^L dx N^{-1}(x)e^{-G(x)}\int_L^{x+L} dx' N^{-1}\left(x'\right)e^{G(x')}, \\
&=\int_0^L dx N^{-1}(x)e^{-G(x)}\int_x^{L+x} dx' N^{-1}\left(x'\right)e^{G(x')}, \\
&=\int_0^L dx N^{-1}(x)e^{-G(x)}\int_0^L dx' N^{-1}\left(x'+x\right)e^{G(x'+x)}.
\end{aligned} \tag{4.35}$$

Lastly, this leads to our final expression for v

$$v = \frac{D_0 L \left(1 - \exp(-\beta F L)\right)}{\int_0^L dx \int_0^L dy \left(N(x) N\left(x+y\right)\right)^{-1} \exp\left[-G(x) + G\left(x+y\right)\right]}. \tag{4.36}$$

Chapter 5

Concluding remarks and future work

In the studies presented in Chapters 2-4, we addressed three problems in amorphous systems. Chapter 2 focused on the interplay between the stability of a glass and the fluctuations in its elastic matrix in the low-frequency regime[180], Chapter 3 was mainly concerned with the formulation of the probability density of a tagged active particle beyond the linear response regime[181], and Chapter 4 discussed the problem of active motion in the context of a ratchet potential with a focus on the density distribution, particle current, and self-diffusion coefficient of a non-interacting active particle.

In the second chapter we numerically investigated spatial fluctuations of elastic moduli of computer glasses via coarse-graining of the elastic field. Numerical simulations are an ideal tool for studying the low-frequency structural and vibrational properties of amorphous solids because on one hand approaching the near-zero temperatures in an experimental setup is quite challenging. On the other hand, performing any experiment at a finite temperature would have not been accurate enough due to the role of anharmonic effects which add to the uncertainty of results interpretation. Furthermore, the numerical simulations are essential at the level of system preparation where using effective numerical techniques such as swap Monte Carlo algorithm allows for the preparation of ultra-stable glasses in a reasonable amount of time.

In this work we calculated the local shear and bulk moduli of glasses prepared by quenching from a supercooled liquid reference state. We determined that the Gaussian spatial distributions of elastic moduli become more uniform with increasing the stability. Furthermore, we were interested to examine the finite-range spatial correlations in the elastic matrix of the solid. We calculated the correlations for our most homogeneous/stable glass and found that the correlations decayed to zero at the size of the local box, indicating that only trivial correlations existed. To investigate the existence of any short-range correlations, we iterated a similar calculation for non-overlapping neighboring domains where again we did not detect any finite length scale associated with elastic

correlations. Notably, we found our calculations at odds with a recent experimental work whose results were interpreted within the context of the FET[104]. Contrary to our results, they found a significant correlation in the elastic matrix of their most stable amorphous solid. Our result was also at variance with a study by Gelin *et al.* which showed a long-range, power-law correlation in elastic matrix responsible for a logarithmic enhancement in Rayleigh scattering of amorphous solids[100]. Our calculations, however, were in agreement with other studies including the calculations by Mizuno and Ikeda where they detected long-range correlation in stress field but not any long-range correlation in elastic modulus field[105]. Here, we note that a recent study on disorder-induced wave attenuation in amorphous solids emphasizes that coarse-grained local elastic moduli fields fail to characterize long-range correlations in the elastic matrix[182]. Instead, to feature the elastic correlations, the study replaces spatial averages of the disorder parameter defined in Rayleigh scaling with ensemble averages. This argument, however, is contrary to previous studies which have used coarse-grained stress fields to demonstrate power-law correlation in deeply supercooled liquids[183].

Lastly, in this work we were interested to determine whether there was a finite size effect associated with our numerical calculations. To this end, we compared our results of systems with 3k, 48k, 96k, and 192k particles and determined that there was no discernible finite size effects. Besides, we observed that our smallest local domain box with approximately 36 particles still follows Gaussian elastic moduli statistics.

In short, it would be difficult to overestimate the entanglement of the structural, vibrational, and thermal features of amorphous materials to their elastic properties. Many studies on vibrational peculiarities of amorphous structures such as the excess of the low-frequency modes (*i.e.* the boson peak) and anomalous Rayleigh scaling in amorphous materials have pointed to the local and global elastic properties of amorphous solids[98,102,184,185]. However, it is the microscopic foundations of elasticity and its formulation that remain the subject of a lively debate[17,182,186].

In the research presented in Chapter 3, we were interested to determine an analytical expression for the distribution function of a tracer particle in a system of interacting active Ornstein-Uhlenbeck

particles. We recall that because active motion is not thermal, the stationary probability density cannot be written as $P_{\rm s} \propto \exp[-H/k_BT]$, with H being the Hamiltonian of the system, and thus a distinct treatment of such a non-equilibrium problem is required. Here, we considered a system of interacting AOUPs where a slowly varying in space external potential exclusively acted on a selected (*i.e.* tagged) particle. Given the non-uniform density of the tagged particle in an external potential, we considered the use of Chapman-Enskog's perturbative expansion as an appropriate choice to describe the diffusive motion of the tagged particle. This led us to the successful derivation of an exact but formal expression for the tagged particle's stationary density distribution. Notably, our analytical results showed that the distribution function of tagged particle followed the same form as that of the equilibrium system with an effective temperature replacing the heat bath temperature in the expression of the distribution function.

We note that in equilibrium statistical physics, temperature appears as a proportionality parameter that correlates the inherent fluctuations of an observable to the mean response of the system (to an external perturbation). More precisely, for small and transient perturbing field and within the limits of a linear response, temperature is defined by the fluctuation-dissipation relations[126,127]. The notion of an effective temperature is, however, presented in the context of non-equilibrium systems with slow dynamics as a quantity that captures deviations from the equilibrium fluctuation-dissipation theorem[124,187]. The identification of an effective temperature obtained through the violation of the time-independent Einstein relation, $T^{\rm E}\mu = D$, allowed us to further test the validity of tagged particle's density distribution beyond the linear response regime. To this end, we simulated different sets of strongly perturbed and unperturbed systems of AOUPs. A comparison of the effective temperature, obtained from the spatial distribution of the tagged particles, and the Einstein temperature showed that the effective temperature matched the Einstein temperature in a wide range of systems from near-equilibrium to far-from-equilibrium states.

Furthermore, we showed that our theory holds as long as the longest length scale in the system is associated with the variation of the external potential. *I.e.*, when the motility-induced phase separation causes long-wavelength density fluctuations in the system, the theory breaks down as

our theoretical derivation relied on smooth variation of the external potential and tagged particle's density on the length scale of the inter-particle distance. Through the calculation of the steady state structure factors, we demonstrated the violation of the latter in case of an inconsistency between the Einstein temperature and the effective temperature.

To sum up, our analytical results can be regarded as a successful application of the concept of effective temperature in the context of non-equilibrium systems in general and active systems in particular. Accordingly, we would expect that our derivation could effectively be extended to other active systems including the active Brownian system. While it remains as a future work, it would also be interesting to additionally investigate the variation of the internal pressure of the system with the effective temperature to determine an equation-of-state for the current active system.

The study in Chapter 4 addressed the problem of active motion in a tilted washboard potential. We derived analytical expressions for the stationary density distribution and current of an overdamped AOUP within the unified colored noise approximation (UCNA) and determined that such expressions are quantitatively accurate for small to moderate correlation times of the colored noise. In particular, we found that within the range of $\tau_p \in [0, 1.0]$, our theoretical expression for the density distribution accurately predicted the numerical results while the expression overestimated the asymmetric effect of the tilting force on the density distribution at higher values of F. By considering the current of active particles within a range of tilting force F, we also reported the non-intuitive behavior of particles with longer persistence time that showed a smaller rate of potential barrier crossing. Besides, our numerical calculations at the higher temperature showed a stronger enhancement of self-diffusion coefficient for active particles with a longer persistence time. We found that the critical tilting force at which the giant enhancement of diffusion coefficient happened, remained relatively insensitive to temperature.

The discussion presented in Chapter 4, however, leaves space for some unanswered questions and interpretations: what would be the effect of the shape of the piecewise potential on the acceleration of the self-diffusion coefficient. A study by Heinsalu *et al.* which centered around the dependence of diffusive and coherent motion of overdamped Brownian particles on the shape of

the external potential, found that diffusion coefficient and coherence level to be extremely sensitive to the asymmetry and the shape of the periodic potential[188]. Their results supports the idea that large values of the asymmetry parameter favors the amplification of diffusion. Besides, more recent theoretical and numerical calculations have shown that tiny, time-independent deviations from a strictly spatially periodic potential can effectively amplify the diffusion peak even compared to previously reported amplifications of the diffusive motion[169,189]. Together, these findings emphasize the impact of the shape and symmetry of the external periodic potential on the accelerating effects of the tilted potential.

Another idea is to discuss the same problem for an underdamped particle where the conventional adiabatic approximation does not apply. We anticipate that a similar derivation will be more challenging as the transition in the underdamped regime is characterized by an excess diffusion of the particle or similarly, by an excess noise in the response of the system[166].

Bibliography

(1) Chaikin, P. M.; Lubensky, T. C., *Principles of Condensed Matter Physics*, 1st; Cambridge University Press: University Press, Cambridge, 1995.

(2) Sacha, K.; Zakrzewski, J. *Rep. Prog. Phys.* **2018**, *81*, 016401.

(3) Kittel, C., *Introduction to Solid State Physics*, 8th; Wiley: Hoboken, New Jersey, 2005.

(4) Debenedetti, P. G.; Stillinger, F. H. *Nature* **2001**, *410*, 259.

(5) Tammann, G., *Der Glaszustand (in German)*, 1st; L. Voss: Leipzig, 1933.

(6) Chumakov, A. I.; Monaco, G. *J. Non-Cryst. Solids* **2015**, *407*, 126.

(7) Schirmacher, W.; Scopigno, T.; Ruocco, G. *J. Non-Cryst. Solids* **2015**, *407*, 133.

(8) Flubacher, P.; Leadbetter, A. J.; Morrison, J. A.; Stoicheff, B. P. *J. Phys. Chem. Solids* **1959**, *12*, 53.

(9) Leadbetter, A. J. *J. Chem. Phys.* **1969**, *51*, 779.

(10) Zeller, R. C.; Pohl, R. O. *Phys. Rev. B* **1971**, *4*, 2029–2041.

(11) Ashcroft, N. W.; Mermin, N. D., *Solid State Physics*, College Edition; Harcourt College Publishers: Orlando, Florida, 1976.

(12) Huang, K., *Statistical Mechanics*, 2nd; Wiley: Hoboken, New Jersey, 1987.

(13) Malinovsky, V. K.; Novikov, N.; Sokolov, A. P. *Physics Letters A* **1991**, *153*, 63.

(14) Schober, H. R. *J. Phys.: Condens. Matter* **2004**, *16*, S2659–S2670.

(15) Taraskin, S. N.; Elliott, S. R. *Phys. Rev. B* **2000**, *61*, 12017–12030.

(16) Shimada, M.; Mizuno, H.; Ikeda, A. *Phys. Rev. E* **2018**, *97*, 022609.

(17) Caroli, C.; Lemaître, A. *Phys. Rev. Lett.* **2019**, *123*, 055501.

(18) Wang, L.; Ninarello, A.; Guan, P.; Berthier, L.; Szamel, G.; Flenner, E. *Nat. Commun.* **2019**, *10*, 26.

(19) Mizuno, H.; Ruocco, G.; Mossa, S. *Phys. Rev. B* **2020**, *101*, 174206.

(20) Mizuno, H.; Shimada, M.; Ikeda, A. *Phys. Rev. Research* **2020**, *2*, 013215.

(21) Schirmacher, W.; Tomaras, C.; Schmid, B.; Baldi, G.; Viliani, G.; Ruocco, G.; Scopigno, T. *Condens. Matter Phys.* **2010**, *13*, 23606.

(22) Mizuno, H.; Tong, H.; Ikeda, A.; Mossa, S. *J. Chem. Phys.* **2020**, *153*, 154501.

(23) Baldi, G.; Giordano, V. M.; Ruta, B.; Maschio, R. D.; Fontana, A.; Monaco, G. *Phys. Rev. Lett.* **2014**, *112*, 125502.

(24) Saitoh, K.; Mizuno, H. *Soft Matter* **2021**, *17*, 4204.

(25) Mizuno, H.; Ikeda, A. *arXiv:2101.01371v1* **2021**.

(26) Angelani, L.; Paoluzzi, M.; Parisi, G.; Ruocco, G. *PNAS* **2018**, *115*, 8700.

(27) Cui, B.; Zaccone, A. *Eur. Phys. J. E* **2020**, *43*, 72.

(28) Wang, L.; Szamel, G.; Flenner, E. *Soft Matter* **2020**, *16*, 7165.

(29) Mizuno, H.; Shiba, H.; Ikeda, A. *PNAS* **2017**, *114*, 9767–9774.

(30) Grigera, T. S.; Martín-Mayor, V.; Parisi, G.; Verrocchio, P. *Nature* **2003**, *422*, 289–292.

(31) Cachill, D. G.; Pohl, R. O. *Ann. Rev. Phys. Chem.* **1988**, *93*, 121.

(32) Anderson, P. W.; Halperin, B. I.; Varma, C. M. *Philos. Mag.* **1972**, *25*, 1.

(33) Phillips, W. *J. Low Temp. Phys.* **1972**, *7*, 351.

(34) Wang, L.; Berthier, L.; Flenner, E.; Guan, P.; Szamel, G. *Soft Matter* **2019**, 7018–7025.

(35) Schober, H. R. *J. Non-Cryst. Solids* **2011**, *357*, 501.

(36) Beltukov, Y. M.; Parshin, D. A.; Giordano, V. M.; Tanguy, A. *Phys. Rev. E* **2018**, *98*, 023005.

(37) Mézard, M.; Montanari, A., *Information, Physics, and Computation*, 1st; Oxford University Press: New York, 2009.

(38) Berthier, L.; Ediger, M. D. *Physics Today* **2016**, *69*, 40.

(39) Szamel, G.; Flenner, E.; Berthier, L. *Phys. Rev. E* **2015**, *91*, 062304.

(40) Marchetti, M. C.; Joanny, J. F.; Ramaswamy, S.; Liverpool, T. B.; Prost, J.; Rao, M.; Simha, R. A. *Rev. Mod. Phys.* **2013**, *85*, 1143.

(41) Fodor, E.; Marchetti, M. C. *Physica A* **2018**, *504*, 106.

(42) Ramaswamy, S. *Ann. Rev. Condens. Matter Phys.* **2010**, *1*, 323.

(43) Zöttl, A.; Stark, H. *J. Phys.: Condens. Matter* **2016**, *28*, 253001.

(44) Berthier, L.; Flenner, E.; Szamel, G. *J. Chem. Phys.* **2019**, *150*, 200901.

(45) Elgeti, J.; Winkler, R.; Gompper, G. *Rep. Prog. Phys.* **2015**, *78*, 056601.

(46) Cates, M. E. *Rep. Prog. Phys.* **2012**, *75*, 042601.

(47) Needleman, D.; Dogic, Z. *Nature Rev. Mat.* **2017**, *2*, 17048.

(48) Vicsek, T.; Zafeiris, A. *Phys. Rep.* **2012**, *517*, 71.

(49) de Groot, S. R.; Mazur, P., *Non-Equilibrium Thermodynamics*, 1st; Dover: New York, 1984.

(50) Wang, H.; Qian, T.; Xu, X. *Soft Matter* **2021**, *17*, 3634.

(51) Gaspard, P.; Kapral, R. *Research* **2020**, *2020*, 9739231.

(52) Doi, M. *J. Phys.: Condens. Matter* **2011**, *23*, 284118.

(53) Berthier, L. *Phys. Rev. Lett.* **2014**, *112*, 220602.

(54) Caballero, F.; Nardini, C.; Cates, M. E. *J. Stat. Mech.* **2018**, *2018*, 123208.

(55) Fily, Y.; Marchetti, M. C. *Phys. Rev. Lett.* **2012**, *108*, 235702.

(56) Structure; of a Phase-Separating Active Colloidal Fluid, D. *Phys. Rev. Lett.* **2013**, *110*, 055701.

(57) Borthne, O. L.; Fodor, E.; Cates, M. E. *New J. Phys.* **2020**, *22*, 123012.

(58) Howse, J. R.; Jones, R. A. L.; Ryan, A. J.; Gough, T.; Vafabakhsh, R.; Golestanian, R. *Phys. Rev. Lett.* **2007**, *99*, 048102.

(59) Bricard, A.; Caussin, J.-B.; Desreumaux, N.; Dauchot, O.; Bartolo, D. *Nature* **2013**, *503*, 95.

(60) Fournier-Bidoz, S.; Arsenault, A. C.; Manners, I.; Ozin, G. A. *Chem. Commun.* **2005**, *441*, 441.

(61) Paxton, W. F.; Kistler, K. C.; Olmeda, C. C.; Sen, A.; Angelo, S. K. S.; Cao, Y.; Mallouk, T. E.; Lammert, P. E.; Crespi, V. H. *J. Am. Chem. Soc.* **2004**, *126*, 13424.

(62) Martin, P. C.; Parodi, O.; Pershan, P. S. *Phys. Rev. A* **1972**, *6*, 2401.

(63) Uhlenbeck, G. E.; Ornstein, L. S. *Phys. Rev.* **1930**, *36*, 823.

(64) Hermanns, H.; Felderhof, B. U. *J. Chem. Phys.* **2007**, *126*, 044902.

(65) Romanczuk, P.; Bär, M.; Ebeling, W.; Lindner, B.; Schimansky-Geier, L. *Eur. Phys. J. Special Topics* **2012**, *202*, 1.

(66) Solon, A. P.; Cates, M. E.; Tailleur, J. *Eur. Phys. J. Special Topics* **2015**, *224*, 1231.

(67) Cates, M. E.; Tailleur, J. *Europhys. Lett.* **2013**, *101*, 20010.

(68) Martin, D.; O'Byrne, J.; Cates, M. E.; Fodor, E.; Nardini, C.; Tailleur, J.; van Wijland, F. *Phys. Rev. E* **2021**, *103*, 032607.

(69) Tailleur, J.; Cates, M. E. *Phys. Rev. Lett.* **2008**, *100*, 218103.

(70) Bechinger, C.; Leonardo, R. D.; Löwen, H.; Reichhardt, C.; Volpe, G.; Volpe, G. *Rev. Mod. Phys.* **2016**, *88*, 045006.

(71) Caprini, L.; Marconi, U. M. B.; Puglisi, A.; Vulpiani, A. *J. Stat. Mech.* **2019**, *2019*, 053203.

(72) Elliott, S. R. *Europhys. Lett.* **1992**, *19*, 201.

(73) Gurevich, V. L.; Parshin, D. A.; Schober, H. R. *Phys. Rev. B* **2003**, *67*, 094203.

(74) Schirmacher, W. *Europhys. Lett.* **2006**, *73*, 892–898.

(75) Schirmacher, W.; Scopigno, T.; Ruocco, G. *J. Non-Cryst. Solids* **2015**, *407*, 133.

(76) Marruzzo, A.; Schirmacher, W.; Fratalocchi, A.; Ruocco, G. *Sci. Rep.* **2013**, *3*, 1407.

(77) Alexander, S. *Physics Reports* **1998**, *296*, 65.

(78) Wagner, H.; Bedorf, D.; Küchemann, S.; Schwabe, M.; Zhang, B.; Arnold, W.; Samwer, K. *Nat. Mater.* **2011**, *10*, 439–442.

(79) Mizuno, H.; Mossa, S.; Barrat, J.-L. *Phys. Rev. E* **2013**, *87*, 042306.

(80) Schirmacher, W; Ruocco, G; Scopigno, T *Phys. Rev. Lett.* **2007**, *98*, 025501.

(81) Allen, M. P.; Tildesley, D. J., *Computer Simulation of Liquids*, 1st; Oxford University Press: New York, 1987.

(82) Haile, J. M.; Gray, C. G. *Chem. Phys. Lett.* **1980**, *76*, 583.

(83) Szamel, G. *Phys. Rev E* **2014**, *90*, 012111.

(84) Kurzthaler, C.; Leitmann, S.; Franosch, T. *Sci. Rep.* **2016**, *6*, 36702.

(85) Dauchot, O.; Démery, V. *Phys. Rev. Lett.* **2019**, *122*, 068002.

(86) Caprini, L.; Marconi, U. M. B. *Soft Matter* **2019**, *15*, 2627.

(87) Sevilla, F. J.; Arzola, A. V.; Cital, E. P. *Phys. Rev. E* **2019**, *99*, 012145.

(88) Ten Hagen, B.; Kümmel, F.; Wittkowski, R.; Takagi, D.; Löwen, H.; Bechinger, C. *Nat. Commun.* **2014**, *5*, 4829.

(89) Takatori, S. C.; Dier, R. D.; Vermant, J.; Brady, J. F. *Nat. Commun.* **2016**, *7*, 10694.

(90) Deblais, A.; Barois, T.; Guerin, T.; Delville, P. H.; Vaudaine, R.; Lintuvuori, J. S.; Boudet, J. F.; Baret, J. C.; Kellay, H. *Phys. Rev. Lett.* **2018**, *120*, 188002.

(91) Jung, P.; Hänggi, P. *Phys. Rev. A* **1987**, *35*, 4464.

(92) Stephens, R. B. *Phys. Rev. B* **1973**, *8*, 2896–2905.

(93) Zaitlin, M. P.; Anderson, A. C. *Phys. Rev. B* **1975**, *12*, 4475–4486.

(94) Pohl, R. O.; Liu, X.; Thompson, E. *Rev. Mod. Phys.* **2002**, *74*, 991–1013.

(95) Mizuno, H.; Mossa, S.; Barrat, J.-L. *Phys. Rev. B* **2016**, *94*, 144303.

(96) Yoshimoto, K.; Jain, T. S.; Workum, K. V.; Nealey, P. F.; de Pablo, J. J. *Phys. Rev. Lett.* **2004**, *93*, 175501.

(97) Tsamados, M.; Tanguy, A.; Goldenberg, C.; Barrat, J.-L. *Phys. Rev. E* **2009**, *80*, 026112.

(98) Léonforte, F.; Tanguy, A.; Wittmer, J. P.; Barrat, J.-L. *Phys. Rev. Lett.* **2006**, *97*, 055501.

(99) Mizuno, H.; Mossa, S.; Barrat, J.-L. *PNAS* **2014**, *111*, 11949–11954.

(100) Gelin, S.; Tanaka, H.; Lemaître, A. *Nat. Mater.* **2016**, *15*, 1177–1181.

(101) Fan, Y.; Iwashita, T.; Egami, T. *Phys. Rev. E* **2014**, *89*, 062313.

(102) Mizuno, H.; Mossa, S.; Barrat, J.-L. *Europhys. Lett.* **2013**, *104*, 56001.

(103) Mizuno, H.; Silbert, L. E.; Sperl, M. *Phys. Rev. Lett.* **2016**, *116*, 068302.

(104) Pogna, E. A. A.; Chumakov, A. I.; Ferrante, C.; Ramos, M. A.; Scopigno, T. *J. Phys. Chem. Lett.* **2019**, *10*, 427–432.

(105) Mizuno, H.; Ikeda, A. *Phys. Rev. E* **2018**, *98*, 062612.

(106) Moriel, A.; Kapteijns, G.; Rainone, C.; Zylberg, J.; Lerner, E.; Bouchbinder, E. *arXiv:1905.03378* **2019**.

(107) Lerner, E. *J. Non-Cryst. Solids* **2019**, *522*, 119570.

(108) Ninarello, A.; Berthier, L.; Coslovich, D. *Phys. Rev. X* **2017**, *7*, 021039.

(109) Grigera, T. S.; Parisi, G. *Phys. Rev. E* **2001**, *63*, 045102.

(110) Gutiérrez, R.; Karmakar, S.; Pollack, Y. G.; Procaccia, I. *Europhys. Lett.* **2015**, *111*, 56009.

(111) http://lammps.sandia.gov.

(112) Plimpton, S. *J. Comp. Phys.* **1995**, *119*, 1–19.

(113) Tanguy, A.; Wittmer, J. P.; Leonforte, F.; Barrat, J.-L. *Phys. Rev. B* **2002**, *66*, 174205.

(114) Lakes, R. S.; Lee, T.; Bersie, A.; Wang, Y. C. *Nature* **2001**, *410*, 565–567.

(115) Mizuno, H.; Ruocco, G.; Mossa, S. *arXiv:1905.10235v1* **2019**.

(116) Lerner, E. *J. Chem. Phys.* **2020**, *153*, 216101.

(117) Chandler, D., *Introduction to Modern Statistical Mechanics*, 1st; Oxford University Press: Oxford, New York, 1987.

(118) Clark, N.; Ackerson, B. *Phys. Rev. Lett.* **1980**, *44*, 1005.

(119) Ramaswamy, S. *J. Stat. Mech.* **2017**, *2017*, 054002.

(120) Maggi, C.; Marconi, U. M. B.; Gnan, N.; Leonardo, R. D. *Sci. Rep.* **2015**, *5*, 10742.

(121) Farage, T.; Krinninger, P.; Brader, J. *Phys. Rev. E* **2015**, *91*, 042310.

(122) Rein, M.; Speck, T. *Eur. Phys. J. E* **2016**, *39*, 84.

(123) De Pirey, T.; Lozano, G.; van Wijland, F. *Phys. Rev. Lett.* **2019**, *123*, 260602.

(124) Cugliandolo, L. F. *J. Phys. A: Math. Theor.* **2011**, *44*, 483001.

(125) Puglisi, A.; Sarracino, A.; Vulpiani, A. *Phys. Rep.* **2017**, *709-710*, 1.

(126) Kubo, R. *Rep. Prog. Phys.* **1966**, *29*, 255.

(127) Marconi, U. M. B.; Puglisi, A.; Rondoni, L.; Vulpiani, A. *Phys. Rep.* **2008**, *461*, 111.

(128) Cugliandolo, L. F.; Kurchan, J.; Peliti, L. *Phys. Rev. E* **1997**, *55*, 3898.

(129) Berthier, L.; Barrat, J.-L. *J. Chem. Phys.* **2002**, *116*, 6228.

(130) For a review see, *e.g.*, A. Crisanti; Ritort, F. *J. Phys. A: Math. Gen.* **2003**, *36*, R181.

(131) Barrat, J.-L.; Kob, W. *EPL* **1999**, *46*, 637.

(132) For a review see, *e.g.*, L. Leuzzi *J. Non-Cryst. Solids* **2009**, *355*, 686.

(133) Levis, D.; Berthier, L. *EPL* **2015**, *111*, 60006.

(134) Szamel, G. *EPL* **2017**, *117*, 50010.

(135) Petrelli, I.; Cugliandolo, L. F.; Gonnella, G.; Suma, A. *Phys. Rev. E* **2020**, *102*, 012609.

(136) See also D. Loi; Mossa, S.; Cugliandolo, L. F. *Phys. Rev. E* **2008**, *77*, 051111, where a different effective temperature was used in an active matter investigation.

(137) Flenner, E.; Szamel, G. *Phys. Rev. E* **2020**, *102*, 022607.

(138) Hayashi, K.; i. Sasa, S. *Phys. Rev. E* **2004**, *69*, 066119.

(139) Szamel, G.; Zhang, M. *EPL* **2011**, *96*, 50007.

(140) For a general introduction to Chapman-Enskog expansion, see, *e.g.*, P. Résibois and M. de Leener, *Classical Kinetic Theory of Fluids*, 1st; Wiley: New York, 1977.

(141) Titulaer, U. M. *Physica A* **1978**, *91*, 321.

(142) Hess, W.; Klein, R. *Adv. Phys.* **1983**, *32*, 173.

(143) Fodor, E.; Nardini, C.; Cates, M. E.; Tailleur, J.; Visco, P.; van Wijland, F. *Phys. Rev. Lett.* **2016**, *117*, 038103.

(144) Berthier, L.; Flenner, E.; Szamel, G. *New J. Phys.* **2017**, *19*, 125006.

(145) In practice, we fitted function $A\exp(-\Phi(\mathbf{r})/T^{\text{fit}})$ using both A and T^{fit} as independent fit parameters. We verified that the resulting fits were correctly normalized, *i.e.* that $\int_V d\mathbf{r}\ A \times \exp(-\Phi(\mathbf{r})/T^{\text{fit}}) = 1$ within error.

(146) Abou, B.; Gallet, F. *Phys. Rev. Lett.* **2004**, *93*, 160603.

(147) Pottier, N. *Physica A* **2005**, *345*, 472.

(148) Sciortino, F.; Tartaglia, P. *Phys. Rev. Lett.* **2001**, *86*, 107.

(149) Berthier, L. *Phys. Rev. Lett.* **2007**, *98*, 220601.

(150) Gnan, N.; Maggi, C.; Parisi, G.; Sciortino, F. *Phys. Rev. Lett.* **2013**, *110*, 035701.

(151) Puglisi, A.; Baldassarri, A.; Vulpiani, A. *J. Stat. Mech.* **2007**, *2007*, P08016.

(152) Gnoli, A.; Puglisi, A.; Sarracino, A.; Vulpiani, A. *PLoS ONE* **2014**, *9*, e93720.

(153) Reimann, P.; den Broeck, C. V.; Linke, H.; Hänggi, P.; Rubi, J. M.; Pérez-Madrid, A. *Phys. Rev. Lett.* **2001**, *87*, 010602.

(154) Lindenberg, K.; Lacasta, A. M.; Sancho, J. M.; Romero, A. H. *New J. Phys.* **2005**, *7*, 1.

(155) Sancho, J. M.; Lacasta, A. M.; Lindenberg, K.; Sokolov, I. M.; Romero, A. H. *Phys. Rev. Lett.* **2004**, *92*, 250601.

(156) Hänggi, P.; Talkner, P.; Borkovec, M. *Rev. Mod. Phys.* **1990**, *62*, 251.

(157) Fulde, P.; Pietronero, L.; Schneider, W. R.; Strässler, S. *Phys. Rev. Lett.* **1975**, *35*, 1776.

(158) Burada, P. S.; Hänggi, P.; Marchesoni, F.; Schmid, G.; Talkner, P. *ChemPhysChem* **2009**, *10*, 45.

(159) Burada, P. S.; Schmid, G.; Reguera, D.; Rubí, J. M.; Hänggi, P. *Phys. Rev. E* **2007**, *75*, 051111.

(160) Borromeo, M.; Marchesoni, F. *Phys. Rev. Lett.* **2000**, *84*, 203.

(161) Reimann, P. *Phys. Rep.* **2002**, *361*, 57.

(162) Hänggi, P.; Marchesoni, F.; Nori, F. *Ann. Phys.* **2005**, *14*, 51.

(163) Astumian, R. D.; Hänggi, P. *Physics Today* **2002**, *55*, 33.

(164) Seifert, U. *Rep. Prog. Phys.* **2012**, *75*, 126001.

(165) Burada, P. S.; Schmid, G.; Talkner, P.; Hänggi, P.; Reguera, D.; Rubí, J. M. *BioSystems* **2008**, *93*, 16.

(166) Costantini, G.; Marchesoni, F. *Europhys. Lett.* **1999**, *48*, 491.

(167) Faucheux, L. P.; Stolovitzky, G.; Libchaber, A. *Phys. Rev. E* **1995**, *51*, 5239.

(168) Gang, H.; Daffertshofer, A.; Haken, H. *Phys. Rev. Lett.* **1996**, *76*, 4874.

(169) Lindner, B.; Schimansky-Geier, L. *Phys. Rev. Lett.* **2002**, *89*, 230602.

(170) Schweitzer, F.; Tilch, B.; Ebeling, W. *Eur. Phys. J. B* **2000**, *14*, 157.

(171) Tilch, B.; Schweitzer, F.; Ebeling, W. *Physica A* **1999**, *273*, 294.

(172) Reimann, P.; den Broeck, C. V.; Linke, H.; Hänggi, P.; Rubi, J. M.; Pérez-Madrid, A. *Phys. Rev. E* **2002**, *65*, 031104.

(173) Dan, D.; Jayannavar, A. M. *Phys. Rev. E* **2002**, *66*, 041106.

(174) Evstigneev, M.; Zvyagolskaya, O.; Bleil, S.; Eichhorn, R.; Bechinger, C.; Reimann, P. *Phys. Rev. E* **2008**, *77*, 041107.

(175) Lee, S. H.; Grier, D. G. *Phys. Rev. Lett.* **2006**, *96*, 190601.

(176) Hayashi, R.; Sasaki, K.; Nakamura, S.; Kudo, S.; Inoue, Y.; Noji, H.; Hayashi, K. *Phys. Rev. Lett.* **2015**, *114*, 248101.

(177) By adopting the standard adiabatic elimination procedure, one can show that the stationary probability distribution of a Brownian particle follows the exact equation, $P_{\rm s}(x) = A\exp(-\beta V(x))\left[\frac{\int_0^L dx'\exp(\beta V(x'))}{1-\exp(-\beta FL)} - \int_0^x dx'\exp(\beta V(x'))\right]$.

(178) Evans, M. W.; Grigolini, P.; Parravicini, G. P., *Memory function approaches to stochastic problems in condensed matter*, 1st; Wiley: New York, 1985.

(179) van Kampen, N. G., *Stochastic processes in physics and chemistry*, 1st; Elsevier Science B.V.: Amsterdam, 1992.

(180) Shakerpoor, A.; Flenner, E.; Szamel, G. *Soft Matter* **2020**, *16*, 914.

(181) Shakerpoor, A.; Flenner, E.; Szamel, G. *J. Chem. Phys.* **2021**, *154*, 184901.

(182) Kapteijns, G.; Richard, D.; Bouchbinder, E.; Lerner, E. *J. Chem. Phys.* **2021**, *154*, 081100.

(183) Lemaître, A. *Phys. Rev. Lett.* **2014**, *113*, 245702.

(184) Tomoshige, N.; Goto, S.; Mizuno, H.; Mori, T.; Kim, K.; Matubayasi, N. *J. Phys.: Condens. Matter* **2021**, *33*, 274002.

(185) Tomoshige, N.; Mizuno, H.; Mori, T.; Kim, K.; Matubayasi, N. *Sci. Rep.* **2019**, *9*, 19514.

(186) Goldhirsch, I.; Goldenberg, C. *Eur. Phys. J. E* **2002**, *9*, 245–251.

(187) Hohenberg, P. C.; Shraiman, B. I. *Physica D* **1989**, *37*, 109.

(188) Heinsalu, E.; Tammelo, R.; Örd, T. *Phys. Rev. E* **2004**, *69*, 021111.

(189) Reimann, P.; Eichhorn, R. *Phys. Rev. Lett.* **2008**, *101*, 180601.